Master Thesis

Investigating the Relationship Between Clinical Image Characteristics and Mechanical Properties of In Vitro Thrombi in Acute Ischemic Stroke

A Comprehensive Analysis About Acute Ischemic Stroke

Chenrui Zhang

2023. November 27

Investigating the Relationship Between Clinical Image Characteristics and Mechanical Properties of In Vitro Thrombi in Acute Ischemic Stroke

A Comprehensive Analysis About Acute Ischemic Stroke

by

Chenrui Zhang

Student Name	Student Number
Chenrui Zhang	5441501

Defense time: 27.November.2023, at 10:00 A.M
Project Duration: March 2023 - November 2023
Thesis committee: Dr. Ir. F.J.H. Gijsen — TU Delft and Erasmus MC, Supervisor
Dr. B. Fereidoonnezhad — TU Delft, Supervisor
Dr. M. J. Mirzaali — TU Delft

TU Delft

Preface

Looking back at the past two years of my study abroad journey, I am filled with emotion. While this thesis may not represent my entire academic experience, it stands as a testament to my dedication and efforts. I hope that, as you read it, you can enjoy the journey just as I have.

The first class of my first year in TU Delft was Tissue Biomechanics, where I first met one of my mentors, Dr. ir. F.J.H. (Frank) Gijsen, and gained insights into the intricacies of human tissue and structure. In my second year, while searching for internship opportunities, I joined Dr. ir. F.J.H. (Frank) Gijsen and Dr. Behrooz Fereidoonnezhad's research group successfully. I cherish the experiences gained during my internship at Erasmus MC and working on my graduation project, along with the valuable friendships formed. The completion of this research project wouldn't have been possible without the careful guidance of Dr. Gijsen and Dr. Fereidoonnezhad. They have been incredibly helpful, offering patience and friendly assistance, whether it was academic or personal challenges. When facing immense pressure, they would genuinely advise me to take a break, creating invaluable experiences that made me feel warmth in a foreign land.

I also want to express gratitude to my parents Jianguo Zhang, Huiru Duan and family, who selflessly provide both financial and emotional support. They answer my calls even in the late hours, praying for me every day from over 8,000 kilometers away. With their help, I could wholeheartedly immerse myself in academic research, and they remain my strongest and most crucial pillars of support.

I extend my thanks to my boyfriend Zeqian Yuan, who has been my most important companion in the Netherlands. He provided all the assistance I needed during my initial transition, stood by me when I shed tears due to immense pressure, and did everything possible to make me feel happier and more relaxed, even with his own academic pressures. Although we have been separated between Belgium and the Netherlands in the last six months, a long-distance relationship indeed divides us geographically but not heartly.

Lastly, gratitude to my motherland.

Chenrui Zhang
Leuven, November 2023

Abstract

Stroke, currently ranked as the second leading cause of mortality and the most prevalent source of enduring disability, imposes significant societal and economic consequences. These consequences encompass the necessity for extended care, rehabilitation, and the economic burdens associated with lost productivity. In the diagnostic process, physicians typically employ imaging techniques to assess cerebral blood vessels, ruling out alternative conditions when stroke is suspected. Subsequent to diagnosis, treatments like Intravenous Thrombolysis (IVT) and Endovascular Thrombectomy (EVT) are administered to either dissolve or retrieve thrombi. However, with EVT emerging as the new standard of stroke care and an increasing body of evidence indicating the substantial impact of thrombus mechanical properties on thrombectomy success, the use of clot analogues is gaining prominence as a means of facilitating efficient mechanical testing, both in terms of time and finances. By establishing a link between mechanical properties and image characteristic parameters, medical practitioners gain a better understanding of intracranial thrombi before embarking on surgical procedures. This knowledge can serve as a theoretical foundation for optimizing surgical instruments and devising effective surgical protocols in the future.

In pursuit of these objectives, this study involved 29 patients and entailed several key steps: firstly, the extraction of imaging parameters from pre-EVT CT images; secondly, the creation of thrombus analogues from the patient's blood; thirdly, the execution of five distinct mechanical tests to derive mechanical properties, encompassing cyclic compression, compression relaxation, tensile test to failure, tensile relaxation, and fracture testing. Additionally, the hyperelastic Yeoh model was utilized to simulate the behavior observed from cyclic compression and tensile to failure test. Prony series (n=2) was fitted to stress relaxation curves.

In summary, this investigation revealed noteworthy observations pertaining to mechanical properties. Notably, hysteresis areas demonstrated robust and statistically significant correlations with compression high-strain stiffness, low-strain stiffness, and tensile stiffness along with the ultimate tensile stress, implying that the thrombus analogue exhibits both hyperelastic and viscoelastic characteristics. In the domain of imaging parameters, the evident interdependence among the densities of the three regions of interest within both CTA and NCCT is apparent, respectively. However, it is essential to underscore that the relationship between CTA and NCCT was not deemed statistically significant. Lastly, a noteworthy revelation was the strong negative monotonic correlation (ρ=-0.82, P=0.011) observed between the analogue contraction ratio of the thrombus analogue and the density of the middle part of NCCT in actual thrombi. This insight suggests that, in addition to thrombus composition, microstructure plays a pivotal role as well in determining their properties.

Contents

Nomenclature

Abbreviations

Abbreviation	Definition
AIS	Acute ischemic stroke
CT	Computed tomography
CTA	Computed tomography angiography
NCCT	Non-contrast computed tomography
HU	Hounsfield units
HAS	Hyperdense arterial sign
IVT	Intravenous thrombolysis
EVT	Endovascular thrombectomy
MT	Mechanical thrombectomy
ICA-T	Terminus of intracranial carotid artery
ROI	Region of interest
IQR	Interquatile range

1

Introduction

1.1. Acute ischemic stroke

As the second greatest cause of mortality and the most frequent cause of permanent disability today, stroke imposes significant societal and financial consequences in the form of long-term care, rehabilitation, and lost productivity [1]. It can be split into two types that are either predominantly ischemic or hemorrhagic [2]. Among these, acute ischemic stroke (AIS) accounts for 85% of all strokes worldwide [3]. Quantifiably, ischemic stroke affects 17 million people globally each year, with up to 6 million dying and a considerable proportion permanently disabled [4], [5].

In general, acute ischemic strokes essentially happen when blood flow to a portion of the brain is cut off. Most frequently, the clog is a blood clot or embolus, which could be a fragment of a clot or other material that has detached from another location in the circulatory system [6]. As shown in Figure 1, a blood clot can travel to a brain artery if it escapes from plaque development in a carotid artery in the neck. The clot may prevent blood flow to a portion of the brain, leading to the loss of brain tissue [7].

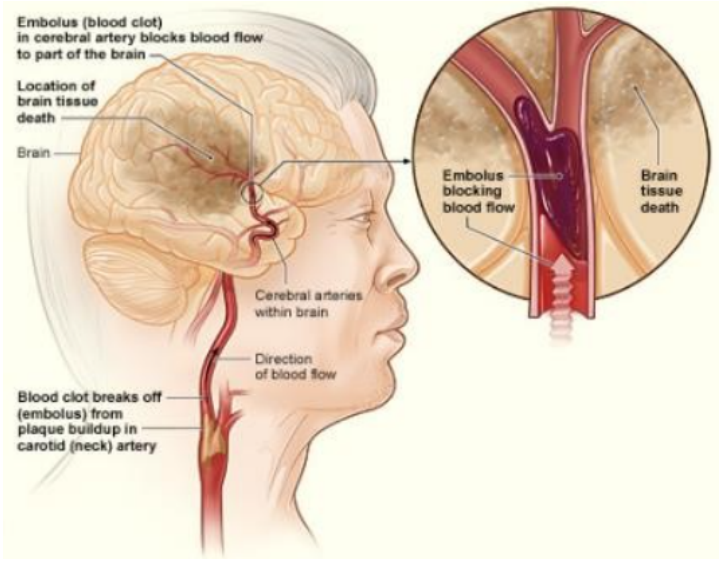

Figure 1: The illustration shows how an ischemic stroke can occur in the brain: a blood clot can travel to a brain artery if it escapes from plaque development in a carotid artery in the neck. The clot may prevent blood flow to a portion of the brain, leading to the loss of brain tissue [7].

1.2. Current diagnosis

Once a patient is suspected of having a stroke, doctors typically conduct an imaging test to examine the blood arteries in the brain in order to rule out alternative possibilities, such as a tumor, and to identify

the patient's specific kind of stroke and the location of the stroke [2], [7]. In the Netherlands, as well as in many other countries, the established procedure for diagnosing acute ischemic stroke entails obtaining computed tomography (CT) images [8]. This process involves the utilization of non-contrast computed tomography (NCCT) scans to distinguish between ischemic and hemorrhagic strokes, as shown in Figure 2A. Additionally, computed tomography angiography (CTA) scans are employed, which are contrast-enhanced scans used to visualize blood vessels and evaluate the existence and position of blood clots, as shown in Figure 2B [8].

CT imaging has the potential to distinguish high-fibrin thrombi from low-fibrin clots by calculating the differences in attenuation that the thrombus exhibits on imaging, in cases where the hematocrit levels (%H) are higher, the Hounsfield units (HU) average value of the thrombus tends to be higher [9]. Additionally, the classification can also be aided with the help of a hyperdense artery sign (HAS), which refers to the proximal middle cerebral artery appearing to have a higher attenuation, associated with a higher hematocrit level (%H). The presence of HAS is determined by RBC content, whereas their absence may signal fibrin-predominant occlusive thrombi [10].

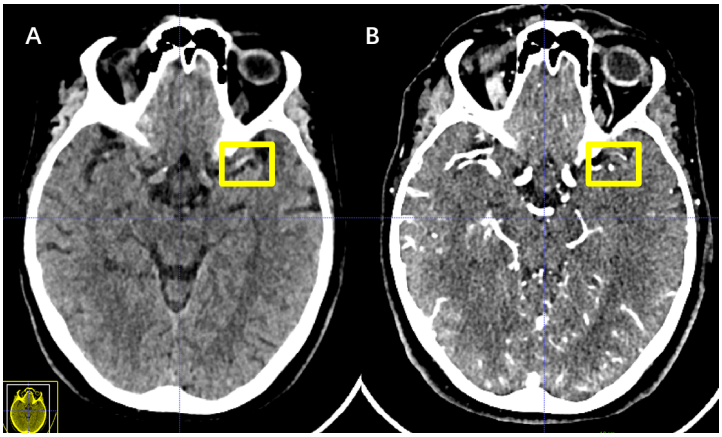

Figure 2: Imaging to diagnose stroke. CT scans of a patient with a left middle cerebral artery occlusion: A) During an NCCT scan, the presence of a thrombus is indicated by the HAS. B) During a CTA scan, the thrombus is located where the contrast stops.

1.3. Current treatments

There are various treatments available after an AIS diagnosis. Intravenous thrombolysis (IVT) and endovascular thrombectomy (EVT), also known as mechanical thrombectomy (MT), have shown efficacy in improving functional results [11]. However, the selection of treatment is influenced by a number of variables, including the time since the onset of symptoms and the site of the blockage [12].

A drug from the IVT group called tissue plasminogen activator (tPA) is one of the main therapy for an ischemic stroke [13]. After the patients get it through injection in their arms, it dissolves the blood clots that are obstructing blood flow to the brain [7]. Besides, doctors may give an anticoagulant or blood-thinning medicine to help stop blood clots from forming or getting larger when the patient is not suitable to have tPA. However, these medicines' main side effect is bleeding and the limited time window [11].

MT is a minimally invasive procedure used to remove occlusive thrombi in the vasculature of patients with acute ischemic stroke[14]. The first study that has proven MT to be effective for the treatment of acute ischemic stroke was in 2015 [15]. During thrombectomy, there are mainly three ways to retrieve the thrombus from the patients: by stent retrievers, by aspiration devices, and the combination of these two methods:

- **Thrombectomy stent retrieval**: Stent-retriever thrombectomy consists of multiple steps as shown in Figure 3. An extracranial internal carotid artery guidance catheter is first inserted. The intracranial thrombus is then passed by a micro-guidewire inserted through the guiding catheter. A microcatheter will follow the same route as the micro-guidewire and make sure the tip of the microcatheter is inserted beyond the thrombus. The micro-guidewire is subsequently taken out to provide room for the stent-retriever to be inserted via the microcatheter and afterward deployed

in the thrombus by retracting the microcatheter past the proximal end of the stent. By pushing it into the guiding catheter, the stent-retriever with the entrapped thrombus is then removed from the vascular [14]. However, as shown in Figure 4, the removed thrombus will often appear fragmented.

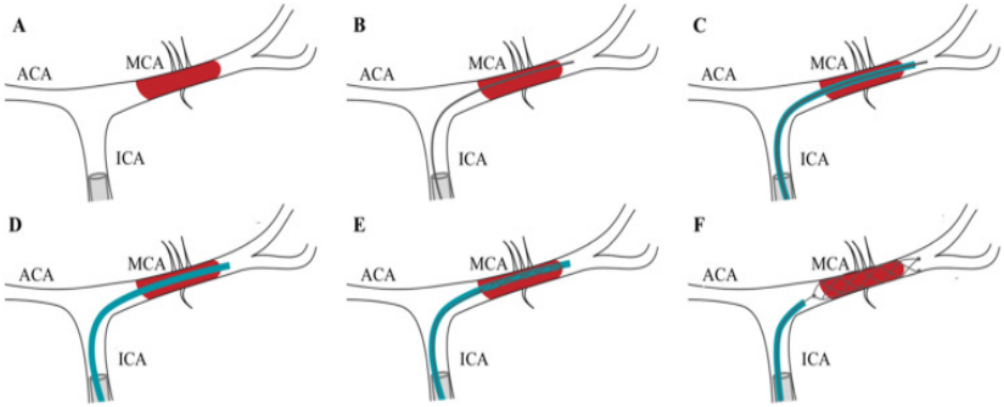

Figure 3: Stent-retriever thrombectomy steps [14].

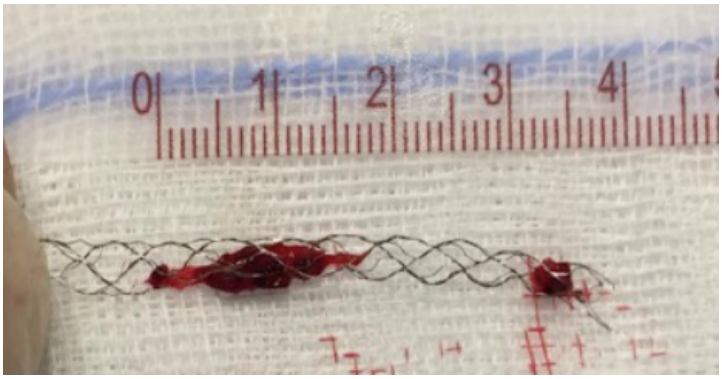

Figure 4: Stent-retriever with captured blood clot that has been removed from a cerebral artery [16].

- **Thrombectomy aspiration**: In thrombectomy aspiration, as shown in Figure 5, surgeons follow the same first 3 steps as Stent retriever thrombectomy. After that, aspiration is applied once the tip has been positioned at the proximal thrombus face. The result is that the thrombus is either completely aspirated into the catheter or is trapped by the catheter and then removed, thereby restoring blood flow [16].
- **Combination of aspiration and stent-retriever**: As shown in figure 6, this method combines a stent-retriever with primary aspiration, after the balloon at the tip of the balloon-guided catheter is inflated to create a flow block, the distal access catheter begins to aspirate. Then the stent retriever and distal access catheter are simultaneously applied to capture the thrombus. In the end, all catheters are withdrawn and blood flow to the brain is restored after the thrombus was captured [18].

In general terms, patients who present with stroke symptoms within a 4.5-hour window of onset may be eligible for IVT, making IVT the primary therapeutic modality [19]. Nevertheless, the existing anticoagulant and thrombolytic therapies for thrombus management are associated with notable drawbacks, including high costs, limited efficacy in a substantial portion of patients, inadequate prevention of recurrence, and post-thrombotic syndrome. Moreover, they carry the potential risk of inducing cerebral hemorrhage and precipitating severe hemorrhagic complications [20].

Meanwhile, certain investigations have demonstrated that EVT administered within a six to sixteen-hour time window following the onset of a stroke, in conjunction with standard medical treatment, re-

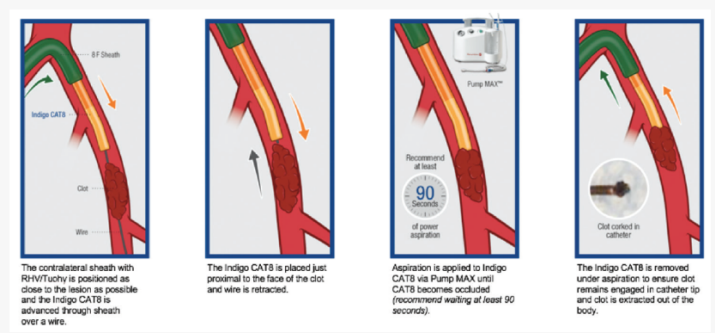

Figure 5: Thrombectomy aspiration steps [17].

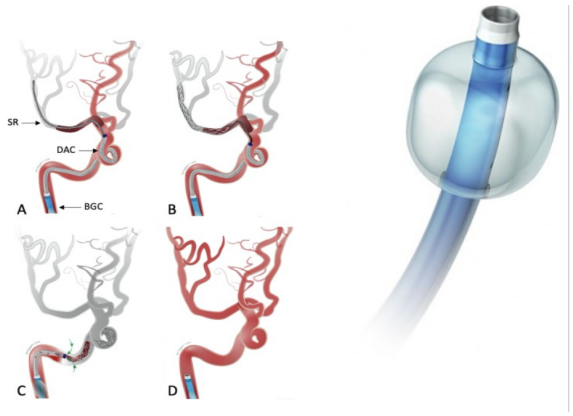

Figure 6: The operation steps of the “hybrid techniques”with a balloon guide catheter [16]

sulted in reduced disability and enhanced functional independence at the three-month mark compared to sole reliance on standard medical treatment. These findings imply that, in instances appropriately assessed by a medical professional, thrombectomy typically exhibits a superior success rate and expedites the recuperative process compared to not performing it [21].

1.4. Thrombus analogues

Evaluating thrombus material sourced from patients can frequently generate significant costs and involve stringent regulations, making the acquisition of specimens challenging [22]. Besides, a systematic investigation involving varied mechanical tests on thrombi from the same patients is not feasible. Consequently, in-vitro fabrication of clinically pertinent thrombus analogues becomes invaluable for pre-clinical assessments of MT outcome, as well as for evaluating the efficacy of these thrombectomy devices across various clot compositions [23].

These in vitro clot analogues should be assembled using blood proteins and components found in the natural clotting cascade, thus achieving a chemical composition similar to that of native clots. Besides, according to Cahalane $et\ al.$, the mechanics of thrombi are associated with their compositional characteristics [24]. Meanwhile, several research groups have proven that thrombus analogues exhibit similar properties as in vivo thrombi [22], [25]. Therefore, it is expected that thrombus analogues can be used as a substitute for in vivo thrombi in mechanical testing.

1.5. Mechanical characteristics

The mechanical characteristics of the occluding thrombus are proved to change significantly due to their composition [26]. This variation is the primary factor causing variable thrombus behavior during thrombectomy, which has a major impact on the procedure’s success [27]. Prior studies have conducted

diverse mechanical tests on thrombus analogues that were made from human blood, which includes compression tests [27]–[29], tensile tests [30], [31], rheometry [32]. In addition, a few studies have probed into the viscoelastic behavior of clot material [33]–[35]. To further investigate the effect of rate-dependent viscoelasticity of thrombus material, researchers also took loading–unloading hysteresis and stress-relaxation into account [22]. They discovered that the thrombus analogues were found to exhibit dynamic stress relaxation, indicating that the clot exhibits viscoelastic behavior by displaying non-linear hyperelastic strain stiffening and loading-unloading hysteresis [22]. However, there is a lack of information on the mechanical properties related to real patients' thrombi.

1.6. Constitutive and computational models

Representing mechanical tests conducted on thrombus analogues mathematically is a critical step in improving the basic scientific knowledge of thrombus and in developing computational models for diagnosis and prognosis [36]. The behavior of thrombi and their mechanical properties can be more accurately predicted by creating models with material properties retrieved from experimental tests of real thrombi. This allows researchers to study thrombectomy success and failure in advance using the in silico thrombectomy model.

The exploration of thrombus viscoelasticity begins with the linear spring model [32], [37], [38]. They tried to model each fiber in the network as a linear spring. Additionally some linear viscoelastic models were introduced, notably the Kelvin-Voigt model [39]–[41] and the Zener model [33]. While the linear model is more straightforward to utilize, it proves insufficient for capturing the viscoelastic behavior under substantial deformations (>5 %) [42]. Therefore, different models which indicated non-linear viscoelastic have been developed. Among those, the Generalized Maxwell model(GMM) has been widely used. In these models, several Maxwell elements are assembled in parallel. Some studies employed the direct application of either two-arm or three-arm GMM to fit their experimental data [34], [43]–[46].

Some researchers analyzed the hyper-viscoelastic property [22], [35], [46]–[50], by conducting unconfined compression test, tensile to failure tests as well as relaxation tests. Under those mechanical tests, hyperelastic models(Mooney-Rivilin [35], [46], [49], [50], Yeoh [47], [51], Ogden [48]) and Prony series are used very often. Hyper-viscoelastic models can capture the time-dependent and nonlinear responses of thrombus to mechanical loads, allowing for a more precise description of its behavior under varying conditions [52]. More precise predictions for thrombus behavior could be made with hyper-viscoelastic modeling, which can be important for clinical decision-making and the creation of therapeutic therapies.

1.7. The aim of this study

With EVT becoming the new standard of care for stroke, and with numerous studies showing that the success of thrombectomy may be significantly influenced by the mechanical properties of the occluding thrombus, there is a need to explore thrombus analogues for mechanical testing before surgery to aid in treatment planning. The limited availability of clots in patients makes it impractical to conduct experiments, therefore employing clot analogues is essential for systematic mechanical testing under various loading scenarios. Besides, clot analogues are considered to provide insight into the testing and design of these therapeutic devices [22], [51]. By connecting mechanical properties and image characteristic parameters, surgeons are able to have a better understanding of the thrombus in the patient's brain before surgery. This can be used as a theoretical basis to design better surgical instruments and formulate feasible steps in the future, which will ultimately significantly improve the success rate and prognosis of surgery. Furthermore, with the aid of in-silico models, hyper-viscoelasticity could be investigated to predict the behaviors of thrombi in thrombectomy

The primary objectives of this study are twofold: firstly, to establish a correlation between clinical imaging characteristics observed in real thrombi and the mechanical properties of in vitro thrombus analogues. This correlation aims to enhance pre-surgical planning for clinicians by providing a deeper understanding of the relationship between clinical imaging features and mechanical properties. Secondly, the study employed computational models to investigate the mechanical behaviors of thrombus analogues. This dual-focused approach not only addresses the growing significance of mechanical properties in thrombectomy success but also aids in predicting and comprehensively studying the mechanical responses of thrombus analogues through computational simulations.

2

Material and methodology

In this chapter, a comprehensive outline of the methodology employed in this study is presented. This approach commences with the generation of thrombus analogues from the selected patient cohort, followed by the conduct of five distinct mechanical tests on these analogues. The clinical image analysis and the relationship between mechanical properties and image characteristics are also addressed.

While clots are removed during a mechanical thrombectomy, they are subjected to tensile stress and compression stress [46]. Therefore, understanding how the specimen changes under different mechanical conditions is important to surgical outcomes. Then the investigation extends to the extraction of CT parameters, which were subsequently utilized to establish correlations between these parameters and the mechanical properties of the thrombus analogues. Nowadays, it is hypothesized that mechanical, histological, and imaging measurements can describe thrombus characterization [53], [54]. Among them, radiological imaging is known as the most direct way to get insight into the thrombus because it is part of the standard protocol for diagnosing patients with acute ischemic stroke [8]. As an additional aspect of this research, the section details the development of computational models, serving a pivotal role in advancing the understanding of the mechanical behavior of thrombus analogues.

2.1. Patient selection

Patients with AIS who visited the emergency room of the intervention center at Erasmus MC were included in this study. The experimental data collection of this project started from August 2022 to December 2022, with a total of 29 patients.

Subjects were eligible to participate in this study if they met all of the following criteria: 1) Adults (over the age of 18); 2) Underwent EVT (using any device); 3) At least one thrombus was removed from the site of the target occlusion during thrombectomy; 4) The acute ischemic stroke was caused by a proximal intracranial occlusion of the anterior circulation (ICA, ICA-terminus, M1, M2, and/or M3) as confirmed on admission CTA; 5) A mechanical characterization was initiated within 12 hours after the thrombectomy being completed. A potential participant who fitted any of the following requirements was not allowed to take part in this study: 1) The size of the retrieved thrombus was too small that no mechanical characterization could be performed; 2) Patients who did not give informed consent for the use of their data for this study. The number of people involved in different experiments is shown in **Appendix A**.

2.2. Thrombus analogues

Thrombus analogues were created to perform mechanical tests. For each mechanical test (fracture, compression, and tensile), separate specimens were created. These mechanical tests will be explained in the next section.

A tube of arterial blood was taken from the patient: By increasing the ultimate concentrations of calcium chloride and thrombin in the whole blood to 17mM and 1U/mL, respectively, coagulation was initiated. Whole blood was added to tensile molds that were lined with Velcro tabs in order to create fracture and tensile specimens. Besides, whole blood was infused into syringes to create compression

specimens (Figure 8(a)). At 37 degrees, all samples were allowed to contract after being created at ambient temperature (Figure 8(b)). The detailed protocols are introduced in **Appendix B**. Several weight measurements were conducted to quantify the extent of the analogue contraction ratio, as shown in Figure 7, including the weight of an empty syringe, the weight of a syringe filled with both clot and serum after incubation, and the weight of the clot following its separation from excess serum after removal from the syringe. The percentage of contraction was determined by dividing the weight of the isolated clot by the weight of the clot combined with serum, utilizing the following formula:

$$Contraction = 1 - \frac{W_{clot}}{W_{clot} + W_{serum}} \tag{2.1}$$

where W_{clot} and W_{serum} are the weight of clot and serum, respectively. Hence, a greater analogue contraction ratio, associated with a higher proportion of residual serum, signifies a decreased size of the analogue material.

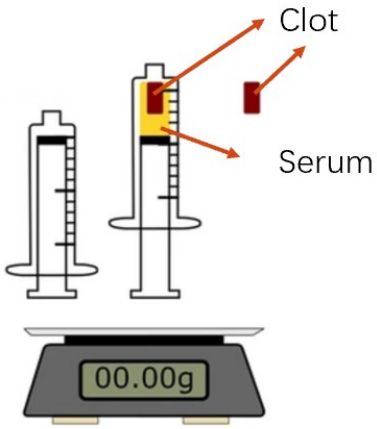

Figure 7: Schematic of the weighting of empty syring, blood clot analogue (red), and serum (yellow).

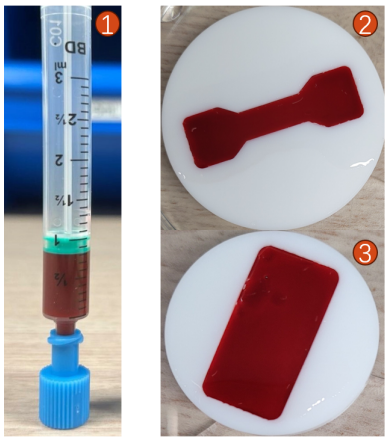

(a) Samples before incubation

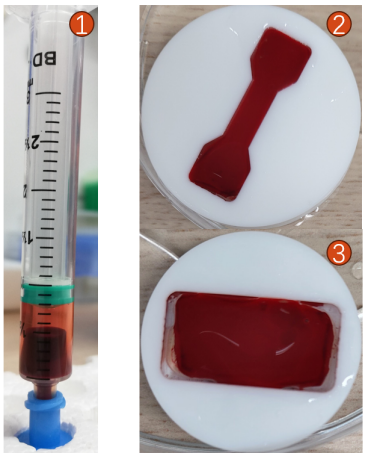

(b) Samples after incubation

Figure 8: Before incubation samples (left) should look like: ❶ 3mL Syringe - compression samples; ❷ tensile sample; ❸ fracture sample. After 1 hour incubation at 37 degrees samples (right) should look like: ❶ 3mL Syringe - compression samples; ❷ tensile sample; ❸ fracture sample.

2.3. Mechanical tests

2.3.1. Unconfined cyclic compression test

To evaluate the stress-strain behavior and relaxation behavior of the samples, a specialized mechanical tester was created. Both hardware and software can be adjusted to the specific needs of the experiment. It has five main components, see Figures 9 A and 9 C, from top to bottom: actuator, load cell, compression plate, and sample stage with a heating container.

The actuator is a step motor with a maximum vertical force of 200N, a stroke of 150mm, and a resolution of 0.01mm. It also has an integrated controller that can handle 10 digital inputs and 6 digital outputs, as well as an electromagnetic brake to stop accidental vertical movement in the event of a power failure [55]. The S-beam load cell works on the strain gauge concept, which states that the deflection of a beam in the load cell causes a rise or reduction in the resistance of the excitation voltage, resulting in a change in the output signal [55]. The compression plate serves as a bridge between the load cell and samples; it can transfer the force between two terminals. Samples were placed on a platform inside a heated container. A temperature-controlling mechanism that regulates itself is in charge of this heated container, keeping the temperature of the bath at around 37 degrees.

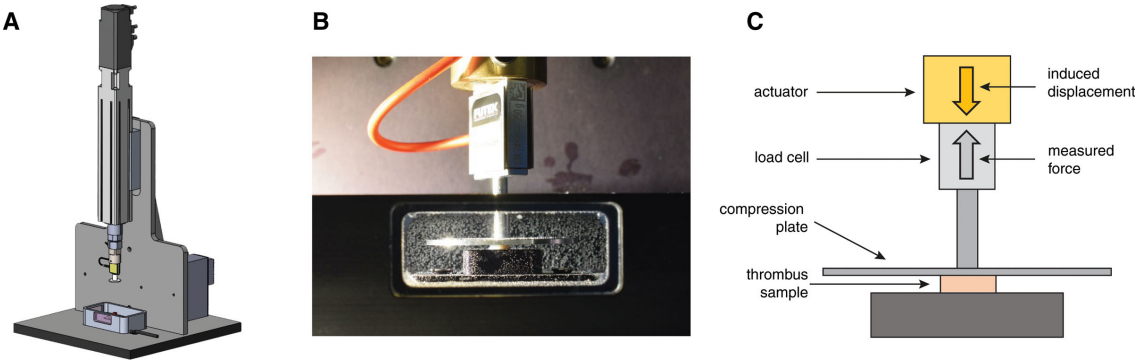

Figure 9: Mechanical compression tester. Adopted from Boodt $et\ al$ [56]. A. Overview of technical drawing, B. Front view of an experiment with compression, C. Overview of main parts

Regarding the specimens, the solid component of the thrombus was trimmed to a uniform height of 2 millimeters for subsequent testing. Following the trimming process, the specimens were photographed in the presence of a ruler while immersed in a HEPES buffer. This photographic documentation was employed to calculate the cross-sectional area of the specimens, expressed in square millimeters [mm^2], as illustrated in Figure B2(b). The specimens were carefully positioned on a platform situated within a temperature-controlled water bath, filled with HEPES buffer maintained at 37 degrees. Subsequently, the specimens underwent controlled compression to a predetermined level of strain, in adherence to a pre-established experimental protocol, as stated in **Appendix C**.

Besides, clot contraction was assessed gravimetrically using the compression specimens prior to testing by following the protocol introduced in Section 2.2, as shown in Figure 7.

To evaluate the stress-strain behavior of the samples, the displacement-controlled plate compressed the sample up to 80% of its initial height, at a strain rate of 10% per second. The plate moved periodically for 20 loops. By studying the hysteresis areas and hysteresis ratio, the viscoelasticity can be investigated. Hysteresis area is defined by the area within the loading-unloading curves in the first loop, while hysteresis ratio is a dimensionless quantity that characterizes the proportion of hysteresis area relative to the total area under the loading curve [57]. The hysteresis area and ratio of a stress-strain curve can provide insights into the energy dissipation within a material during cyclic loading and unloading, indicating the energy loss as the material undergoes deformation, which is particularly relevant in materials exhibiting viscoelastic or hysteretic behavior [57]. The larger the hysteresis area, the more energy is dissipated as heat within the material. Furthermore, the measurements included the quantification of sample deformation (strain) and the calculation of the corresponding force applied by the tissue to the compression plate. The determination of high-strain stiffness [Pa] was accomplished by computing the tangent of the curve spanning from 75% strain to 80% strain (E_{t75}-E_{t80}), with consideration for the thrombi that undergoing large strains in practical surgeries. Likewise, the evaluation of

low-strain stiffness [Pa] was executed by determining the tangent of the curve ranging from 0% strain to 10% strain (E_{t00}-E_{t10}). The stress σ in this test is expressed as:

$$\sigma = \frac{F}{A_0} \tag{2.2}$$

in which F is the recorded load [N] by the load cell and A_0 is the cross-sectional area [m^2] of the sample before compression. The stain ε is calculated by:

$$\varepsilon = \frac{l - l_0}{l_0} \tag{2.3}$$

where l is the sample height [m] after compression and l_0 is the starting height of the sample [m]. The method to select starting points of compression tests is introduced in **Appendix E**

2.3.2. Compression relaxation test

The tissue's ability to reconfigure depends on its viscoelasticity as the thrombus is incorporated into the stent struts or drawn into an aspiration catheter [24]. When held under continuous strain or deflection, the tendency of a material to reduce load generation is known as stress relaxation [58]. To investigate the viscoelasticity of the thrombus analogues, compression relaxation tests were conducted. With the same setup as the cyclic compression test, during the test, the sample was compressed to 60% of its initial height, which was then maintained for 300 seconds. The curves depicting the variation of the force applied to the load cell over time were recorded.

This curve was used for fitting a two-term Prony series to extract related parameters for subsequent stages of viscoelastic computational modeling. Prony series is a function g(t) used to illustrate time-dependent viscoelasticity behavior. The two-term Prony Series (N=2) are given by [59]:

$$g(t) = g_\infty + \sum_{i=1}^{N} g_i \cdot e^{-t/\tau_i} \tag{2.4}$$

and

$$g_\infty = 1 - \sum_{i-1}^{N} g_i \tag{2.5}$$

where g_∞ is the equilibrium modulus, g_i and τ_i are material parameters.

2.3.3. Uniaxial tensile test to failure

With the help of specially designed equipment, tensile experiments were carried out, as shown in Figure 10. It also has five main components: from top to bottom: an actuator, two clamps, samples, a temperature-controlled water bath, and a load cell.

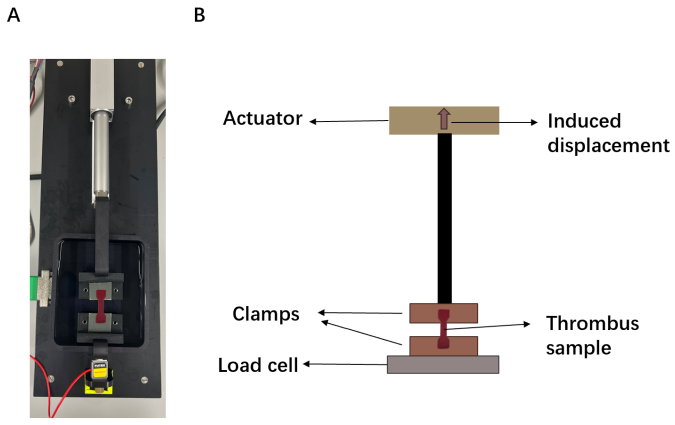

Figure 10: Mechanical tensile tester; the two clamps are used to fix the samples with Velcro tabs. A. Top view of an experiment with tension, B. Schematic overview of main parts

The two clamps are used to fix the samples with Velcro tabs, while the samples are either dog bone-shaped or rectangular-shaped with a crack on them, as shown in Figure D3. The rest of the components are the same as those used for the compression tester described in the previous section.

During tests, the samples were submerged in physiological solution HEPES buffer at 37 degrees and clamped together with Velcro tabs. An ultrasound scan was conducted using a Vevo 3100 Imaging System with an MX550S transducer (FUJIFILM VisualSonics, Canada) to calculate the sample cross-sectional area [mm^2]. The specific steps are described in **Appendix D**.

During the tensile test to failure, the program was terminated once the sample was broken completely. Therefore, the complete curve of the force exerted on the load cell as a function of time was recorded. By deciding the start time and end time (the time the sample started to break), the test duration t was determined. With the known speed v, the induced displacement l is given by:

$$l = vt \tag{2.6}$$

Strain ε is given by Equation 2.3.

Furthermore, stress σ is given by Equation 2.2 with the known cross-sectional area [mm^2] that was measured by Vevo 3100 Imaging System. After that, the tensile stiffness [Pa] was calculated by $\frac{\sigma}{\varepsilon}$. Moreover, the moment that the sample started to break could refer to ultimate tensile strain and ultimate tensile stress [Pa].

2.3.4. Tensile relaxation test

During the tensile relaxation test, the sample was stretched to 125% of its original length and lasted for 300 seconds. The force-time curve was recorded, and it followed the same processing procedure as the compression relaxation test (Section 2.3.2). Two-term Prony series (Equations 2.4 and 2.5) are used to determine viscoelastic and time parameters.

2.3.5. Fracture test

Fracture toughness characterizes a material's capacity to prevent the advancement of pre-existing cracks [60]. Fracture toughness experiments were carried out using the same custom-built set-up used for tensile testing. A crack was introduced in the middle of the fracture sample using a blade, as shown in Figure D.3(b). Following the procedure introduced in **Appendix D.4**, samples were stretched until failure to record the propagation of the crack across the sample. The fracture toughness [J] is represented by the area under force [N] and displacement [mm] curves (purple area in Figure E3). The method to select cracking points of fracture tests for fracture toughness calculation is introduced in **Appendix E**

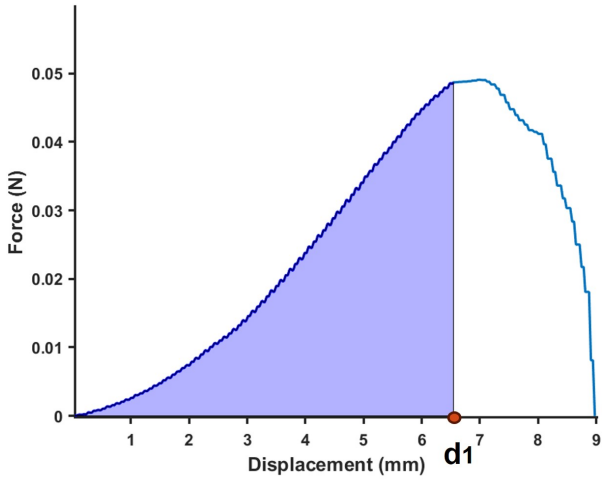

Figure 11: The typical Force(N)-Displacement(mm) obtained from fracture test. The area under the curve (purple) is the fracture toughness and the d_1 is the ending point of this test.

2.4. Constitutive and computational models

The finite element analysis of the compression sample and the tensile sample has been performed by using the C3D8H elements in ABAQUS/standard (2018, Dassault Systèmes Simulia Corp.). Simulations were performed with the samples shown in Figure 12.

An initial evaluation of well-established hyperelastic material models indicates that the Yeoh model offers a reasonably precise fitting to the unconfined compression test outcomes for thrombus analogue materials [47], [51].

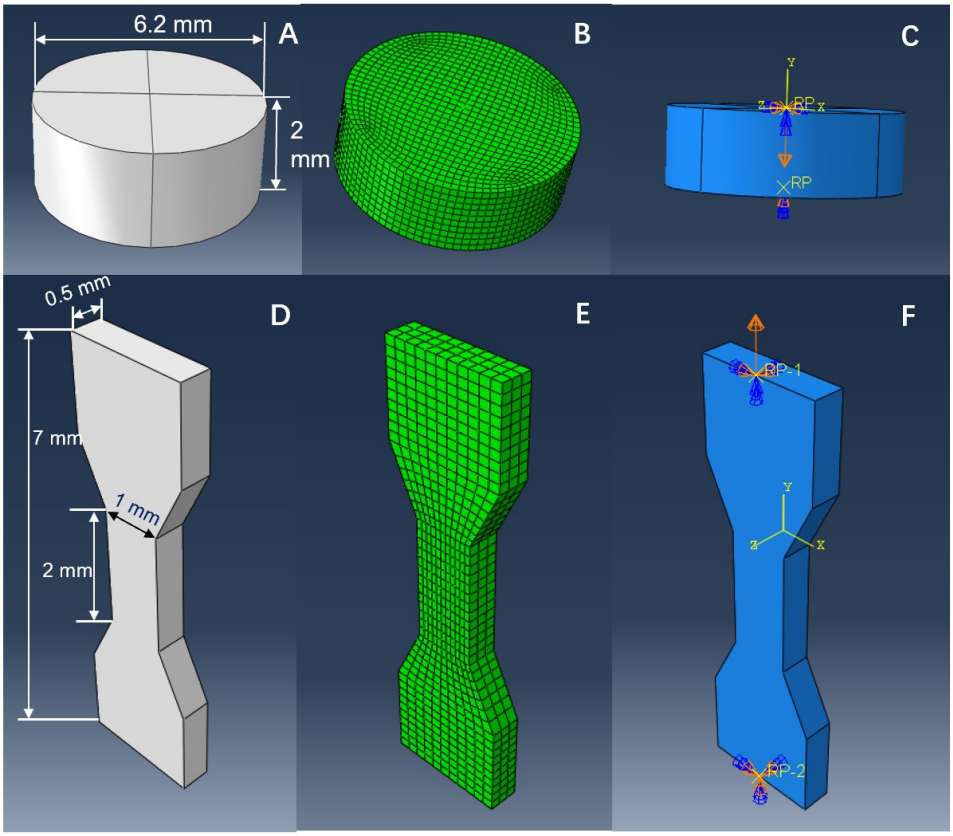

Figure 12: The FEM models of compression sample and tensile sample. A. Geometry of compression model: radius is 3.1 mm and height is 2 mm; B. Mesh of compression model, with the element type C3D8RH; C. In the boundary condition of compression models, the bottom is fixed and the top is compressed to 80% (-1.6mm). D. Geometry of the tensile model; E. Mesh of the tensile model, with the element type C3D8RH; F. In the boundary condition of the tensile model, the bottom is fixed and the top is stretched to a certain strain.

2.4.1. Hyperelastic and stress-relaxation model fitting

Compressible Yeoh's (n=3) strain energy function (W) and Prony series (n = 2) were employed to simulate the viscoelastic and hyperelastic response of the thrombus analogues:

$$W = c_1\left(\bar{I}_1 - 3\right) + c_2\left(\bar{I}_1 - 3\right)^2 + c_3\left(\bar{I}_1 - 3\right)^3 + \frac{1}{d_1}(J-1)^2 + \frac{1}{d_2}(J-1)^4 + \frac{1}{d_3}(J-1)^6 \tag{2.7}$$

where $\bar{I}_1$ and J are the first deviatoric strain invariant and volumetric change, respectively. c_1, c_2, c_3 and d_1, d_2, d_3 are hyperelastic material constants.

2.5. Thrombus imaging characteristics

This section will describe how the CT scans of patients who underwent thrombectomy were analyzed in order to extract in vivo clot imaging characteristics.

Before imaging characteristics collection, in order to assess the thrombus features on the NCCT and CTA simultaneously, two scans have to be co-registered by Elastix's rigid registration [61]. Subsequently, to extract imaging parameters, three regions of interest (ROIs) were defined. As shown in Figure 13, the red marker is the location of the terminus of the intracranial carotid artery (ICA-T). Secondly, in the case of a curved vessel extending up to the proximal thrombus border, a maximum of three optional green markers should be placed. Additionally, position three blue markers at the proximal, middle, and distal segments of the thrombus, a single yellow marker at the proximal thrombus border, and one turquoise marker at the distal thrombus border. Those markers were manually selected by using the software ITK-snap (version 3.8).

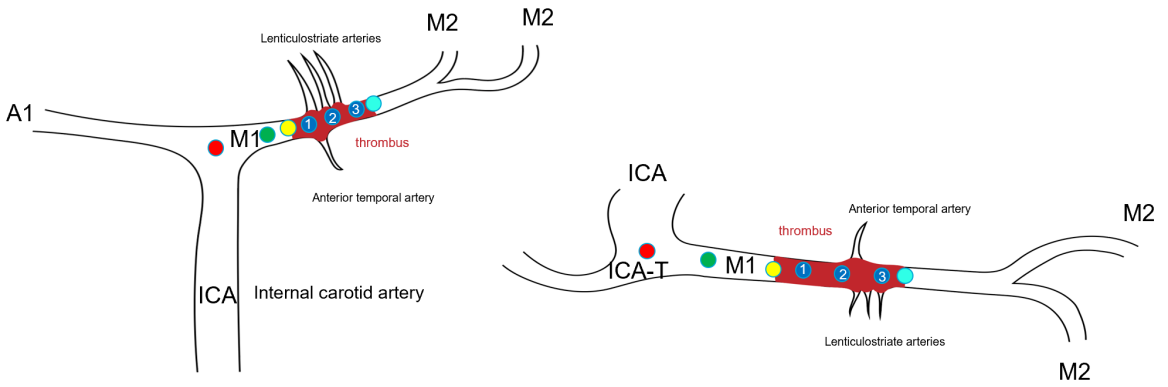

Figure 13: Schematic of how to put markers in two views: on the left is the coronal view and on the right is the axial view. The red marker is the location of ICA-T; in the case of a curved vessel extending up to the proximal thrombus border, a maximum of three optional green markers should be placed; three blue markers at the proximal, middle, and distal segments of the thrombus; a single yellow marker at the proximal thrombus border; and one turquoise marker at the distal thrombus border. Adopted from Arrarte Terreros [62]

Within the scope of this investigation, a comprehensive assessment was undertaken to evaluate a range of critical parameters. These parameters include the measurement of the distance from the ICA-T to the thrombus (DT), the determination of thrombus length, an analysis of thrombus perviousness, and its attenuation. Furthermore, the study involves the quantification of densities within three ROIs on both CTA and NCCT scans. Additionally, the investigation involves the calculation of the mean value of densities within the three ROIs specifically on the CTA images.

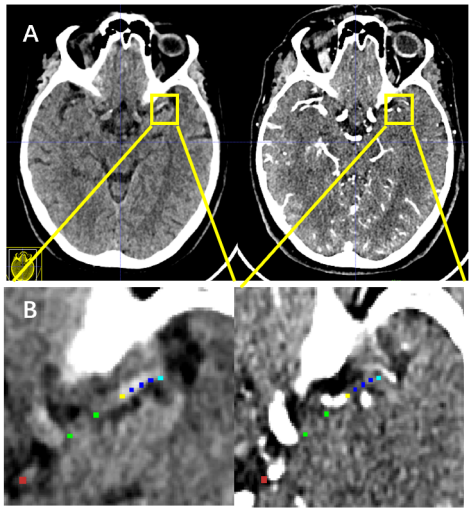

Figure 14: Thrombus imaging measurements with manual-selected markers. A: NCCT (left) and CTA (right) scans of an AIS patient. B: Zoom in the thrombus region. One red marker at ICA-T, two green markers were located along the path to the thrombus, a yellow marker at the edge of the thrombus, three blue markers were put on the thrombus, and one turquoise marker at the distal thrombus border.

The distance between the ICA-T and the closest thrombus boundary is used to define DT. In Figure 22, DT is the distance between the red marker and the yellow marker.

Thrombus length, which with the help of the HAS if it was seen on the co-registered NCCT, is defined as the longest extension where there's no contrast-filled area seen in a CTA image [63]. The HAS has been a recognized diagnostic indicator of occlusive thrombi in cases of acute ischemia as observed on NCCT scans for an extended period [64]. It refers to focal hyperattenuation of the middle cerebral artery on NCCT [65]. Therefore, the length is obtained by summation of the distances between the yellow (start of thrombus) marker and the turquoise (end of thrombus) marker.

Thrombus perviousness in CTA is a quantification of contrast penetration relative to NCCT, indicating how much contrast has infiltrated the thrombus. Thus, perviousness, as determined by single-phase imaging, represents the permeability of the thrombus for contrast material [62], [66], [67].

In terms of thrombus attenuation and permeability, these two parameters can be calculated by using 3 blue markers with the unit of Hounsfield Unit [HU]. According to Dutra and colleagues, thrombus attenuation was determined by averaging the attenuation values within specified ROIs on NCCT scans. Thrombus perviousness, on the other hand, was derived by subtracting the mean attenuation values from the ROIs in NCCT scans from those in CTA scans [54].

2.6. Statistical analysis

Shapiro-Wilk analysis was conducted to evaluate the distribution of continuous data, employing a statistical method to assess the normality of the data's distribution.

The study systematically investigated the correlation between the mechanical properties of thrombi, including high-strain stiffness, low-strain stiffness, ultimate tensile strain, ultimate tensile stress, tensile stiffness, and thrombus imaging characteristics. The imaging parameters examined encompassed perviousness, thrombus attenuation (mean NCCT density), mean CTA density, and densities of proximal, middle, and distal regions in both NCCT and CTA. This correlation analysis was conducted employing statistical methods, specifically the Spearman Rank Correlation.

The Spearman Rank Correlation and Shapiro-Wilk analysis were conducted using GraphPad Prism (version 8.0.1 for Windows, GraphPad Software, San Diego, California USA).

3

Results

In this chapter, a comprehensive analysis of mechanical data obtained from compression tests, tensile tests, and fracture tests is presented. The computational models employed in the study are showcased as a supplement. Furthermore, intricate imaging characteristics are meticulously extracted and detailed. Notably, this chapter also delves into the correlation between the mechanical properties derived from the tests and the extracted imaging characteristics, elucidating the complex interplay between the physical attributes and the observed visualized features. Through this multifaceted analysis, a deeper understanding of the material behavior and its correlation with imaging data is achieved, offering valuable insights for future research and practical applications. The detailed mechanical data and range of all kinds of parameters are presented in **Appendix F**.

3.1. Mechanical characteristics

In the context of the entire cohort comprising 29 patients, mechanical testing was conducted on thrombus analogues from 23 of these individuals (79%). Among the 23 patients, the mechanical evaluations encompassed three specific testing protocols: cyclic compression, tensile to failure, and fracture testing. It is imperative to note that the results of two distinct relaxation tests were excluded from the correlation analytical phase. Eventually, 23 out of 29 samples (79%) underwent both unconfined compression tests and compression relaxation tests, 21 out of 29 samples (72%) underwent fracture tests, 20 out of 29 (69%) underwent the tensile test, and 19 out of 29 (66%) underwent tensile stress relaxation. It is noteworthy that a total of 18 patients (60%) completed the comprehensive suite of all three testing modalities. A thorough evaluation of thrombus analogues performance was made possible by the carefully planned experimental design and sample selection, which also served as a solid basis for further scientific research. MATLAB was employed for post-processing of experimental data files [68]. For the specific flowchart, see Figure A1.

3.1.1. Mechanical tests

In Figure 15, an example showcasing the results obtained from the cyclic compression test and the subsequent data processing for one patient's thrombus analogue is presented. As observed in Figure 15B and Figure 15D, the thrombus analogues displayed a cyclic reduction in stiffness. Besides, cyclic softening was distinctly evident during the first loading cycle, however, the achievement of a cyclic steady state was not clearly established. In Figure 15C, the segment of the Stress(Pa)-Strain curve, indicated by the purple highlighted region at the initial portion, extends from 0% strain to 10% strain. The slope of this segment was utilized for the calculation of low-strain stiffness in the thrombus analogues. Similarly, the final portion of this curve, demarcated by the yellow highlighted region, extends from 75% strain to 80% strain, and the slope of this segment was utilized for the determination of high-strain stiffness in thrombus analogues. The presence of hysteresis from the first loop and decreasing of the hysteresis areas along 20 loops indicates that thrombus analogues exhibit viscoelasticity [25]. Furthermore, Figure F1 shows that all the samples from patients exhibited viscoelasticity.

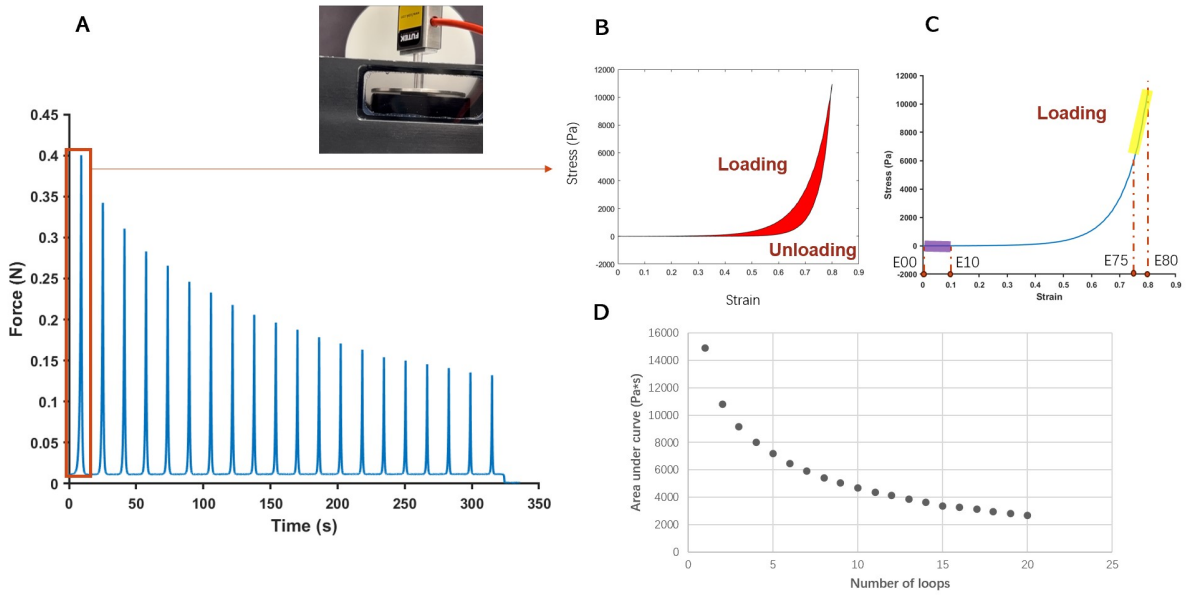

Figure 15: The example of cyclic compression tests. A. Force(N)-Time(s) curve of twenty loops cyclic compression test; B. Hysteresis phenomenon under the stress-strain curve of the first loop, the red part is the hysteresis area; C. The loading part of the first loop: the slope of the purple highlight on the left is used to calculate low-strain stiffness, and the slope of the yellow highlight on the right is used to calculate high-strain stiffness; D. The variation in the area under the Force(N)-Time(s) curve for each of the 20 cycles.

The Force-Time curve acquired during the cyclic compression test did not start at precisely zero Newtons but rather at approximately 0.01 Newtons. This discrepancy can be attributed to the water tension, and the sensor's sensitivity, as even in a stable air environment, the force reading initiates at 0.001 Newtons. Nonetheless, this initial value does not impact the ultimate determination of high-strain stiffness and low-strain stiffness, as both values were derived from the slope of the stress-strain curve. Additionally, certain high-strain stiffness and low-strain stiffness results were removed due to their poor alignment with the linear stress-strain curve.

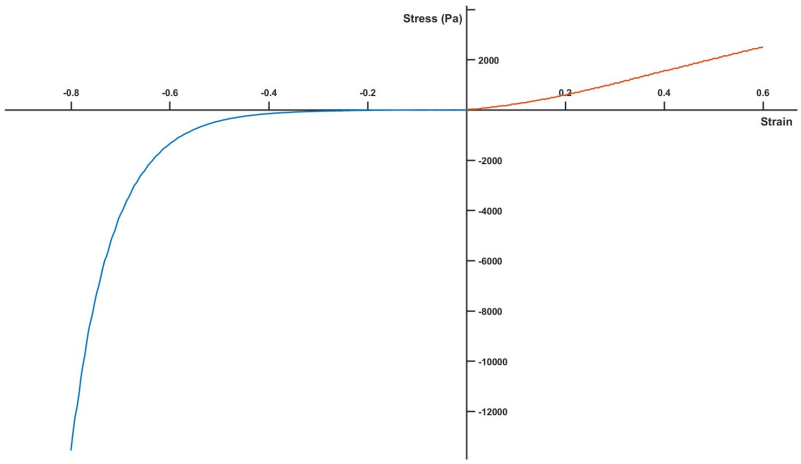

Figure 16: The example of complete curve containing stress-Strain from the first loop of cyclic compression test and tensile test to failure. Red line: tensile test to failure; Blue line: first loading part of a cyclic compression test.

High-strain stiffness and low-strain stiffness are key indicators of the thrombus analogue's mechan-

ical response to different levels of strain. The median values and percentiles (25%-75%) measure the typical range of stiffness exhibited by thrombus analogues. As shown in Table 3.1, high-strain stiffness is more widely dispersed than low-strain stiffness because of the bigger IQR. This find can also be verified with Figure F9. Besides, the patients' high-strain stiffness (range from 6.19E+04 to 2.89E+05 Pa) exhibited a wider range, while low-strain stiffness (range from 163.30 to 1.63E+03 Pa) had a similar range to healthy people with comparison to Cahalane $et\ al.$ [69] (high-strain stiffness range from 1.22E+05 to 3.12E+05 Pa and low-strain stiffness range from 140 to 1.29E+03 Pa).

Hysteresis area and hysteresis ratio are the measures of the material's viscoelastic behavior during cyclic loading and unloading. The median and percentiles describe the extent of energy dissipation within the material, providing insights into its ability to absorb and dissipate mechanical energy. This study observed the hysteresis that had also been documented in earlier studies throughout the unloading process [22], [46], [70], [71].

Likewise, an example is presented (Figure 17), illustrating the outcomes derived from the tensile tests and the subsequent data analysis of a single patient's thrombus analogues. As shown in Figure 17B, the thrombus analogue displayed stress-strain behavior that was almost linear, this find is in agreement with several research [72], [73]. In addition, the discovered properties, which demonstrated that the samples could be stretched to over twice their initial length before breaking, were in good agreement with the findings reported in the literature [27], [46], [74]. As shown in Figure 16, the thrombus analogues typically exhibited greater stiffness when subjected to axial compression loading in comparison to tensile loading. This phenomenon is also consistent with the results obtained in the literature [75].

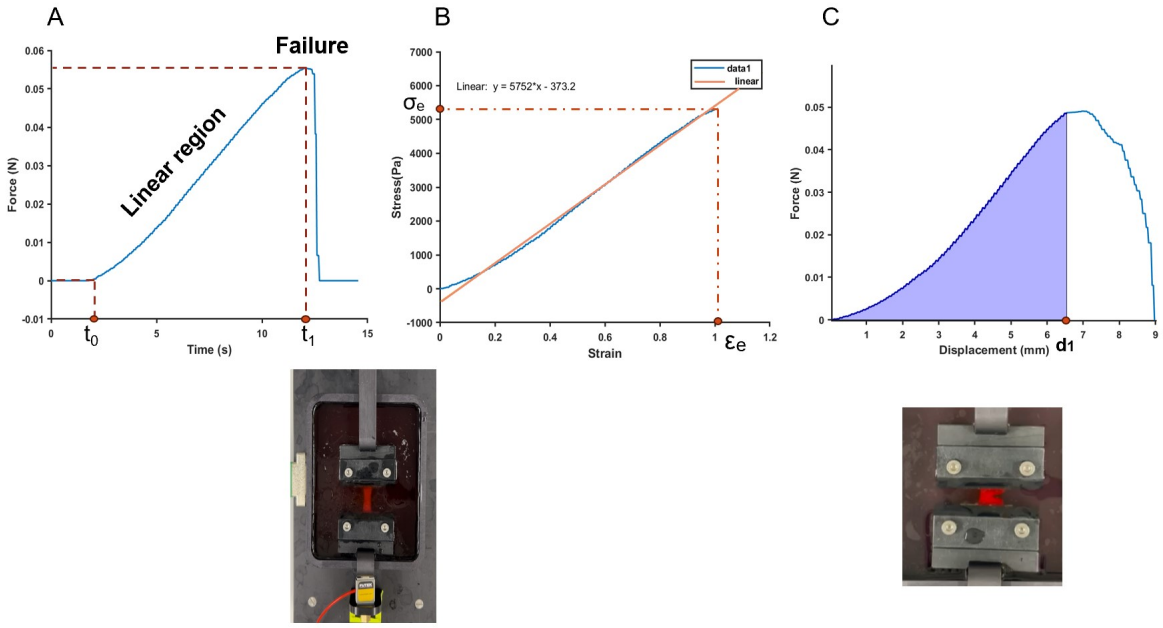

Figure 17: The example of tensile tests. A. Complete Force(N)-Time(s) curve of tensile test to failure. t_0, and t_1 are starting point and ending point, respectively; B. Stress(Pa)-Strain curve derived from time period t_0 to t_1. The orange straight line: the linear fitting curve, thus the slope of this linear line was used to calculate tensile stiffness. ε_e and σ_e represent ultimate tensile strain and ultimate tensile stress, respectively; C. The complete Force(N)-Displacement(mm) curve of fracture test. The purple area is the fracture toughness.

Figure F7 shows the distributions of mechanical parameters. Using the Shapiro-Wilk analysis, the assessment of normality for various mechanical properties was conducted. The results revealed that high-strain stiffness (P=0.87), hysteresis area (P=0.77), hysteresis ratio (P=0.06), tensile stiffness (P=0.56), ultimate tensile strain (P=0.45), and fracture toughness (P=0.06) all exhibited distributions consistent with normality. However, the distributions of low-strain stiffness (P=0.02), analogue contraction ratio (P=0.003), and ultimate tensile stress (P<0.0001) deviated significantly from the normal

distribution, indicating non-normality in these specific mechanical properties. Hence, the analysis utilized Spearman Correlation to investigate the relationships among these variables. This choice was made due to the fact that Spearman correlation evaluates monotonic associations, making it adept at detecting any systematic relationships between variables that exhibit either an ascending or descending trend, irrespective of whether the relationship adheres strictly to linearity or not [76].

Figure 18 illustrates the results of the analysis, revealing notable correlations among various mechanical properties. Specifically, the hysteresis ratio and tensile stiffness displayed a significant negative monotonic relationship (ρ= -0.68, P<0.001) with ultimate tensile stress (ρ= -0.85, P<0.001), and ultimate tensile strain (ρ= -0.83, P<0.001). These findings suggest a strong inverse correlation between these parameters. In contrast, the analogue contraction ratio did not exhibit a significant impact on any of the other mechanical measurements.

Furthermore, the three parameters derived from the tensile test demonstrated a high degree of correlation among themselves, while the two stiffness parameters from the compression test showed statistical significance (ρ= 0.54, P<0.02). This indicates a relationship between the stiffness parameters obtained from the compression test, although it is of a somewhat lower strength compared to the correlations observed within the tensile test-derived parameters.

Table 3.1: Thrombus analogues mechanical measurements. Median and interquartile range (IQR) for high-strain stiffness (Pa), low-strain stiffness (Pa), hysteresis area (Pa), hysteresis ratio, analogue contraction ratio, tensile stiffness (Pa), ultimate tensile stress (Pa), ultimate tensile strain, fracture toughness (J).

	Median (IQR)
High-strain stiffness (Pa)	2.20E+05 (1.80E+05-2.50E+05)
Low-strain stiffness (Pa)	456.75 (371.28-817.30)
Hysteresis area (Pa)	1490.60 (996.57-1755.05)
Hysteresis ratio	0.46 (0.43-0.50)
Analogue contraction ratio	0.58 (0.55-0.61)
Tensile stiffness (Pa)	5.89E+03 (5.10E+03-9.66E+03)
Ultimate tensile stress (Pa)	5.30E+03 (3.19E+03-1.05E+04)
Ultimate tensile strain	0.98 (0.61-1.19)
Fracture toughness (J)	1.36E-04 (9.23E-02-2.63E-01)

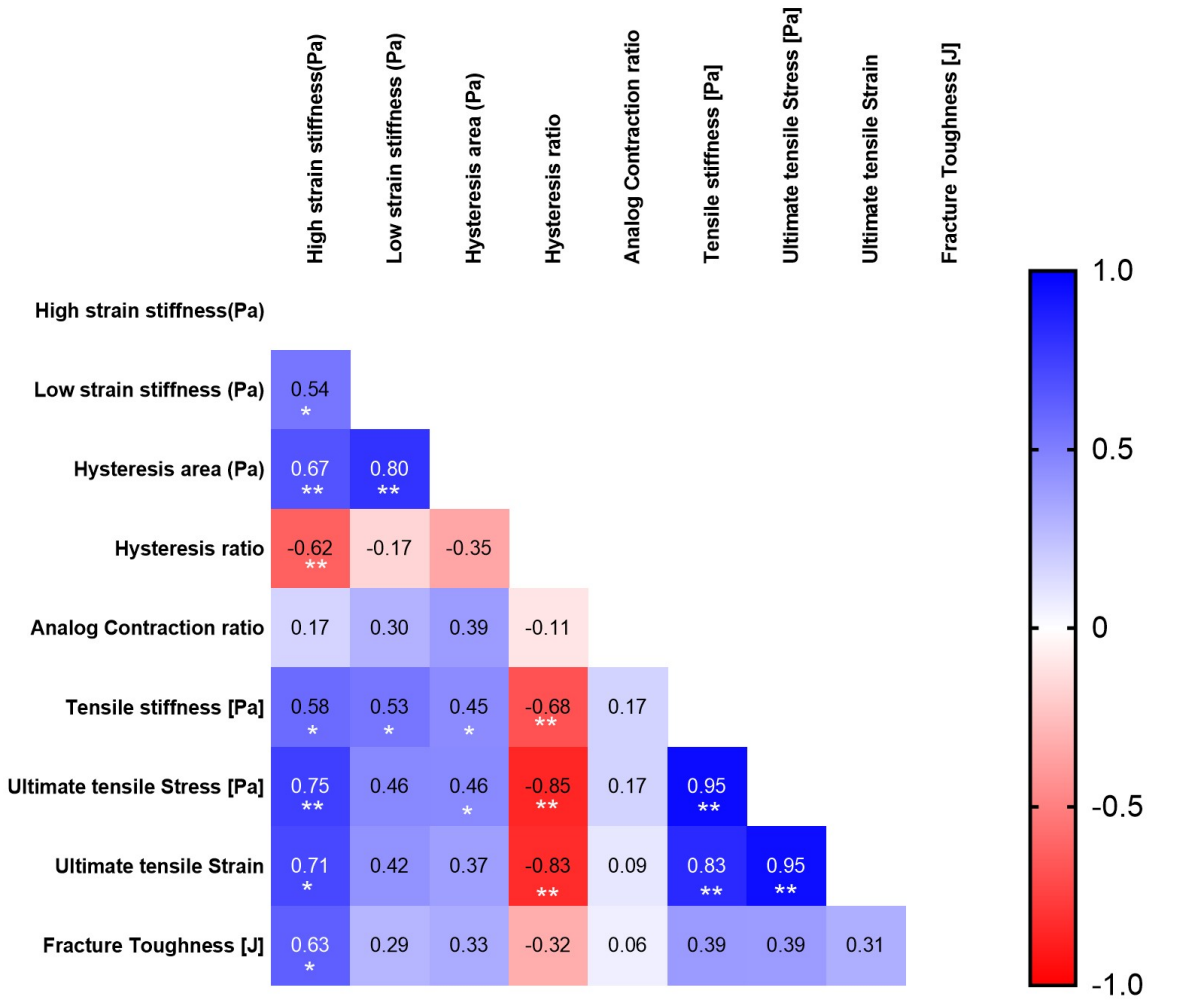

Figure 18: Correlation analysis between mechanical parameters. Spearman's correlation coefficients ρ and significance level: '**', p<0.01; '*', p<0.05; ' ' p≥0.05. The stronger the monotonic association between the two variables under comparison, the closer the ρ is to ± 1, with the darker the color.

3.1.2. Computational models

The fitting process was initiated with the application of the Prony series to achieve optimal fitting of relaxation data. Subsequently, the Yeoh material model was employed to fit the stress-strain curves for the initial loops of both compression and tensile tests.

When modeling compression and tensile samples, conducting a mesh sensitivity analysis is imperative to achieve the optimal mesh refinement for the simulation. A mesh sensitivity analysis, alternatively referred to as a mesh independence or mesh convergence study, entails executing the identical simulation with varying grid resolutions and assessing the extent to which the converged solution alters with each mesh. Conducting a mesh sensitivity analysis offers insight into spatial discretization errors and elucidates the degree to which the mesh exerts an influence on the solution [77].

From Table 3.2, Table 3.3 and Figure 19, it is evident that, for the compression sample, both the reference force and maximum stress reach equilibrium beyond a number of elements of 8640. In the case of the tensile sample, equilibrium is observed in both reference force and maximum stress after a number of elements of 1593.

The visualized results are represented by the von Mises stresses(MPa) of the two sample models after corresponding tests, as shown in Figure 20.

Table 3.2: Mesh sensitivity check for the compression sample

Globe size	Number of elements	Number of nodes	Max Stress (MPa)	Reference Force (N)
1.5	41	81	0.00578001	-0.817218
1	88	165	0.00578001	-0.84178
0.5	560	805	0.0057803	-0.852275
0.4	1200	1590	0.00578207	-0.853354
0.2	8640	10043	0.00578051	-0.85518
0.15	21632	24206	0.00578032	-0.855473
0.1	75440	81291	0.00578026	-0.85567

Table 3.3: Mesh sensitivity check for the tensile sample

Globe size	Number of elements	Number of nodes	Max Stress (MPa)	Reference Force (N)
2	13	42	9.519E-03	0.00188983
0.5	46	130	9.194E-03	0.00151801
0.23	504	887	1.052E-02	0.00145132
0.15	1593	2368	1.140E-02	0.00143742
0.1	6465	8316	1.253E-02	0.00142958
0.08	12612	15533	1.335E-02	0.0014268

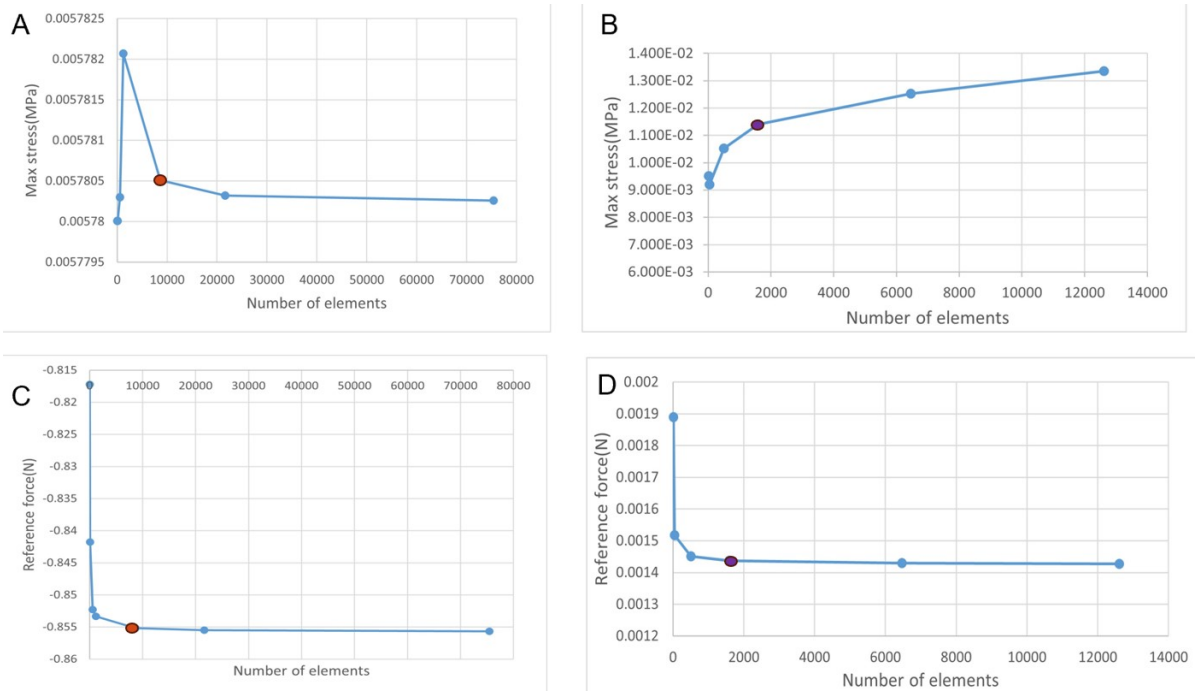

Figure 19: Mesh sensitivity analysis for compression and tensile samples. A. Max stress(MPa)-Number of elements curve of compression sample; B. Max stress(MPa)-Number of elements curve of tensile sample; C. Reference force(N)-Number of elements curve of compression sample; D. Reference force(N)-Number of elements curve of tensile sample. Red points are the number of elements of 8640, and purple points are the number of elements of 1593.

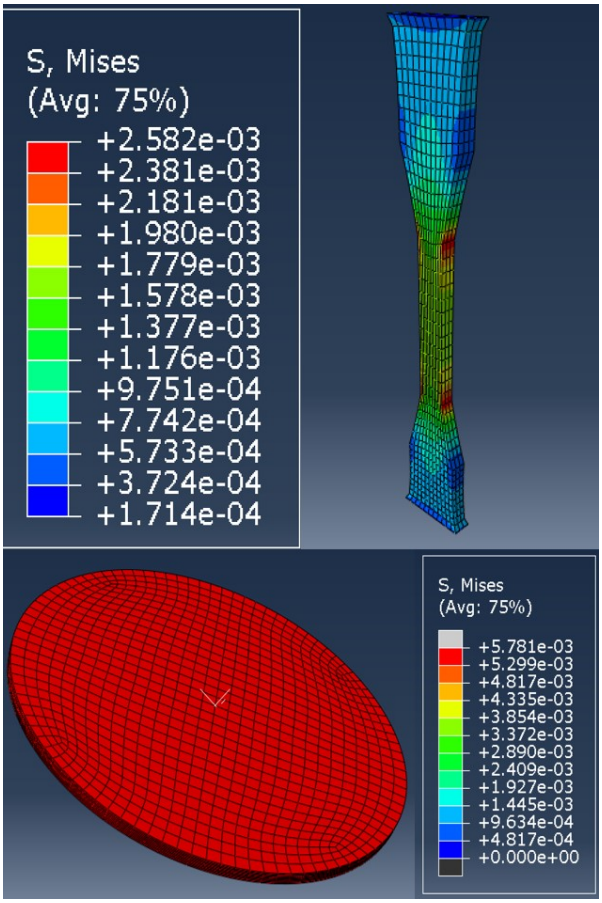

Figure 20: The FEM models of compression sample and tensile sample after tests. Top: Compression model after 80% compression; Bottom: Tensile model after stretched.

Fit relaxed data with two-term Prony series

In this section, a careful procedure for fitting relaxed data using a two-term Prony series is presented. By calculating the R^2, the goodness of fit in regression analysis was accessed. It shows the percentage of the dependent variable's variance that can be accounted for by the model's independent variables. The R^2 calculation formula is as follows:

$$R^2 = 1 - \frac{\sum_{i=1}^{n} (y_i - \hat{y}_i)^2}{\sum_{i=1}^{n} (y_i - \bar{y})^2} \tag{3.1}$$

where n is the number of data, y_i is the experimental value of the dependent variable for the ith observation, $\hat{y}_i$ is the predicted value from Prony series of the dependent variable for the ith observation and $\bar{y}$ is the mean of the experimental values.

The relaxation data was subjected to fitting using the one-term, two-term, and three-term Prony series. Eventually, the two-term Prony series exhibited superior fitting performance while producing the least computational burden, thereby indicating its efficacy for capturing the observed relaxation phenomena. The results presented in the figures and tables show that the two-term Prony series fitting curve can capture the relaxation behavior of the sample (Table 3.4). Additionally, the extracted material parameters for the entire cohort of patients are delineated in Table F3. The visual representations for all patients are elucidated in Figure F5 and Figure F6.

Table 3.4: Material parameters of the two-term Prony series for one patient example.

	g_{inf}	g_1	t_1	g_2	t_2	R^2
Compression relaxation	0.52	0.15	7.48	0.24	141.35	0.9982
Tensile relaxation	0.68	0.11	9.16	0.12	119.70	0.9946

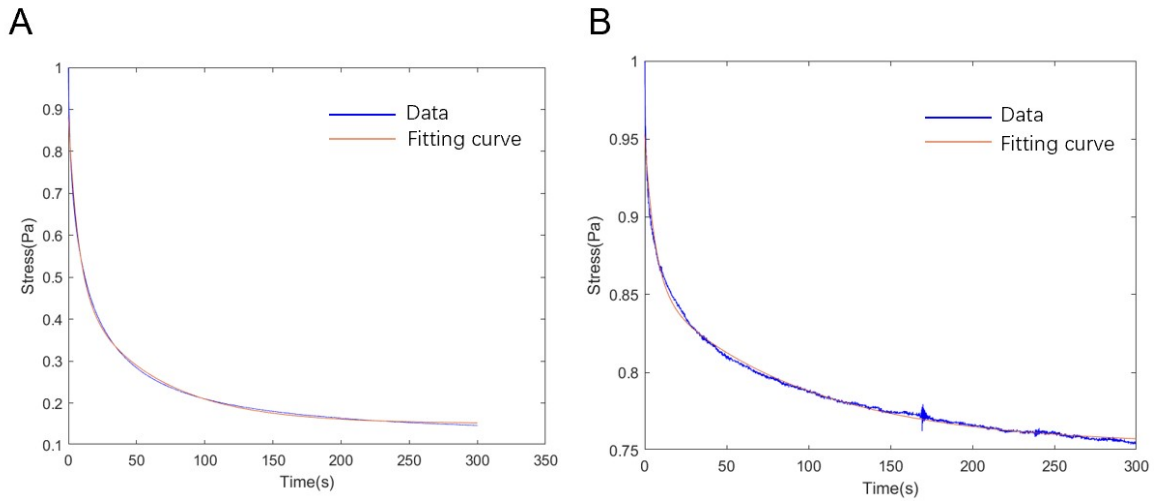

Figure 21: Two-term Prony series fitting to relaxation data. A. Fitting to compression relaxation; B. fitting to tensile relaxation.

Compression and tensile data fitting to 3-term Yeoh material model

The Yeoh model is a typical isotropic hyperelastic material model, therefore, prior research groups have traditionally employed Yeoh material models for the fitting of compression tests [22], [25], [47], [56] or, conversely, tensile tests [36], [46]. In this study, a three-term Yeoh model was concurrently applied to fit both compression and tensile tests.

However, according to Figure G1, the model is only capable of successfully accommodating the results of one of the tests. If the compression test is effectively fitted, the fitting process for the tensile test will prove unsuccessful. In addition, the unsymmetrical shape is shown in Figure 16 as well. The stress-strain behavior of clots exhibited a significant imbalance between tension and compression. Compression stiffness was substantially more than tensile stiffness at high strains, while it was lower at low strains. The Figures and corresponding parameters of the different fit are presented in **Appendix G**. As a result of inadequate fitting of the experimental data in this stage, the subsequent steps will not be addressed in this study.

3.2. Imaging characteristics

There were 13 out of 29 sets of CT images (45%) that were exterminated and extracted imaging characteristics (Figure A2).

The median and IQR of thrombus length were 21.34mm (14.46-29.15mm) (Table 3.5 and Figure F10). It can be observed from the median dataset, that the density values extracted from CTA were notably higher than those derived from non-contrast computed tomography (NCCT). In the IQR dataset, the CTA data exhibited a greater degree of variability compared to the NCCT data.

Summary statistics pertaining to the correlation between thrombus imaging characteristics are presented in Figure 23. Thrombus length exhibits a robust negative monotonic association with perviousness (ρ= -0.88, p<0.001). Additionally, significant statistical correlations were observed between thrombus and density values derived from CTA at different locations, including proximal CTA (ρ= -0.58, p=0.043), middle CTA (ρ= -0.58, p=0.040), and distal CTA (ρ= -0.82, p=0.001).

Furthermore, perviousness demonstrated close relationships with CTA characteristics at distinct locations, with proximal CTA (ρ= 0.68, p=0.013), middle CTA (ρ= 0.62, p=0.0427), and distal CTA (ρ= 0.87, p<0.001). Notably, thrombus attenuation, defined as the mean density value in NCCT, exhibited strong and statistically significant correlations with density extracted from NCCT scans at various locations, including proximal NCCT (ρ=0.97, p<0.001), middle NCCT (ρ=0.91, p<0.001), and distal NCCT (ρ=0.92, p<0.001).

Nevertheless, there is a lack of statistically significant evidence to establish a correlation between the density derived from NCCT and CTA.

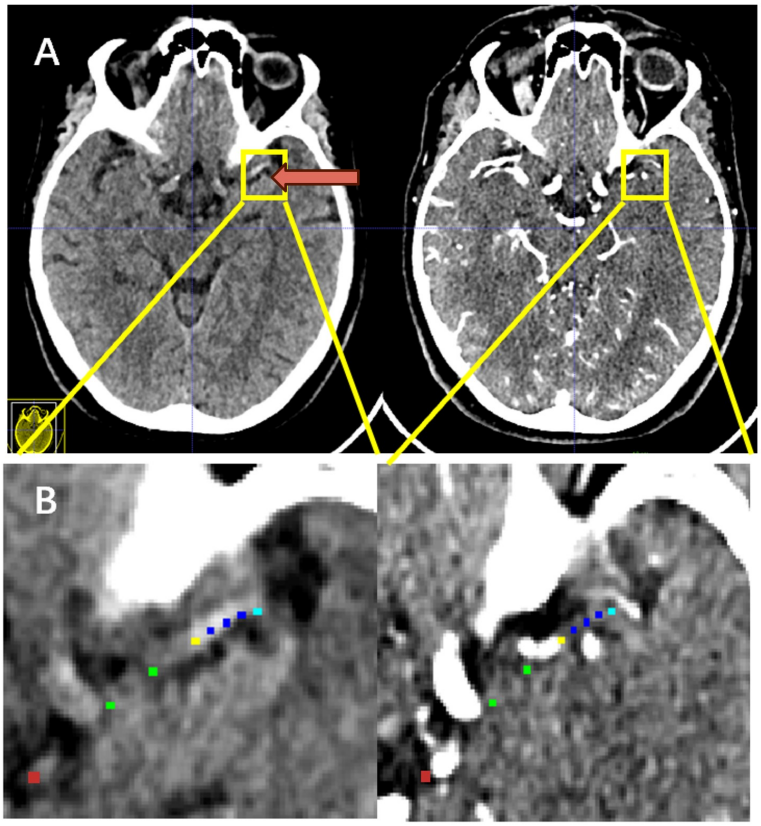

Figure 22: Thrombus imaging measurements with manual-selected markers. A: NCCT (left) and CTA (right) scans of an AIS patient. B: Zoom in the thrombus region. One red marker at ICA-T, two green markers were located along the path to the thrombus, a yellow marker at the edge of the thrombus, three blue markers were put on the thrombus, and one turquoise marker at the distal thrombus border. The part pointed by the red arrow is a HAS.

Table 3.5: Thrombus imaging measurements. Median and interquartile range (IQR) for DT (mm), Thrombus length (mm), Perviousness (HU), Thrombus attenuation (HU), Proximal NCCT (HU), Middle NCCT (HU), Distal NCCT (HU), Proximal CTA (HU), Middle CTA (HU), Distal CTA (HU), Mean density of CTA (HU).

	Median (IQR)
DT (mm)	21.09 (8.99-24.69)
Thrombus length (mm)	21.34 (14.46-29.15)
Perviousness (HU)	14.31 (0.49-27.70)
Thrombus attenuation (HU)	36.23 (29.27-47.42)
Prox NCCT (HU)	34.70 (28.19-50.64)
Mid NCCT (HU)	36.75 (32.18-42.89)
Dis NCCT (HU)	37.46 (30.15-42.62)
Prox CTA (HU)	54.91 (45.89-74.89)
Mid CTA (HU)	53.61 (41.11-68.90)
Dis CTA (HU)	57.64 (40.33-68.21)
Mean density of CTA (HU)	56.33 (44.81-69.07)

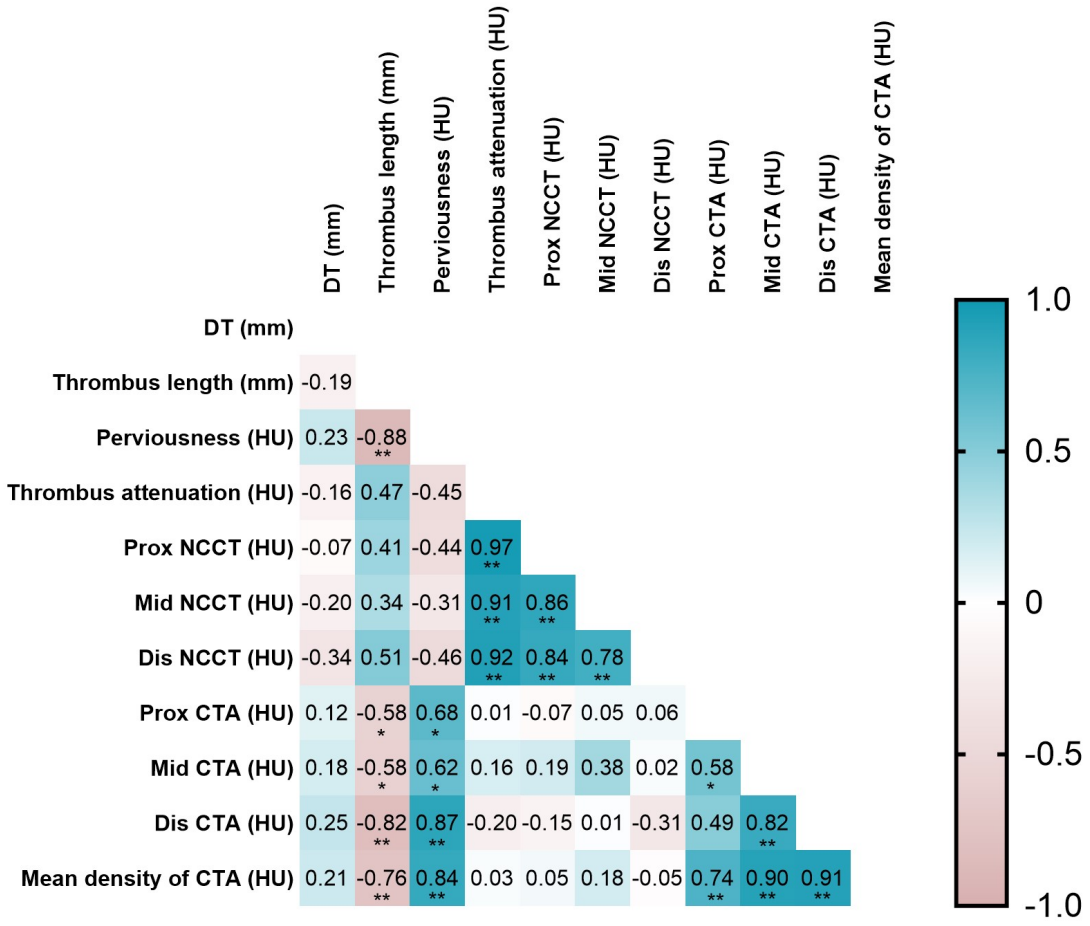

Figure 23: Correlation analysis between imaging characteristics. Spearman's correlation coefficients ρ and significance level: '**', p<0.01; '*', p<0.05; ' ' p≥0.05. The stronger the monotonic association between the two variables under comparison, the closer the ρ is to ± 1, with the darker the color.

3.3. Correlation between mechanical and imaging characteristics

There were 9 out of 29 (31%) cases that studied the correlation between mechanical parameters and imaging characteristics. From Figure 24, it can be concluded that only the analogue contraction ratio had a significant correlation with the middle part of NCCT (ρ=-0.82, P=0.011). In practical terms, this negative correlation indicates that as the analogue contraction ratio increases which means that the analogue becomes denser), there is a tendency for the middle portion of NCCT images to exhibit decreased characteristics. Furthermore, there was no statistically significant relationship found between the perviousness and ultimate tensile stress. Similarly, there was no relationship found between the ultimate tensile strain and thrombus length, perviousness, or thrombus attenuation, nor between low strain stiffness and proximal CTA density (ρ=0).

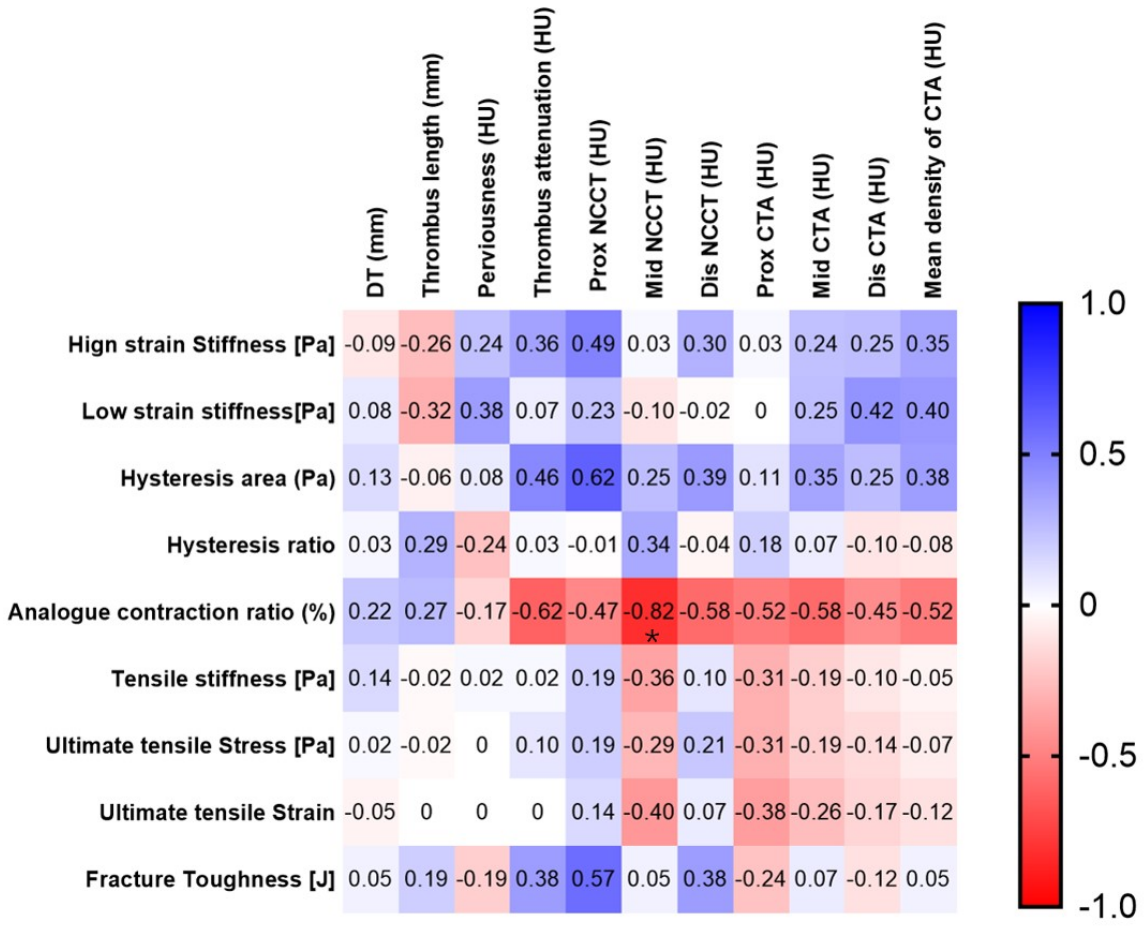

Figure 24: Correlation analysis between imaging characteristics and mechanical measurements. Spearman's correlation coefficients ρ and significance level: '**', p<0.01; '*', p<0.05; ' ' p≥0.05. The stronger the monotonic association between the two variables under comparison, the closer the ρ is to ± 1, with the darker the color.

4

Discussion and limitation

This research has delved into the intricate world of thrombus analysis, bridging the realms of clinical imaging, and experimental investigation. This comprehensive journey began with the examination of thrombus CT characteristics derived from patient data. By employing patient blood to create thrombus analogues and conducting a series of mechanical tests on these analogues, the field of in vitro experimentation was explored, offering a unique perspective on thrombus mechanics. The primary objective was to find out the correlation between CT-derived parameters from real thrombi and the mechanical properties of thrombus analogues.

4.1. Discussion

4.1.1. Mechanical properties

The mechanical tests conducted on the patient-specific blood analogues yielded insightful results across various parameters. Because of the structural principles of fibrin networks, thrombus analogues behaved mechanically very differently under compression and tensile loadings [46].

Within the cyclic compression test, the high- and low-strain stiffness exhibited distinctive values under different loading conditions, the high-strain stiffness has a wider IQR range (1.80E+05-2.50E+05Pa) than the low-strain stiffness (371.28-817.30Pa). A wider IQR for high-strain stiffness implies a greater diversity in the material's response to substantial deformation [78]. Compared between the median values of high-strain stiffness (2.20E+05Pa) and low-strain stiffness (456.75Pa), as the sample underwent more significant deformation (high strain), strain stiffening comes into play, causing a noticeable increase in stiffness. The strain-stiffening phenomenon was observed in all patients (Figure F2). This finding is in agreement with the studies investigated the healthy donors [65], [69], ovine samples [22], [51] and bovine samples [25]. While the absence of tensile strain-stiffening was shown in all patients (Figure F3) and all blood analogues demonstrated linear behavior in tensile until failure. The build-up of damage inside the blood clot network is responsible for the loss of stiffening caused by tensile strain [36], [69]. In Figure F7H, 80% of the samples started to break between 60%-130% strain, indicating that retrieving these clots with the aspirator becomes increasingly difficult. Future thrombectomy devices will require stiffening methods to withstand high-strain tensile deformation of the thrombus during removal.

As shown in Figure 16, the stress-strain behavior of clots exhibited a significant asymmetry between tension and compression. Compression stiffness was substantially more than tensile stiffness at high strains, while it was lower at low strains. The asymmetry between compression and tensile in clots analogues has previously been shown by comparisons with analogues from ovine [60] and human blood clots [69].

Notably, the hysteresis area and ratio were quantified, offering insights into the material's damping characteristics. This study observed the hysteresis that had also been documented in earlier studies throughout the unloading process [22], [46], [70], [71]. In Figure 15 and Figure F1, the hysteresis areas demonstrated a consistent decrease with each cycle across all samples, especially after the first cycle, there was a significant reduction in hysteresis areas. This phenomenon was also observed in the compression tests conducted on real thrombi [79]. Furthermore, it shows in Figure F1 that 18 out of

23 patients (78%) reached an equilibrium after 14 cycles, which aligns with the steady state described in the study of Good [25].

Additionally, the analogue contraction ratio in this study was determined as the proportion of serum to the weight of the entire solution after sample incubation. As demonstrated by the findings (Figure 18), the analogue contraction ratio had no significant impact on the other properties that were examined. However, there remains a conflict as it is known from previous research that platelet-driven contraction can dramatically influence clot stiffness [80]. Some other studies have concluded that the analogue contraction ratio contributes to the increased stiffness under compression with the experiments controlling the content of platelets and red blood cells in thrombus analogues of healthy volunteers [81] and ovine clots [69]. The potential explanation lies in the divergence of research objectives across various studies. Prior investigations manually regulated the red blood cell content within the samples to examine the correlation among red blood cell content, thrombus analogue contraction ratio, and mechanical compression and tensile properties. In contrast to those studies, this experiment demonstrated an analogue contraction ratio ranging from 0.55 to 0.61, a span that largely aligns with only a single experimental group in Cahalane's study, where the red blood cell content was set between 40% and 60%, resulting in analogue contraction ratio ranging from 0.50 to 0.62. In Cahalane's study, mechanical properties did not exhibit obvious differences or relationships based on this red blood cell content either. Consequently, it is hypothesized that the small variation in red blood cell content among patient samples in our experiment was insufficient to establish a statistically significant relationship between the analogue contraction ratio and mechanical properties.

The three tensile parameters exhibit a monotonically growing relationship and a strong association with one another, indicating that higher ultimate tensile strain coincides with higher ultimate tensile stress (ρ=0.95, p<0.001), along with higher tensile stiffness (ρ=0.83, p<0.001). In practical terms, the lower the strain required to reach the breaking point of the thrombus analogue, the earlier the thrombus analogue breaks, and the lower stress resistibility can be expected, choosing a device to remove this thrombus requires consideration of its more fragile nature. Meanwhile, tensile stiffness (range from 1.42E+03 to 21.38E+03Pa) showed greater diversity compared to healthy donors (range from 3.2E+03 to 9.55E+03Pa) [69].

The ranges of compression high-strain stiffness and tensile stiffness observed in the patient group of this study exhibited a wide range of variability compared to those in the healthy control group, as reported in Cahalane $et\ al.$ [69]. This increased variability may be attributed to alterations in the composition of the patient's blood. Khongkhatithu $et\ al.$ reported that abnormal red blood cell indices can lead to irregular blood flow patterns, posing a risk for ischemic stroke [82]. Moreover, at the time of acute ischemic stroke (AIS) diagnosis, there was a notable increase in hematocrit and red blood cell count [83]. Additionally, AIS patients, in comparison to the healthy donor group, exhibited a higher percentage of mononuclear cells and a lower platelet count [84].

From Figure E3, the sample exhibited a stable fracture propagating with an almost constant force after exhibiting an initial non-linear stiffening, this condition also happened to blood analogues from ovine blood [60]. As shown in Figure 18, fracture toughness demonstrates a notable correlation with high-strain stiffness (ρ=0.63, p=0.025). The current investigation stands as a singular reference concerning this association, lacking previous research for comparison. However, Fereidoonnezhad $et\ al.$ [60] and Liu $et\ al.$ [85] had individually probed the fracture toughness and fracture energy of thrombus analogues. Their investigations revealed a decline in fracture toughness as the amount of red blood cells increased (5% red blood cell content with fracture toughness 0.022 kJ/m2, 20% with 0.017 kJ/m2 and 40% with 0.007 kJ/m2). Specifically, red blood cell-rich clots exhibit susceptibility to fragmentation in contrast to clots characterized by higher fibrin content. In the current study, the relation between fracture toughness and thrombus analogue composition has not been investigated and the relevant histological examination can be conducted on thrombus analogues in the future.

Two relaxation loading protocols were introduced in this study: stress-relaxation at a constant 60% applied compression strain; and stress-relaxation at a constant 125% applied tensile strain. Two relaxation curves indicate that all patients exhibited viscoelasticity (Figure F5 and F6), in agreement with the ovine blood sample observed in the study of Johnson $et\ al.$ [22]. It is worth underscoring that no mechanical parameters were directly derived from these two experiments. However, the material parameters acquired through the fitting of the second-order Prony series, as shown in Table F3, hold utility for subsequent models establishing studies, offering a basis for further viscoelasticity exploration and analysis. In the future, the time constants of stress relaxation tests can be investigated to understand

the more detailed viscoelastic behavior [60].

Multiple simulations are made possible by in silico modeling, which makes it easier to test a large number of possible clinical scenarios with a high degree of reliability. In addition, with the help of computational models, the understanding of the fundamental causes of therapy failures in the clinical context might be improved. In this study, it was observed that the Yeoh model was unable to adequately represent both compression and tensile behaviors simultaneously. The possible reason is that Yeoh model is a typical linear and isotropic model while the compression and tensile curves together exhibited an obvious asymmetry (Figure G1), and there are clear shortcomings in Yeoh model when it comes to modeling the high strain portion of both tests [86]. Fereidoonnezhad $et\ al.$ proposed a new material model to simulate the multi-axial deformation of blood clot occlusions in vessels and it has been demonstrated that this model can accurately predict the volumetric and isochoric properties of blood clots in a variety of compositions [47]. For future work, this cutting-edge hyperelastic model can be combined with the Prony series to capture the hyper-viscoelastic behavior of thrombus analogues. In addition, there are several groups that modeled a framework to simulate the interaction that happened between clots and arteries: a hyperelastic artery, a nonlinear incompressible viscoelastic solid clot, and a CZ (cohesive zone) that models the clot–artery interface [49], [50]. This system can be used for future objectives when more realistic features are needed.

4.1.2. Imaging characteristics

Several basic imaging characteristics were investigated in this study (Table F4 and Table F5). These parameters are delineated in terms of medians and IQR in Section 3.2, undergoing internal correlation analysis (Figure 23) and subsequent external correlation analysis with previously acquired mechanical data (Figure 24).

DT ranges from 1.79 to 82.44mm, showing a great diversity of embolization locations although in terms of IQR (25%-75%) and median, the value from this study (21.9mm, IQR from 8.99-24.69mm) was similar to another patient group (24mm, IQR from 15-33mm) in the study from N. Arrarte Terreros $et\ al.$ [87]. The eligibility for endovascular therapy (EVT) in stroke patients is influenced by various baseline characteristics, with the occlusion location being a critical determinant [62]. According to stroke guidelines, patients who have proximal occlusions (M1, M2, M3 bifurcation) are eligible for EVT [13]. However, the eligibility requirements for individuals who have more distal occlusions (M4 segment)—especially those involving medium vessel occlusions—are presently being looked at [88]. Moreover, evaluating occlusion location is a routine procedure in clinical practice and studies. It proves to be less time-intensive than manually measuring thrombi and does not necessitate using thin-slice images [89]. Consequently, if image parameters associated with the occlusion's location can be established, it may pave the way for prospective surgical decision-making based on this straightforward parameter. Although the previous study revealed significant intercorrelations among thrombus distance to ICA-T (DT), thrombus perviousness, thrombus attenuation, and thrombus length, a few exhibited moderate and high relationships [62], in this study, DT had no significant correlation with not only imaging characteristic but also mechanical properties. This conclusion should be drawn with caution because of the small size of the study group.

Furthermore, in Terreros's sample population, the median and IQR of thrombus length were 18mm (11-29mm) [62], which aligns closely with the values obtained in this study, which were 21.34mm (14.46-29.15mm) (Table 3.5 and Figure F10). However, their dataset exhibited a broader spectrum of thrombus attenuation values (44-57HU) compared to this study (29.27-47.42HU). Their perviousness was closer to 0 HU which was 5HU (-2-13HU) in comparison with 14.31HU (0.49-27.7HU) in this study. While the perviousness range in other experiments typically initiates from 0HU [90], [91], the IQR in Terreros's experiment reveals the presence of some negative values around 0HU [87]. Nevertheless, it is noteworthy that an outlier of -16HU was identified in this experiment. The explanation of this unusual value is an area that requires more research and discussion.

Relatedly, there are three out of thirteen patients were observed with hyperdense artery signs (HAS), which can be quantitatively measured and defined as the artery with a density HU on NCCT greater than 50 [92]. In related research, they studied the correlation between HAS and the composition of thrombus analogues especially the content of red blood cells and found rich red blood cells thrombi and the presence of HAS are frequently linked [93]–[95].

The examination of the median dataset in the current study reveals a noticeable difference in density values between CTA and NCCT. The augmented density values obtained from CTA can be attributed to

the enhanced visualization of blood vessels under the CTA setup, as noted in the work by Terreros $et\ al.$ [87]. This enhancement contributes to predominantly positive numerical values in the representation of Thrombus perviousness. A preceding investigation conducted by Patel $et\ al.$ demonstrated a significant correlation between thrombus perviousness and its composition. However, no correlation was observed between thrombus composition and density on NCCT [91]. The lack of correlation between thrombus perviousness and NCCT density revealed in this study is an extension of previous studies exploring the relationship between thrombus composition, perviousness, and NCCT density.

Thrombus length and perviousness exhibit a robust correlation with density in CTA but not in NCCT. This observation aligns with the findings of a study wherein thrombus length, determined based on the absence of contrast in single-phase CTA [62], in the meantime verified the effectiveness of the registration process. Besides, the strong negative monotonic association exhibited by thrombus length and perviousness (ρ= -0.88, p<0.001) was consistent with many studies [14], [87], [91].

This analysis indicates that some thrombus characteristics exhibit significant but moderate correlations. This observation implies that a single thrombus variable may provide limited information, as there remains a considerable degree of variability in other thrombus characteristics not captured by the analyzed variable. This finding is also consistent with another study [87].

4.1.3. The correlation between Imaging and mechanical results

It can be determined that a higher analogue contraction ratio is strongly correlated with a lower density of middle NCCT. In this context, higher analogue contraction denotes greater thrombus analogue density. Therefore, the mechanical properties of thrombus analogue could not be directly connected to imaging characteristics but they do have some correlation underneath. It can be hypothesized that beyond the thrombus composition, the microstructure also assumes a critical role in shaping the characteristics of thrombi [96], [97].

4.2. Limitation

First, the process of EVT retrieval subjects thrombi to multiaxial loading conditions at various strain rates. In order to streamline the mechanical characterization of blood clot analogues, our study exclusively focused on uniaxial tensile and unconfined compression experiments, excluding shear investigations. Subsequent research should consider the inclusion of experiments tailored to characterize the shear responses of clots, thus providing a more comprehensive assessment of their mechanical behavior.

Secondly, while this study initially encompassed 29 patients, it is essential to note that, due to several mitigating factors, only 9 pairs of imaging and mechanical datasets were ultimately included in the final correlation analysis. Consequently, the sample size at our disposal for analysis is relatively modest. Furthermore, the strict criteria for assessing thrombus imaging characteristics resulted in a reduction in this sample size. Specifically, two cases were afflicted by suboptimal image quality, and an additional four cases exhibited image slices with thicknesses exceeding five millimeters, contributing to a notable exclusion rate. This, in turn, introduced the potential for selection bias in this study.

Last but not least, occlusion patterns were visually assessed on single-phase CTA images, introducing a degree of potential inaccuracy and variability, particularly in discerning the distal boundary of the thrombus. Although this aspect was aided by the expertise of skilled surgeons, it is acknowledged that this phase is inherently challenging. Besides, the presence of inadequate distal contrast filling could have contributed to potential misclassification.

5

Conclusion

To the best of the author's knowledge, this is the first time to study the correlation between clinical CT imaging characteristics and mechanical properties of in vitro thrombi in acute ischemic stroke. In conclusion, the mechanical tests on patient-specific blood analogues provided valuable insights into various parameters. The unconfined cyclic compression test revealed distinct high- and low-strain stiffness values, suggesting diverse material responses to substantial deformation. The strain-stiffening phenomenon, observed in all patients, aligns with previous studies on healthy donors and animal samples. The asymmetry between compression and tensile stiffness, along with hysteresis area reduction, indicates energy dissipation during stress-strain behavior. The contraction ratio had no significant impact on other properties, contradicting some previous findings. The positive correlation between tensile parameters implies that thrombus analogues breaking earlier may have lower stress resistibility. It is worth highlighting that the analogue contraction ratio of the thrombus analogue displayed a strong negative monotonic correlation with the density of the middle NCCT for actual thrombi. It is conceivable that in addition to the composition of thrombi, the microstructure plays a crucial influence in determining their properties.

This study enhances understanding of thrombus behavior, contributing insights for the correlation between thrombus analogues and real thrombi. The observed asymmetry, strain-stiffening, and hysteresis provide crucial information for device development. The lack of correlation between contraction ratio and other properties challenges existing notions, urging further exploration. Future models combining hyperelasticity and viscoelasticity may better capture thrombus analogues' behavior.

References

[1] R. V. Krishnamurthi, T. Ikeda, and V. L. Feigin, "Global, regional and country-specific burden of ischaemic stroke, intracerebral haemorrhage and subarachnoid haemorrhage: A systematic analysis of the global burden of disease study 2017," *Neuroepidemiology*, vol. 54, no. 2, pp. 171–179, 2020.

[2] S. R. Martini and T. A. Kent, "Chapter 58 - ischemic stroke," in *Cardiology Secrets (Fifth Edition)*, G. N. Levine, Ed., Fifth Edition, Elsevier, 2018, pp. 493–504, ISBN: 978-0-323-47870-0. DOI: https://doi.org/10.1016/B978-0-323-47870-0.00058-1. [Online]. Available: https://www.sciencedirect.com/science/article/pii/B9780323478700000581.

[3] H. B. Van der Worp and J. van Gijn, "Acute ischemic stroke," *New England Journal of Medicine*, vol. 357, no. 6, pp. 572–579, 2007.

[4] G. Badwaik and P. Badwaik, "Influence of psychological disorders on the functional outcomes in the survivors of ischemic stroke," *Journal of Stroke and Cerebrovascular Diseases*, vol. 30, no. 2, p. 105 486, 2021.

[5] S. R. Zhang, T. G. Phan, and C. G. Sobey, "Targeting the immune system for ischemic stroke," *Trends in pharmacological sciences*, vol. 42, no. 2, pp. 96–105, 2021.

[6] A. E. Hillis, "Acute ischemic stroke," in *Current Therapy in Neurologic Disease (Seventh Edition)*, R. T. Johnson, J. W. Griffin, and J. C. McArthur, Eds., Seventh Edition, Philadelphia: Mosby, 2006, pp. 213–218, ISBN: 978-0-323-03432-6. DOI: https://doi.org/10.1016/B978-0-323-03432-6.50052-0. [Online]. Available: https://www.sciencedirect.com/science/article/pii/B9780323034326500520.

[7] B. I. National Heart Lung, *Stroke*, https://www.nhlbi.nih.gov/health/stroke.

[8] N. Arrarte Terreros, "Imaging and modelling in acute ischemic stroke: Quantifying thrombus and residual blood flow characteristics," English, Ph.D. dissertation, University of Amsterdam, 2023, ISBN: 9789464691603.

[9] K. Kirchhof, T. Welzel, C. Mecke, S. Zoubaa, and K. Sartor, "Differentiation of white, mixed, and red thrombi: Value of ct in estimation of the prognosis of thrombolysis—phantom study," *Radiology*, vol. 228, no. 1, pp. 126–130, 2003.

[10] D. S. Liebeskind, N. Sanossian, W. H. Yong, *et al.*, "Ct and mri early vessel signs reflect clot composition in acute stroke," *other*, vol. 42, no. 5, 2011.

[11] F. Herpich and F. Rincon, "Management of acute ischemic stroke," *Critical care medicine*, vol. 48, no. 11, p. 1654, 2020.

[12] J.-a. Giezen, "The association between in vitro human thrombi composition, mechanics, and computed tomography imaging characteristics," 2021.

[13] W. J. Powers, A. A. Rabinstein, T. Ackerson, *et al.*, "Guidelines for the early management of patients with acute ischemic stroke: 2019 update to the 2018 guidelines for the early management of acute ischemic stroke: A guideline for healthcare professionals from the american heart association/american stroke association," *Stroke*, 2019.

[14] N. A. Terreros, S. Renon, F. Zucchelli, *et al.*, "Microcatheter tracking in thrombectomy procedures: A finite-element simulation study," *Computer Methods and Programs in Biomedicine*, p. 107 515, 2023.

[15] O. A. Berkhemer, P. S. Fransen, D. Beumer, *et al.*, "A randomized trial of intraarterial treatment for acute ischemic stroke," *n Engl J Med*, vol. 372, pp. 11–20, 2015.

[16] J. M. Ospel, A. van der Lugt, M. Gounis, M. Goyal, and C. B. Majoie, "A clinical perspective on endovascular stroke treatment biomechanics," *Journal of Biomechanics*, vol. 127, p. 110 694, 2021.

[17] F. SAAB, J. H. PARK, V. VADLAMUDI, M. FAKHIR ELMASRI, and M. EZELL ASKEW JR, "Indigo® system for thromboembolic disease,"

[18] R. A. McTaggart, E. L. Tung, S. Yaghi, *et al.*, "Continuous aspiration prior to intracranial vascular embolectomy (captive): A technique which improves outcomes," *Journal of neurointerventional surgery*, vol. 9, no. 12, pp. 1154–1159, 2017.

[19] K. Walter, "What Is Acute Ischemic Stroke?" *JAMA*, vol. 327, no. 9, pp. 885–885, Mar. 2022, ISSN: 0098-7484. DOI: 10.1001/jama.2022.1420. eprint: https://jamanetwork.com/journals/jama/articlepdf/2789540/jama_walter_2022_pg_220003_1645750098.81667.pdf. [Online]. Available: https://doi.org/10.1001/jama.2022.1420.

[20] A. A. Ashrani and J. A. Heit, "Incidence and cost burden of post-thrombotic syndrome," *Journal of thrombosis and thrombolysis*, vol. 28, no. 4, pp. 465–476, 2009.

[21] G. W. Albers, M. P. Marks, S. Kemp, *et al.*, "Thrombectomy for stroke at 6 to 16 hours with selection by perfusion imaging," *New England Journal of Medicine*, vol. 378, no. 8, pp. 708–718, 2018.

[22] S. Johnson, R. McCarthy, M. Gilvarry, P. E. McHugh, and J. P. McGarry, "Investigating the mechanical behavior of clot analogues through experimental and computational analysis," *Annals of Biomedical Engineering*, vol. 49, pp. 420–431, 2021.

[23] S. Duffy, M. Farrell, K. McArdle, *et al.*, "Novel methodology to replicate clot analogs with diverse composition in acute ischemic stroke," *Journal of neurointerventional surgery*, vol. 9, no. 5, pp. 486–491, 2017.

[24] R. Cahalane, N. Boodt, A. C. Akyildiz, *et al.*, "A review on the association of thrombus composition with mechanical and radiological imaging characteristics in acute ischemic stroke," *Journal of Biomechanics*, vol. 129, p. 110 816, 2021, ISSN: 0021-9290. DOI: https://doi.org/10.1016/j.jbiomech.2021.110816. [Online]. Available: https://www.sciencedirect.com/science/article/pii/S0021929021005765.

[25] B. C. Good, "The influence of blood composition and loading frequency on the behavior of embolus analogs," *Journal of the Mechanical Behavior of Biomedical Materials*, vol. 140, p. 105 738, 2023.

[26] S. F. De Meyer, T. Andersson, B. Baxter, *et al.*, "Analyses of thrombi in acute ischemic stroke: A consensus statement on current knowledge and future directions," *International journal of stroke*, vol. 12, no. 6, pp. 606–614, 2017.

[27] J. Chueh, A. Wakhloo, G. Hendricks, C. Silva, J. Weaver, and M. Gounis, "Mechanical characterization of thromboemboli in acute ischemic stroke and laboratory embolus analogs," *American Journal of Neuroradiology*, vol. 32, no. 7, pp. 1237–1244, 2011.

[28] J. H. Ashton, J. P. V. Geest, B. R. Simon, and D. G. Haskett, "Compressive mechanical properties of the intraluminal thrombus in abdominal aortic aneurysms and fibrin-based thrombus mimics," *Journal of biomechanics*, vol. 42, no. 3, pp. 197–201, 2009.

[29] N. Krasokha, W. Theisen, S. Reese, *et al.*, "Mechanical properties of blood clots–a new test method," *Materialwissenschaft und Werkstofftechnik*, vol. 41, no. 12, pp. 1019–1024, 2010.

[30] Z. Teng, J. Feng, Y. Zhang, *et al.*, "Layer-and direction-specific material properties, extreme extensibility and ultimate material strength of human abdominal aorta and aneurysm: A uniaxial extension study," *Annals of biomedical engineering*, vol. 43, pp. 2745–2759, 2015.

[31] J. P. V. Geest, M. S. Sacks, and D. A. Vorp, "A planar biaxial constitutive relation for the luminal layer of intra-luminal thrombus in abdominal aortic aneurysms," *Journal of biomechanics*, vol. 39, no. 13, pp. 2347–2354, 2006.

[32] E. A. van Dam, S. D. Dams, G. W. Peters, *et al.*, "Determination of linear viscoelastic behavior of abdominal aortic aneurysm thrombus," *Biorheology*, vol. 43, no. 6, pp. 695–707, 2006.

[33] C. Schmitt, A. H. Henni, and G. Cloutier, "Characterization of blood clot viscoelasticity by dynamic ultrasound elastography and modeling of the rheological behavior," *Journal of biomechanics*, vol. 44, no. 4, pp. 622–629, 2011.

[34] E. A. van Dam, S. D. Dams, G. W. Peters, *et al.*, "Non-linear viscoelastic behavior of abdominal aortic aneurysm thrombus," *Biomechanics and modeling in mechanobiology*, vol. 7, pp. 127–137, 2008.

[35] T. H. van Kempen, G. W. Peters, and F. N. van de Vosse, "A constitutive model for the time-dependent, nonlinear stress response of fibrin networks," *Biomechanics and modeling in mechanobiology*, vol. 14, pp. 995–1006, 2015.

[36] M. K. Rausch, G. P. Sugerman, S. Kakaletsis, and B. Dortdivanlioglu, "Hyper-viscoelastic damage modeling of whole blood clot under large deformation," *Biomechanics and Modeling in Mechanobiology*, vol. 20, no. 5, pp. 1645–1657, 2021.

[37] A. E. Brown, R. I. Litvinov, D. E. Discher, P. K. Purohit, and J. W. Weisel, "Multiscale mechanics of fibrin polymer: Gel stretching with protein unfolding and loss of water," *science*, vol. 325, no. 5941, pp. 741–744, 2009.

[38] E. Kim, O. V. Kim, K. R. Machlus, *et al.*, "Correlation between fibrin network structure and mechanical properties: An experimental and computational analysis," *Soft Matter*, vol. 7, no. 10, pp. 4983–4992, 2011.

[39] A. H. Henni, C. Schmitt, and G. Cloutier, "Three-dimensional transient and harmonic shear-wave scattering by a soft cylinder for dynamic vascular elastography," *The Journal of the Acoustical Society of America*, vol. 124, no. 4, pp. 2394–2405, 2008.

[40] A. H. Henni, C. Schmitt, and G. Cloutier, "Shear wave induced resonance elastography of soft heterogeneous media," *Journal of Biomechanics*, vol. 43, no. 8, pp. 1488–1493, 2010.

[41] M. Bhatt, E. Montagnon, F. Destrempes, B. Chayer, S. Kazemirad, and G. Cloutier, "Acoustic radiation force induced resonance elastography of coagulating blood: Theoretical viscoelasticity modeling and ex vivo experimentation," *Physics in Medicine & Biology*, vol. 63, no. 6, p. 065 018, 2018.

[42] S. Johnson, S. Duffy, G. Gunning, M. Gilvarry, J. McGarry, and P. McHugh, "Review of mechanical testing and modelling of thrombus material for vascular implant and device design," *Annals of biomedical engineering*, vol. 45, pp. 2494–2508, 2017.

[43] T. H. van Kempen, W. P. Donders, F. N. van de Vosse, and G. W. Peters, "A constitutive model for developing blood clots with various compositions and their nonlinear viscoelastic behavior," *Biomechanics and modeling in mechanobiology*, vol. 15, pp. 279–291, 2016.

[44] D. He, D. A. Kim, D. N. Ku, and Y. Hu, "Viscoporoelasticity of coagulation blood clots," *Extreme Mechanics Letters*, vol. 56, p. 101 859, 2022.

[45] P. Williams, K. Hawkins, C. Wright, *et al.*, "Rheometrical and computational studies of blood viscoelasticity during coagulation," *Clinical hemorheology and microcirculation*, vol. 35, no. 1-2, pp. 123–127, 2006.

[46] K. Tashiro, Y. Shobayashi, I. Ota, and A. Hotta, "Finite element analysis of blood clots based on the nonlinear visco-hyperelastic model," *Biophysical Journal*, vol. 120, no. 20, pp. 4547–4556, 2021.

[47] B. Fereidoonnezhad, K. M. Moerman, S. Johnson, R. McCarthy, and P. J. McGarry, "A new compressible hyperelastic model for the multi-axial deformation of blood clot occlusions in vessels," *Biomechanics and Modeling in Mechanobiology*, vol. 20, pp. 1317–1335, 2021.

[48] B. C. Good, "The influence of blood composition and loading frequency on the behavior of embolus analogs," *Journal of the Mechanical Behavior of Biomedical Materials*, vol. 140, p. 105 738, 2023, ISSN: 1751-6161. DOI: https://doi.org/10.1016/j.jmbbm.2023.105738. [Online]. Available: https://www.sciencedirect.com/science/article/pii/S1751616123000917.

[49] O. Oyekole, S. Simon, K. B. Manning, and F. Costanzo, "Modeling acute ischemic stroke recanalization through cyclic aspiration," *Journal of biomechanics*, vol. 128, p. 110 721, 2021.

[50] P. Patki, S. Simon, K. B. Manning, and F. Costanzo, "Computational analysis of effects of clot length on acute ischemic stroke recanalization under different cyclic aspiration loading conditions," *International Journal for Numerical Methods in Biomedical Engineering*, e3667, 2022.

[51] S. Johnson, J. Chueh, M. J. Gounis, *et al.*, "Mechanical behavior of in vitro blood clots and the implications for acute ischemic stroke treatment," *Journal of neurointerventional surgery*, vol. 12, no. 9, pp. 853–857, 2020.

[52] S. K. Panda and M. L. Buist, "A finite nonlinear hyper-viscoelastic model for soft biological tissues," *Journal of biomechanics*, vol. 69, pp. 121–128, 2018.

[53] S. Staessens and S. F. De Meyer, "Thrombus heterogeneity in ischemic stroke," *Platelets*, vol. 32, no. 3, pp. 331–339, 2021.

[54] B. G. Dutra, M. L. Tolhuisen, H. C. Alves, *et al.*, "Thrombus imaging characteristics and outcomes in acute ischemic stroke patients undergoing endovascular treatment," *Stroke*, vol. 50, no. 8, pp. 2057–2064, 2019.

[55] P. Snouckaert van Schauburg, "Mechanical and histological characterization of thrombi retrieved during thrombectomy for acute ischaemic stroke," 2019.

[56] N. Boodt, P. R. Snouckaert van Schauburg, H. M. Hund, *et al.*, "Mechanical characterization of thrombi retrieved with endovascular thrombectomy in patients with acute ischemic stroke," *Stroke*, vol. 52, no. 8, pp. 2510–2517, 2021.

[57] H. Guo, M. Ji, Y. Zhang, M. Zhang, *et al.*, "Study of mechanical property of rock under uniaxial cyclic loading and unloading," *Advances in Civil Engineering*, vol. 2018, 2018.

[58] K. J. Anusavice, C. Shen, and H. R. Rawls, *Phillips' science of dental materials*. Elsevier Health Sciences, 2012.

[59] S. Goh, M. Charalambides, and J. Williams, "Determination of the constitutive constants of non-linear viscoelastic materials," *Mechanics of Time-Dependent Materials*, vol. 8, pp. 255–268, 2004.

[60] B. Fereidoonnezhad, A. Dwivedi, S. Johnson, R. McCarthy, and P. McGarry, "Blood clot fracture properties are dependent on red blood cell and fibrin content," *Acta Biomaterialia*, vol. 127, pp. 213–228, 2021.

[61] S. Klein, M. Staring, K. Murphy, M. A. Viergever, and J. P. Pluim, "Elastix: A toolbox for intensity-based medical image registration," *IEEE transactions on medical imaging*, vol. 29, no. 1, pp. 196–205, 2009.

[62] N. A. Terreros, A. A. Bruggeman, M. Kappelhof, *et al.*, "Thrombus imaging characteristics within acute ischemic stroke: Similarities and interdependence," *Journal of neurointerventional surgery*, vol. 15, no. e1, e60–e68, 2023.

[63] N. Boodt, K. C. Compagne, B. G. Dutra, *et al.*, "Stroke etiology and thrombus computed tomography characteristics in patients with acute ischemic stroke: A mr clean registry substudy," *Stroke*, vol. 51, no. 6, pp. 1727–1735, 2020.

[64] U. Jensen-Kondering, C. Riedel, and O. Jansen, "Hyperdense artery sign on computed tomography in acute ischemic stroke," *World journal of radiology*, vol. 2, no. 9, p. 354, 2010.

[65] R. Cahalane, N. Boodt, A. C. Akyildiz, *et al.*, "A review on the association of thrombus composition with mechanical and radiological imaging characteristics in acute ischemic stroke," *Journal of Biomechanics*, vol. 129, p. 110 816, 2021.

[66] M. Berndt, B. Friedrich, C. Maegerlein, *et al.*, "Thrombus permeability in admission computed tomographic imaging indicates stroke pathogenesis based on thrombus histology," *Stroke*, vol. 49, no. 11, pp. 2674–2682, 2018.

[67] J. Borggrefe, J. Kottlors, M. Mirza, *et al.*, "Differentiation of clot composition using conventional and dual-energy computed tomography," *Clinical neuroradiology*, vol. 28, pp. 515–522, 2018.

[68] I. The MathWorks, *Symbolic math toolbox*, Natick, Massachusetts, United State, 2019. [Online]. Available: `https://www.mathworks.com/help/symbolic/`.

[69] R. M. Cahalane, J. J. de Vries, M. P. de Maat, *et al.*, "Tensile and compressive mechanical behaviour of human blood clot analogues," *Annals of Biomedical Engineering*, pp. 1–10, 2023.

[70] W. Liu, C. Carlisle, E. Sparks, and M. Guthold, "The mechanical properties of single fibrin fibers," *Journal of thrombosis and haemostasis*, vol. 8, no. 5, pp. 1030–1036, 2010.

[71] G. P. Sugerman, S. H. Parekh, and M. K. Rausch, “Nonlinear, dissipative phenomena in whole blood clot mechanics,” *Soft Matter*, vol. 16, no. 43, pp. 9908–9916, 2020.

[72] T. C. Gasser, G. Görgülü, M. Folkesson, and J. Swedenborg, “Failure properties of intraluminal thrombus in abdominal aortic aneurysm under static and pulsating mechanical loads,” *Journal of vascular surgery*, vol. 48, no. 1, pp. 179–188, 2008.

[73] J. W. Weisel, “The mechanical properties of fibrin for basic scientists and clinicians,” *Biophysical chemistry*, vol. 112, no. 2-3, pp. 267–276, 2004.

[74] G. Luraghi, J. F. Rodriguez Matas, G. Dubini, *et al.*, “Applicability assessment of a stent-retriever thrombectomy finite-element model,” *Interface Focus*, vol. 11, no. 1, p. 20 190 123, 2021.

[75] K. H. Yang, “Chapter 5 - material laws and properties,” in *Basic Finite Element Method as Applied to Injury Biomechanics*, K.-H. Yang, Ed., Academic Press, 2018, pp. 231–256, ISBN: 978-0-12-809831-8. DOI: https://doi.org/10.1016/B978-0-12-809831-8.00005-2. [Online]. Available: https://www.sciencedirect.com/science/article/pii/B9780128098318000052.

[76] C. Pearson’s, “Comparison of values of pearson’s and spearman’s correlation coefficients,” *Comparison Of Values Of Pearson’s And Spearman’s Correlation Coefficients*, 2011.

[77] O. Wodo and B. Ganapathysubramanian, “Computationally efficient solution to the cahn–hilliard equation: Adaptive implicit time schemes, mesh sensitivity analysis and the 3d isoperimetric problem,” *Journal of Computational Physics*, vol. 230, no. 15, pp. 6037–6060, 2011.

[78] C. H. Parvini, A. X. Cartagena-Rivera, and S. D. Solares, “Viscoelastic parameterization of human skin cells characterize material behavior at multiple timescales,” *Communications Biology*, vol. 5, no. 1, p. 17, 2022.

[79] I. N. Chernysh, R. Spiewak, C. L. Cambor, P. K. Purohit, and J. W. Weisel, “Structure, mechanical properties, and modeling of cyclically compressed pulmonary emboli,” *Journal of the mechanical behavior of biomedical materials*, vol. 105, p. 103 699, 2020.

[80] S. J. Pathare, W. Eng, S.-J. J. Lee, and A. K. Ramasubramanian, “Fibrin prestress due to platelet aggregation and contraction increases clot stiffness,” *Biophysical Reports*, vol. 1, no. 2, 2021.

[81] M. H. Choi, G. H. Park, J. S. Lee, *et al.*, “Erythrocyte fraction within retrieved thrombi contributes to thrombolytic response in acute ischemic stroke,” *Stroke*, vol. 49, no. 3, pp. 652–659, 2018.

[82] C. Khongkhatithum, P. Kadegasem, W. Sasanakul, L. Thampratankul, A. Chuansumrit, and N. Sirachainan, “Abnormal red blood cell indices increase the risk of arterial ischemic stroke in children,” *Journal of Clinical Neuroscience*, vol. 62, pp. 117–120, 2019.

[83] A. R. Nayak, R. S. Kashyap, D. Kabra, *et al.*, “Evaluation of routinely performed hematological and biochemical parameters for the prognosis of acute ischemic stroke patients,” *Neurological Sciences*, vol. 32, pp. 855–860, 2011.

[84] D. Wang, F. Zhang, Y. Zhao, *et al.*, “Association of polymorphism in icam-1 (k469e) and cytology parameters in patients’ initial blood test with acute ischemic stroke,” *Genetics and Molecular Research*, vol. 14, no. 4, pp. 15 520–15 529, 2015.

[85] S. Liu, G. Bao, Z. Ma, C. J. Kastrup, and J. Li, “Fracture mechanics of blood clots: Measurements of toughness and critical length scales,” *Extreme Mechanics Letters*, vol. 48, p. 101 444, 2021.

[86] T. W. Hohenberger, R. J. Windslow, N. M. Pugno, and J. J. Busfield, “A constitutive model for both low and high strain nonlinearities in highly filled elastomers and implementation with user-defined material subroutines in abaqus,” *Rubber Chemistry and Technology*, vol. 92, no. 4, pp. 653–686, 2019.

[87] N. A. Terreros, A. A. Bruggeman, I. S. Swijnenburg, *et al.*, “Early recanalization in large-vessel occlusion stroke patients transferred for endovascular treatment,” *Journal of NeuroInterventional Surgery*, vol. 14, no. 5, pp. 480–484, 2022.

[88] M. Shapiro, E. Raz, E. Nossek, B. Chancellor, K. Ishida, and P. K. Nelson, “Neuroanatomy of the middle cerebral artery: Implications for thrombectomy,” *Journal of neurointerventional surgery*, vol. 12, no. 8, pp. 768–773, 2020.

[89] A. Ciccone, L. Valvassori, M. Nichelatti, *et al.*, “Endovascular treatment for acute ischemic stroke,” *New England Journal of Medicine*, vol. 368, no. 10, pp. 904–913, 2013.

[90] J. C. Benson, S. T. Fitzgerald, R. Kadirvel, *et al.*, “Clot permeability and histopathology: Is a clot’s perviousness on ct imaging correlated with its histologic composition?” *Journal of neurointerventional surgery*, vol. 12, no. 1, pp. 38–42, 2020.

[91] T. Patel, S. Fricano, M. Waqas, *et al.*, “Increased perviousness on ct for acute ischemic stroke is associated with fibrin/platelet-rich clots,” *American Journal of Neuroradiology*, vol. 42, no. 1, pp. 57–64, 2021.

[92] S. T. Fitzgerald, S. Wang, D. Dai, *et al.*, “Platelet-rich clots as identified by martius scarlet blue staining are isodense on ncct,” *Journal of neurointerventional surgery*, vol. 11, no. 11, pp. 1145–1149, 2019.

[93] D. S. Liebeskind, N. Sanossian, W. H. Yong, *et al.*, “Ct and mri early vessel signs reflect clot composition in acute stroke,” *Stroke*, vol. 42, no. 5, pp. 1237–1243, 2011.

[94] G. Ye, R. Cao, J. Lu, *et al.*, “Histological composition behind ct-based thrombus density and perviousness in acute ischemic stroke,” *Clinical Neurology and Neurosurgery*, vol. 207, p. 106 804, 2021.

[95] S. Ahn, I. Choo, R. Hong, *et al.*, “Hyperdense arterial sign reflects the proportion of red blood cells in the thromboemboli of acute stroke patients,” *Cerebrovasc Dis*, vol. 33, p. 236, 2012.

[96] R. F. Landel and L. E. Nielsen, *Mechanical properties of polymers and composites*. CRC press, 1993.

[97] M.-N. Abdallah, T. Lou, J.-M. Retrouvey, and S. Suri, “20 - biomaterials used in orthodontics: Brackets, archwires, and clear aligners,” in *Advanced Dental Biomaterials*, Z. Khurshid, S. Najeeb, M. S. Zafar, and F. Sefat, Eds., Woodhead Publishing, 2019, pp. 541–579, ISBN: 978-0-08-102476-8. DOI: https://doi.org/10.1016/B978-0-08-102476-8.00020-7. [Online]. Available: https://www.sciencedirect.com/science/article/pii/B9780081024768000207.

[98] X.-K. Zhu and J. A. Joyce, “Review of fracture toughness (g, k, j, ctod, ctoa) testing and standardization,” *Engineering fracture mechanics*, vol. 85, pp. 1–46, 2012.

[99] R. Long and C.-Y. Hui, “Fracture toughness of hydrogels: Measurement and interpretation,” *Soft Matter*, vol. 12, no. 39, pp. 8069–8086, 2016.

A

Appendix: Inclusion flowchart

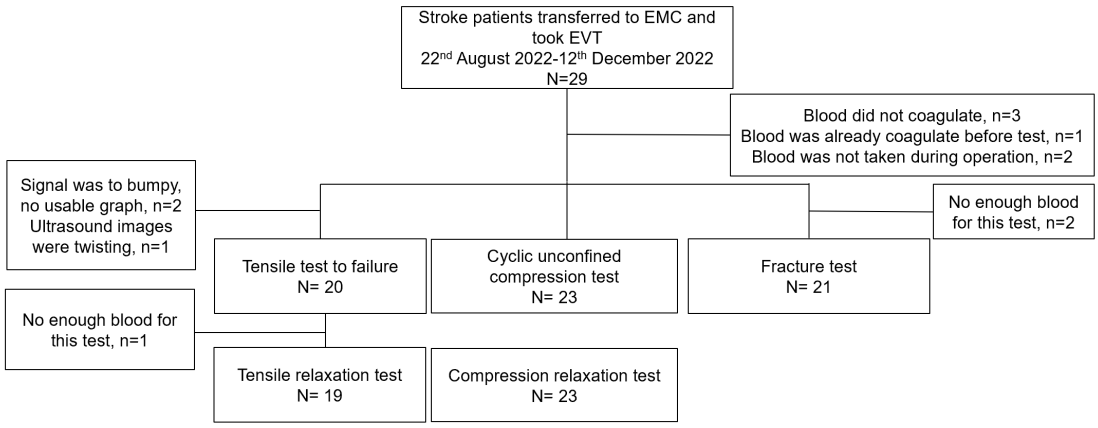

Figure A1: Mechanical tests inclusion flowchart. EVT, endovascular thrombectomy.

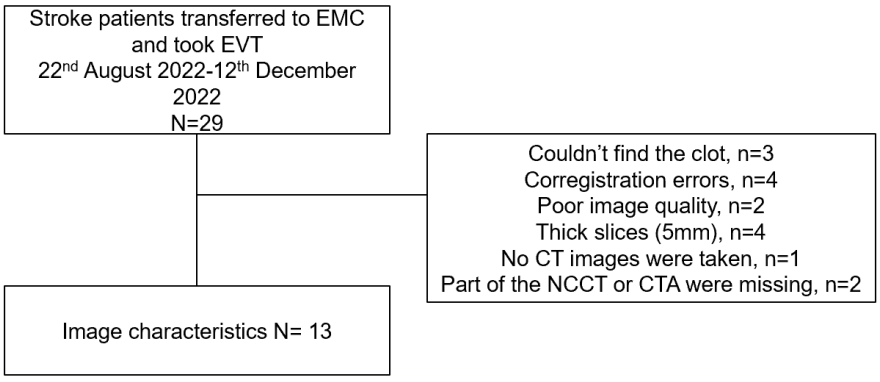

Figure A2: Thrombus imaging characteristics inclusion flowchart.

B

Appendix: Protocol of preparation of thrombus analogues

B.1. Samples making

As soon as the researcher was informed that the patients would arrive, the instruments, the chemicals and the containers were well prepared, as shown in Figure B1. Samples were made following the steps below:

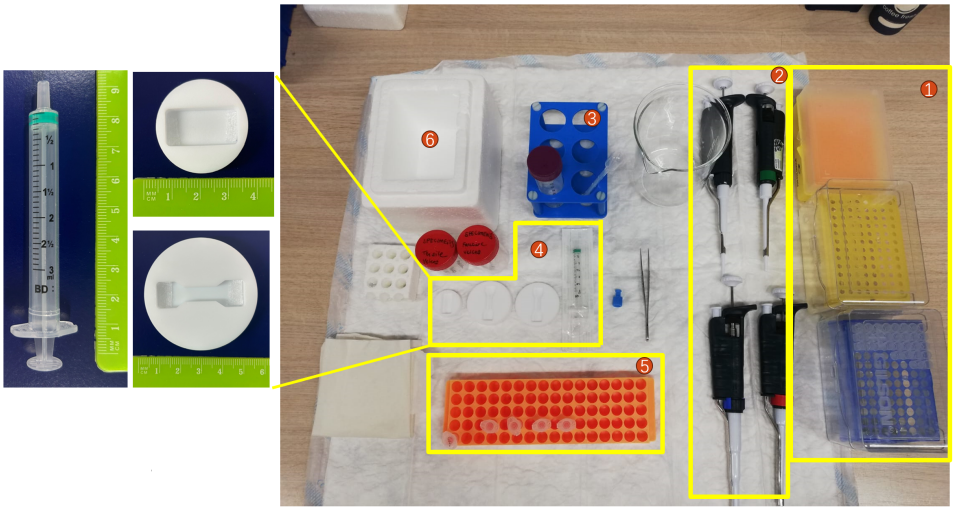

Figure B1: Consumables that need to be prepared before making samples: ❶ are pipette tips set; ❷ are pipette sets with different maximum capacities; ❸ is mineral oil; ❹ are molds for mechanical tests: two with dog bone shape, one 3 ml syringe and one with rectangle shape; ❺ are calcium chloride and vials for mixing blood with chemical; ❻ is the ice box used to store thrombin temporarily.

Before starting the experiment, it is crucial to ensure thorough mixing of the contents. Start by inverting the entire blood tube four times. To each sample tube (compression, tension x 2, fracture), add 970µL of whole blood volumes.

Generally, prepare three pipettes along with their respective tips: 1000µL, 20µL, and 10µL. Take care when adding calcium chloride to sample vials, ensuring that it is added below the liquid level. Pre-mix the solution and ensure that no residual liquid remains in the pipette tip before discarding.

Next, thrombin was introduced below the liquid level, pushing it all the way down to the second stop. Immediately perform a single mixing step using the 1000µL pipette and subsequently transfer the mixture to syringes or molds.

For compression experiments, eliminate any bubbles from the compression syringe by gently flicking and dispensing against a tissue.

In the case of tensile or fracture experiments, mix once using the 1000µL pipette, then carefully reverse the pipette to 1200µL to extract the entire volume, taking care not to introduce blood into the pipette. Dispense blood along the tensile mold in a linear fashion, slightly tilting to ensure even coverage of the entire mold by the blood solution. After that, allow a 10-second waiting period to prevent the formation of oil pockets. Using a plastic dropper, gently add a layer of mineral oil until the top of the sample is fully covered. Be cautious not to introduce bubbles during the pipetting process; avoid stopping pipetting once all the blood has been dispensed, and perform a slight reverse pipetting motion.

If bubbles are accidentally introduced, gently touch them with a pipette tip after adding the oil. If they detach from the sample, make a note indicating the presence of bubbles on the information sheet.

Third, before starting the incubation process, capture photographs of the samples, as shown in Figure 8(a).

After completing the meticulous preparation steps detailed earlier, proceed to the incubation phase of the experiment. Begin by placing the molds into plastic dishes containing some HEPEs solution to facilitate the next steps. Carry the prepared syringes and dishes to the dedicated laboratory, where the incubator is stored. It is important to maintain sterile conditions; therefore, the researchers were asked to wear a pair of gloves and lightly mist them with ethanol. Subsequently, place the molds and syringes inside the designated incubator. It is worth noting that the molds should lie flat within the incubator, while the syringes should stand vertically to ensure proper orientation.

Upon initiating this phase, start a timer that lasts one hour. Throughout the incubation period, carefully record the elapsed time and carefully fill in the relevant details on the sample information sheet to maintain accurate records. The samples prepared for the final tests can be seen in Figure 8(b).

B.2. Samples preparation

After an hour of incubation, the samples in the three molds have become solid, and the next step is to pre-process the samples for the final experiment. First, for the samples of the compression test, it is necessary to first determine the weight of the fully loaded syringe. Subsequently, the clots were carefully removed from each syringe and the individual weights of these clots were determined individually. Re-zero the scale using the designated weighing pan to ensure accurate measurements.

Afterward, cut blood clots into manageable 2 x 2mm pieces with meticulous precision using the specialized 2mm cutting tool and microtome blade. The pixel-to-length ratio was measured using a ruler, and the sample's surface area was calculated using the freehand selection tool.

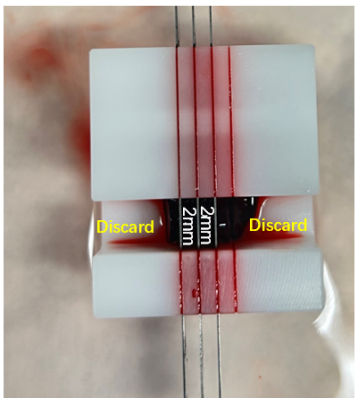

(a) Cut into 2 x 2mm thickness pieces

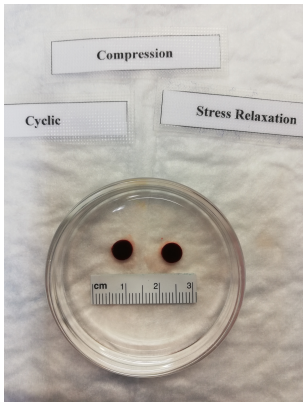

(b) The photo of the sample with the ruler for cross-sectional areas measurement

Figure B2: Pre-process for compression samples

It is critical to maintain a consistent approach, always discarding the upper and lower parts of the clot. Instead, choose to select two different sections from the central region of the clot for subsequent

analysis and experiments, as shown in Figure B2(a). Lastly, take a photo of the sample with the ruler for cross-sectional areas measurement, as shown in Figure B2(b). This comprehensive process ensures the accuracy and reliability of the sample preparation and lays a solid foundation for subsequent stages of experiments.

For tensile and fracture samples, upon completion of the incubation period, capture a photograph of the sample to document its condition and any observable changes that may have occurred. Subsequently, proceed to carefully extract the clot from the mold, taking care to gently release the Velcro fastenings from both ends. It is crucial to ensure that the Velcro attachments are fully disengaged before attempting to remove the entire sample.

Exercise caution and handle the sample with utmost care to prevent any unintended damage. Subsequent to detaching the sample, initiate the rinsing process by placing it within a dish containing HEPEs buffer. This step serves to effectively eliminate any residual oil present on the sample's surface, contributing to the precision and accuracy of the subsequent analyses and assessments.

C

Appendix: Perform the tests on the compression tester

C.1. Set up

To begin with, make sure the water bath is fully prepared by filling it with HEPES buffer, then plugging the bath into the heating unit and turning it on to preheat the liquid. The test should wait until the water bath is fully heated, at least five minutes.

In terms of setup, use the designated laptop and make sure it stays connected to the charger at all times. Plug in the compression tester and listen for the confirmation ”click”. Connect the two USB cables to the corresponding laptop USB ports, then log in using the password provided to start the laptop, and complete the setup, as shown in Figure C1.

Figure C1: Set up for compression tester

C.2. Cyclic unconfined compression test

For effective file management, navigate to the specified locations: Desktop > SPECIMENS and MR-CLOT studies. Begin by opening the MEX file labeled ”SPECIMENS 80 % compression – 2mm sample – 20 loops” and meticulously review the settings within. Confirm proper settings before initiating data writing (PC > Product); upon completion of the writing process, acknowledge with an ’OK’ selection.

Subsequently, close the MEX file and proceed to open the LabVIEW file named ”unconfined compression program.” Initiate the process by clicking the ’Run’ button, denoted by the white arrow positioned in the top-left corner of the interface. As the load cell readings become visible, perform a tare by holding for a complete second, ensuring a deliberate action rather than a swift click.

To enhance precision, remove any bubbles from the water bath and carefully place the sample on the designated water bath stage. Trigger a 5-minute timer and proceed by clicking ’Set to starting height’; this action will cause the plate to lower into the water bath and establish contact with the sample.

Essential checks encompass verifying the correct load cell pattern and ensuring that the plate aligns with the top of the sample. Any discrepancies in these aspects necessitate an evaluation of the water bath's positioning, with the zero position being of particular significance.

Prepare an empty text file with the accurate file name and utilize the file path button to designate the desired save location. Once the load cell signal stabilizes, devoid of drift (indicated by a flat line), initiate the test and recording process by selecting 'start test and recording.' Should the signal exhibit irregularities, consider halting the program and restarting it. Verify that the load cell wire remains unobstructed and avoid contact with any objects. Adjust the position of the entire stand if necessary to achieve a steady, flat line.

Document relevant details on the information sheet, including the start time, and patiently oversee the flawless execution of 20 cycles, which should conclude within approximately 6 to 7 minutes. Upon completion, the plate will ascend to a high position. Once the plate surpasses the water level, promptly press 'stop recording.' Confirm the test's success by verifying data storage in the designated file, characterized by a non-zero file size.

Maintain the LabVIEW file in an open state to ensure a smooth transition to the next steps. Careful follow-up of these steps will guarantee the correct performance and thorough documentation of the test.

C.3. Compressive Stress Relaxation Testing

The procedure begins by opening the MEX file named "SPECIMENS 60% relaxation – 2mm sample." After confirming the settings, initiate the data writing process from the PC to the product. Once the writing is finished, click the "OK" button. Transition back to the LabVIEW program and place the sample onto the water bath stage. Start a timer for a duration of 5 minutes and then select 'Set to starting height.' Subsequently, the plate will descend into the water bath and make contact with the sample. It's essential to verify the accuracy of the load cell pattern: ensure the plate makes proper contact with the sample's top surface. If any discrepancies are observed, examine the water bath's positioning, ensuring that the zero position is accurate.

Generate an empty text file with the appropriate name and utilize the file path button to choose the saving location for this file. Proceed once the load cell signal stabilizes (indicated by a flat line) and press "start test and recording". Monitor the relaxation process, which should last for 5 minutes. At the conclusion of the test, the plate will elevate to a higher position. Once the plate surpasses the water level, press 'stop recording.' Confirm that the test is complete and inspect that data have been successfully saved to the designated file (ensuring that the file size is no longer 0KB).

D

Appendix: Perform the tests on the tension tester

D.1. Set up and calibration

First, use a designated laptop and make sure that it is connected to a power source at all times. Then plug it into the tension tester by connecting the two USB cables to their respective USB ports on the laptop and access the system using the password provided to boot the laptop and complete the setup. Third, open the right Labview window and have the MEX file ready for calibration. After that, use weights of 10 grams, 20 grams and 50 grams to add force to the load cell respectively, and judge whether the calibration is successful by observing the signal value displayed on the laptop. When the calibration has been proven successful, the water bath can be prepared. The water bath should be properly set up by filling it with HEPES buffer. Then, link the bath buffer to the heating device, however, the buffer added before the experiment should not exceed the bottom of the clamp. Turn on the heating system and adjust it to heat the solution. It is essential to wait until the water bath has reached its ideal temperature, which should take at least five minutes, before starting the experiment, as shown in Figure D1.

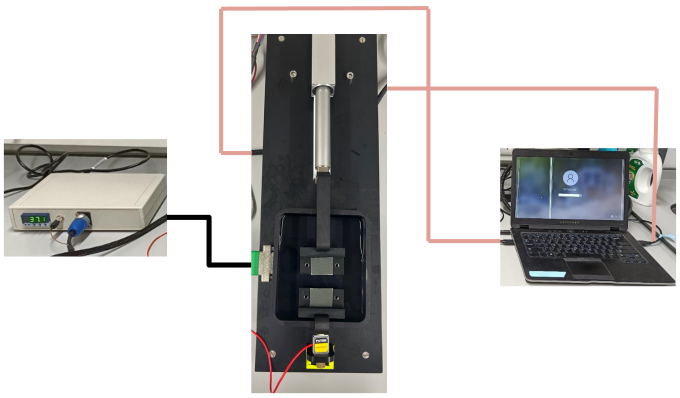

Figure D1: Set up for tension tester (top view)

D.2. Tensile test to failure

The next step of setup begins by setting the initial clamp distance at 15mm for tensile testing. Place the sample between the clamps and ensure it is aligned properly. Gradually place the sample on the clamps. Next, carefully tighten the clamps by placing them and the screws atop the sample. Tighten

the clamps slowly and uniformly using a torque screw set to 1cN. Fill the container with HEPE buffer to cover the sample and start a 5-minute timer.

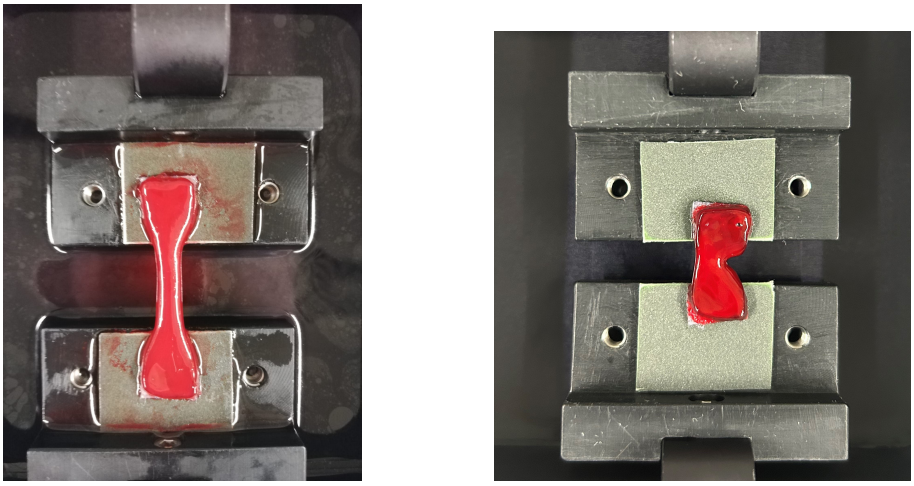

(a) Part of cutting mold with sample inside

(b) Along with the metal part for the notch

Figure D2: Cutting mold with sample inside

For pre-stretching, set the pre-stretch speed to 0.1mm/s, zero the load cell, and confirm the load cell reading by gently pulling with your fingers. Set the pre-stretch threshold to 0.0001N and then proceed with pre-stretching.

Next, the ultrasound measurement should be performed. Place the probe into the bath, taking care to avoid collisions. Adjust settings for the focal plane, depth, and visibility of the sample. Start recording and scan along the sample's length, acquiring 300 frames. After freezing a frame, rename the sample.

Next, a gauge length assessment is needed. Determine the test speed as 10% of this value, for instance, if the gauge length is 19.45mm, the test speed should be 1.95mm/s. Adjust the stretch and pre-stretch lines to this speed in the control panel, with a maximum of two decimal places. Rewrite the file accordingly.

To perform the test, navigate to LabVIEW, choose a save location and create an empty text file. Calibrate the load cell to zero. Initiate recording and start the test. Once the sample breaks, stop recording and halt movement. Return the clamps to their initial position. If the sample does not break, prevent a collision by stopping movement before it reaches the waterbath. Then, the clamps are returned to their starting position.

When unloading the sample, remove the liquid with a 50mL syringe until the clamps are clear. Unscrew the clamps, dispose of the sample, and prepare for the next iteration of the test.

D.3. Tensile relaxation test

The tensile relaxation test, follows exactly the same procedures as the last test before checking the gauge length and setting the test speed as well as the initial clamp distance. The only difference is that in the process of assessing the gauge length and configuring the test parameters, begin by accessing the MEX file labeled "SPECIMENS tensile relaxation." Initiate the remote operation teaching mode. Verify the current position, which represents the new gauge length. Adjust the stretch distance to the gauge length plus 25%. Modify the test speed to 10% of the gauge length and set the retraction distance to match the gauge length. Finally, revise the settings accordingly.

D.4. Fracture test

To prepare the sample for the fracture test, begin by creating a notch. Remove the sample from the mold and place it within a cutting mold to carefully craft the notch using the mold's features, as shown in Figure D.3(a). Handle the notched sample with precision, utilizing two tweezers to ensure the notch remains unaltered. Subsequently, the sample should be positioned between the clamps, confirming its

alignment. The initial clamp distance of this type of experiment is 8mm.

(a) Part of cutting mold with the sample inside

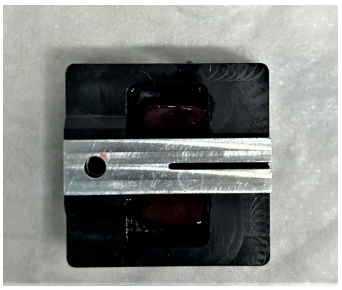

(b) Together with the metal part for the notch

Figure D3: Two different samples for tension tests and fracture tests, respectively.

Proceed to tighten the clamps by positioning them atop the sample, gradually and uniformly fastening them using a torque screw set to 1cN. Maintain a consistent clamping force of 1 cN. Replenish the bath with HEPEs buffer and initiate a 5-minute timer.

By finishing pre-stretching and ultrasonic measurement in the same steps as the tensile test to failure, the load cell has been calibrated to zero, and 300 frames of MRI images have been recorded.

Next, evaluate the gauge length and modify the test speed by accessing the MEX file ”SPECIMENS tensile stretch to failure.” Initiate remote operation teaching and confirm the current position as the new gauge length. Adjust the test speed to 10% of the gauge length and save the adjustments.

To execute the test, navigate to LabVIEW, select a save location, and create an empty text file. Calibrate the load cell to zero and initiate recording before commencing the test. Upon sample breakage, cease recording, halt movement, and return the clamps to the initial position.

For unloading, remove the liquid using a 50mL syringe until the clamps are free, then unscrew the clamps and dispose of the sample. Proceed to load the subsequent sample and repeat the process.

E

Appendix: Critical points selection during post-procession of mechanical results

During the post-processing of mechanical data files, the identification of starting points and ending points of each curve can pose a challenge, yet it holds paramount significance. The intricacies surrounding the determination of starting and ending points underscore the need for careful consideration in post-processing, as the accuracy of these determinations can significantly impact the overall quality and reliability of the results.

E.1. Starting point for high-strain and low-strain stiffness

These starting points (t_0) play a pivotal role in determining whether the end strain reaches the targeted 80% in the cyclic compression test. As shown in Figure E1, it is obvious that at t_1, the sample is supposed to be compressed to 80%, however, the initial part of the curve is bumpy and unstable which makes it challenging to determine the starting point (t_0). The problem is further complicated by the relatively small measured parameter values and high signal-to-noise ratio during the initial stages of compression testing. Consequently, achieving accurate assessments of low-strain stiffness becomes a complex task.

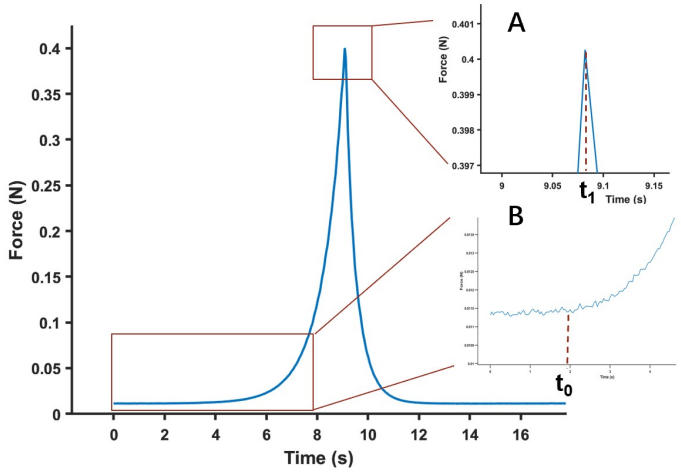

Figure E1: An example of the Force-Time curve in the compression tests. A. The ending point of the compression test is easy to determine; B. Starting point of the compression test challenges in terms of selection.

The test program specifies that the cyclic compression test initiates approximately 1.7 seconds after pressing the ”start” button, and after 8 seconds, the compression plate reaches a displacement of 1.6mm, signifying the peak point of the curve, corresponding to the intended 80% strain level. In essence, the accuracy of the 80% strain determination hinges on the precision of the starting point.

The high-strain segment, constituting 75% to 80%, within the stress-strain curve of the compression test conducted on all patient samples displays a distinctly linear behavior. In the context of an isotropic and uniform thrombus analogue, it is reasonable to anticipate that the corresponding low-strain portion of the curve should exhibit a similar linearity because the thrombus analogue is isotropic and uniform.

A reliable approach for assessing the validity of the starting point is by scrutinizing the stress-strain curve, specifically in the low-strain stiffness region. If the curve exhibits linearity within the 0%-10% strain range, it confirms the rationality of the starting point selection as shown in Figure E2. Conversely, a lack of linearity suggests an unreasonable starting point, indicating that the final high-strain data does not correspond to the intended 80% strain level. Besides, Table E1 shows that high-strain stiffness is very sensitive to the strain range when conducting the calculation. Even if the difference is only 4%, the error percentage is up to 39.17%. Consequently, it becomes imperative to exclude both high-strain stiffness and low-strain stiffness segments during the subsequent correlation analysis, as their accuracy is questionable and could compromise the overall integrity of the results. In this study, Patient_07, Patient_10, Patient_14, Patient_17, and Patient_26 were excluded according to this principle.

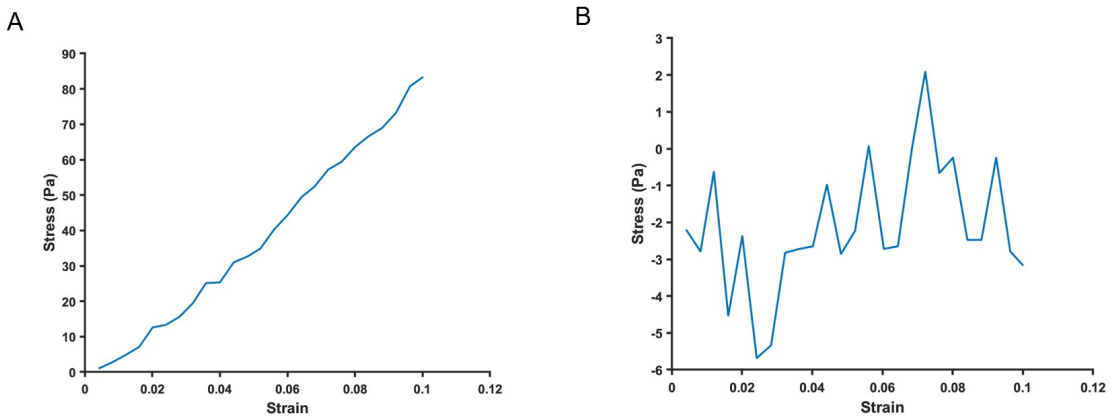

Figure E2: Two examples of the low-strain part of the Stress-Strain curve in the compression tests. A. Demonstration of a standard linear; B. Demonstration of a clear non-linear.

Table E1: Impact of not using the 75%-80% Strain Range on high-strain Stiffness Calculation

The window to calculate high-strain stiffness	75%-80%	74%-79%	73%-78%	72%-77%	71%-76%
high-strain stiffness (Pa)	1.23E+05	1.10E+05	9.58E+04	8.30E+04	7.46E+04
Error percentage (%) compared to the value of 75%-80%	0	10.27	21.94	32.38	39.17

E.2. Choosing the point of crack initiation for fracture toughness

As part of the approach to determine the fracture toughness, the energy produced from the integration of the Force(N)-Displacement(mm) curve in the fracture test must be determined [98]. When a crack initiates and begins to propagate within a sample, it is reasonable to assume that it will ultimately reach a state of stable, continuous propagation [99]. The transition from crack initiation to stable propagation is a complex issue that has not received comprehensive examination. As a result, this study only focuses on the phase of steady-state crack propagation.

Recognize that fracture toughness is determined before crack propagation begins, that is before the steady-state phase of the crack is established. The softening stage reaches its peak at the starting point

of material crack propagation. At this time, the force on the material suddenly decreases significantly, causing the force-displacement curve to drop rapidly, indicating material failure or fracture. Therefore, the ending point for calculating fracture toughness is the starting point of crack propagation, which is located before the material softening term (Point d_1 in Figure E3).

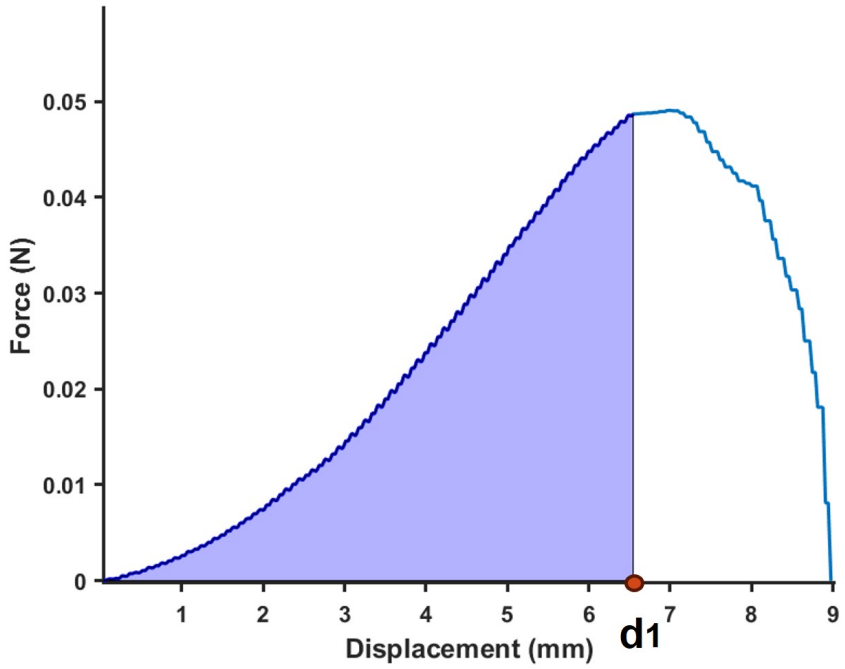

Figure E3: The typical Force(N)-Displacement(mm) obtained from fracture test. The area under the curve (purple) is the fracture toughness and the d_1 is the ending point of calculation for fracture toughness.

F

Appendix: Mechanical tests results and imaging characteristics for all patients

Table F1: Mechanical results from compression tests

Samples	High strain stiffness (Pa)	Low strain stiffness (Pa)	Hysteresis areas (Pa)	Hysteresis ratio	Clot contraction ratio
Patient_01					
Patient_02	2.54E+05	454.00	1.61E+03	0.43	0.59
Patient_03					
Patient_04	1.93E+05	163.30	1.11E+03	0.47	0.58
Patient_05					
Patient_06	1.48E+05	385.90	1.08E+03	0.55	0.65
Patient_07	1.23E+05	21.24	5.58E+02	0.48	0.6
Patient_08	2.71E+05	872.50	2.25E+03	0.43	0.57
Patient_09	2.30E+05	431.10	1.49E+03	0.43	0.58
Patient_10	0.62E+05	57.24	3.44E+02	0.57	0.25
Patient_11	2.65E+05	459.50	1.85E+03	0.40	0.62
Patient_12	1.60E+05	432.50	1.81E+03	0.54	0.54
Patient_13	2.38E+05	276.80	1.40E+03	0.41	0.54
Patient_14	1.55E+05	98.51	9.18E+02	0.46	0.59
Patient_15					
Patient_16	2.22E+05	854.80	1.67E+03	0.53	0.56
Patient_17	1.18E+05	68.50	7.24E+02	0.49	0.48
Patient_18	1.75E+05	203.90	1.11E+03	0.47	0.67
Patient_19	2.18E+05	704.80	2.65E+03	0.60	0.60
Patient_20	2.30E+05	592.70	1.70E+03	0.42	0.57
Patient_21	1.98E+05	366.40	1.38E+03	0.45	0.61
Patient_22	2.89E+05	899.10	2.33E+03	0.42	0.62
Patient_23	1.66E+05	1071.00	1.60E+03	0.48	0.73
Patient_24	1.18E+05	221.30	8.08E+02	0.43	0.52
Patient_25					
Patient_26	0.81E+05	31.60	4.58E+02	0.45	0.50
Patient_27	2.05E+05	476.10	1.67E+03	0.39	0.55
Patient_28					
Patient_29	2.89E+05	1633.00	2.31E+03	0.40	0.74

Table F2: Mechanical results from tensile tests

Samples	Tensile stiffness (Pa)	Ultimate tensile stress (Pa)	Ultimate tensile strain	Fracture toughness (J)
Patient_01				
Patient_02	5.78E+03	5.35E+03	1.01	7.68E-02
Patient_03				
Patient_04	4.96E+03	5.12E+03	1.06	1.45E-01
Patient_05				
Patient_06	2.28E+03	1.17E+03	0.53	2.80E-03
Patient_07	5.16E+03	2.96E+03	0.60	9.30E-02
Patient_08	7.36E+03	7.81E+03	1.10	1.31E-01
Patient_09				2.63E-01
Patient_10	2.87E+03	1.70E+03	0.61	1.39E-01
Patient_11	12.01E+03	16.66E+03	1.37	
Patient_12	3.89E+03	1.43E+03	0.37	1.06E-01
Patient_13	10.64E+03	10.55E+03	1.04	3.19E-01
Patient_14	4.71E+03	2.56E+03	0.56	3.00E-01
Patient_15				
Patient_16				3.11E-01
Patient_17	5.66E+03	5.24E+03	0.95	9.23E-02
Patient_18				1.36E-01
Patient_19	5.77E+03	3.27E+03	0.58	2.93E-01
Patient_20	7.34E+03	8.74E+03	1.26	8.84E-02
Patient_21	6.01E+03	3.89E+03	0.66	
Patient_22	10.74E+03	13.05E+03	1.20	1.84E-01
Patient_23	9.33E+03	7.55E+03	0.83	6.64E-02
Patient_24	5.14E+03	3.80E+03	0.79	3.84E-02
Patient_25				
Patient_26	8.86E+03	10.54E+03	1.19	1.07E-01
Patient_27	11.32E+03	14.86E+03	1.29	2.35E-01
Patient_28				
Patient_29	14.92E+03	21.38E+03	1.49	3.31E-01

Table F3: The material parameters obtained by fitted by two-term Prony series

Sample	g_{inf}		g_1		t_1		g_2		t_2		R^2	
	Compression	Tensile	Compression	Tensile	Compression	Tensile	Compression	Tensile	Compression	Tensile	Compression	Tensile
Patient_02	0.521	0.679	0.241	0.120	141.410	119.750	0.241	0.120	141.410	119.750	0.9982	0.9866
Patient_04	0.199	0.771	0.396	0.104	6.826	97.893	0.396	0.104	6.826	97.893	0.9974	0.9963
Patient_06	0.345		0.322		103.878		0.322		103.878		0.9980	
Patient_07	0.327	0.737	0.246	-4.593	72.862	64.846	0.246	-4.593	72.862	64.846	0.9969	0.9556
Patient_08	0.151	0.753	0.406	0.101	7.303	93.222	0.406	0.101	7.303	93.222	0.9977	0.9946
Patient_09	0.395	0.672	0.239	0.135	91.983	6.442	0.239	0.135	91.983	6.442	0.9968	0.9952
Patient_10	0.508	0.722	0.111	0.100	49.000	6.652	0.111	0.100	49.000	6.652	0.9919	0.9934
Patient_11	0.330	0.768	0.411	0.100	105.060	5.801	0.411	0.100	105.060	5.801	0.9992	0.9945
Patient_12	0.188	0.722	0.391	0.100	79.199	8.752	0.391	0.100	79.199	8.752	0.9987	0.9893
Patient_13	0.214	0.749	0.350	0.102	7.659	87.058	0.350	0.102	7.659	87.058	0.9981	0.9950
Patient_14	0.120	0.709	0.410	0.134	61.604	108.703	0.410	0.134	61.604	108.703	0.9987	0.9965
Patient_16	0.317		0.243		80.525		0.243		80.525		0.9964	
Patient_17	0.231	0.736	0.233	-0.469	47.696	66.105	0.233	-0.469	47.696	66.105	0.9950	0.9601
Patient_18	0.205		0.364		65.571		0.364		65.571		0.9987	
Patient_19	0.238	0.718	0.413	0.121	87.330	5.248	0.413	0.121	87.330	5.248	0.9990	0.9935
Patient_20	0.211	0.668	0.445	0.131	101.438	5.580	0.445	0.131	101.438	5.580	0.9991	0.9937
Patient_21	0.219	0.761	0.349	0.096	7.586	95.069	0.349	0.096	7.586	95.069	0.9981	0.9915
Patient_22	0.199	0.709	0.340	0.118	7.179	6.202	0.340	0.118	7.179	6.202	0.9977	0.9932
Patient_23	0.411	0.751	0.263	0.100	7.052	6.162	0.263	0.100	7.052	6.162	0.9960	0.9945
Patient_24	0.256	0.678	0.339	0.180	8.174	155.661	0.339	0.180	8.174	155.661	0.9979	0.9969
Patient_26	0.228		0.373		5.899		0.373		5.899		0.9970	
Patient_27	0.218	0.739	0.396	0.105	7.310	109.617	0.396	0.105	7.310	109.617	0.9970	0.9945
Patient_29	0.518	0.678	0.219	0.113	132.164	100.019	0.219	0.113	132.164	100.019	0.9981	0.9944

Table F4: Imaging characteristics from clinical data

Samples	DT (mm)	Thrombus length (mm)	Perviousness (HU)	Thrombus attenuation (HU)	Mean CTA density (HU)
Patient_04	7.25	25.12	3.11	53.22	56.33
Patient_06	8.35	29.15	14.31	27.76	42.07
Patient_07	26.30	21.34	9.38	47.42	56.80
Patient_08	1.79	9.26	26.10	38.89	65.00
Patient_10	21.49	57.86	-16.39	63.24	46.85
Patient_11	8.99	30.40	-1.37	34.81	33.43
Patient_12	82.44	14.32	52.23	32.86	85.08
Patient_14	21.09	16.59	27.70	41.37	69.07
Patient_18	34.33	24.50	0.49	28.03	28.52
Patient_19	9.84	30.50	-4.00	48.81	44.81
Patient_22	24.69	14.46	66.33	36.23	102.56
Patient_26	16.10	8.30	49.00	26.63	75.63
Patient_29	21.92	15.62	18.03	29.27	47.31

Table F5: Imaging characteristics from clinical data second part continued

Samples	HU prox NCCT (HU)	HU mid NCCT (HU)	HU dis NCCT (HU)	HU prox CTA (HU)	HU mid CTA (HU)	HU dis CTA (HU)
Patient_04	50.64	55.16	53.86	61.16	60.96	46.88
Patient_06	24.20	32.18	26.91	45.89	36.13	44.20
Patient_07	59.17	45.94	37.16	33.30	68.90	68.21
Patient_08	37.01	40.19	39.48	74.89	58.01	62.08
Patient_10	68.83	69.10	51.78	51.46	53.61	35.46
Patient_11	31.39	32.48	40.55	33.04	30.99	36.27
Patient_12	28.19	38.24	32.14	75.40	89.76	90.09
Patient_14	44.74	36.75	42.62	96.22	53.34	57.64
Patient_18	27.53	26.55	30.00	54.91	20.11	10.53
Patient_19	55.00	42.89	48.56	48.67	45.44	40.33
Patient_22	34.70	36.54	37.46	129.86	97.57	80.26
Patient_26	26.05	28.87	24.96	62.85	93.73	70.29
Patient_29	28.93	28.74	30.15	41.63	41.11	59.18

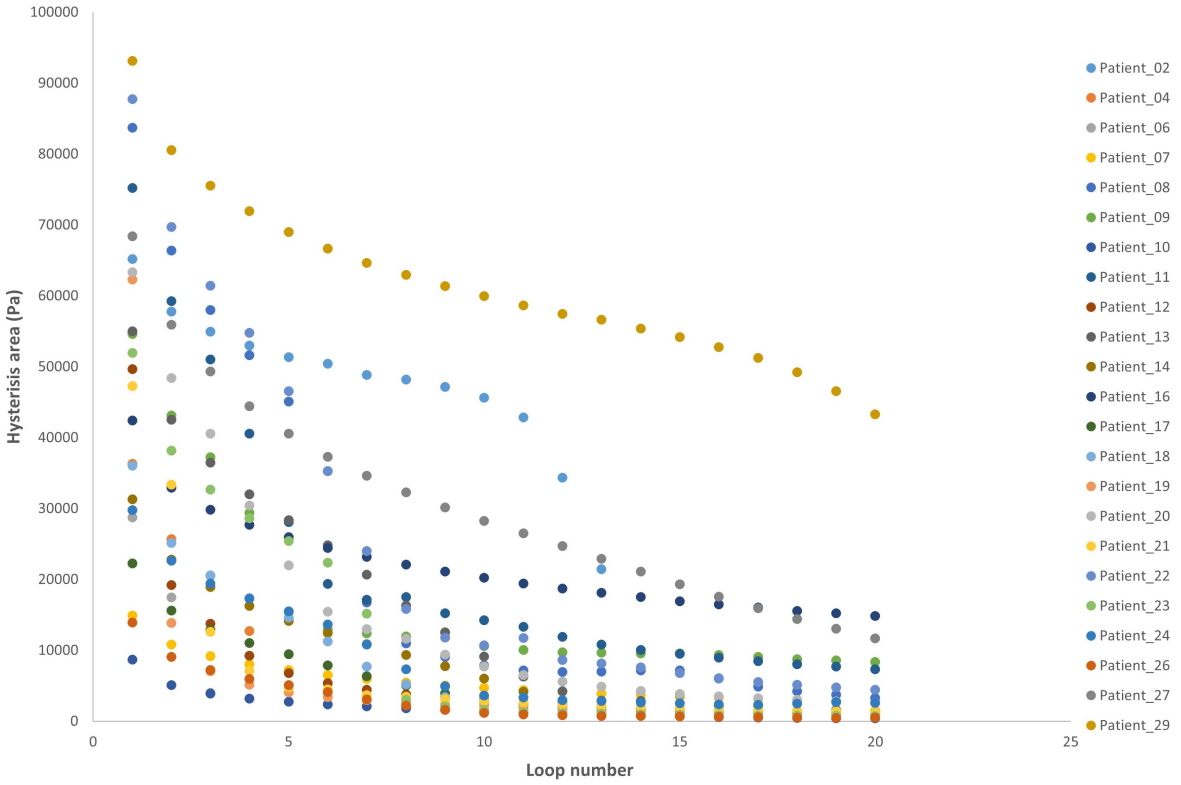

Figure F1: The variety of hysteresis areas along 20 loops for all patients.

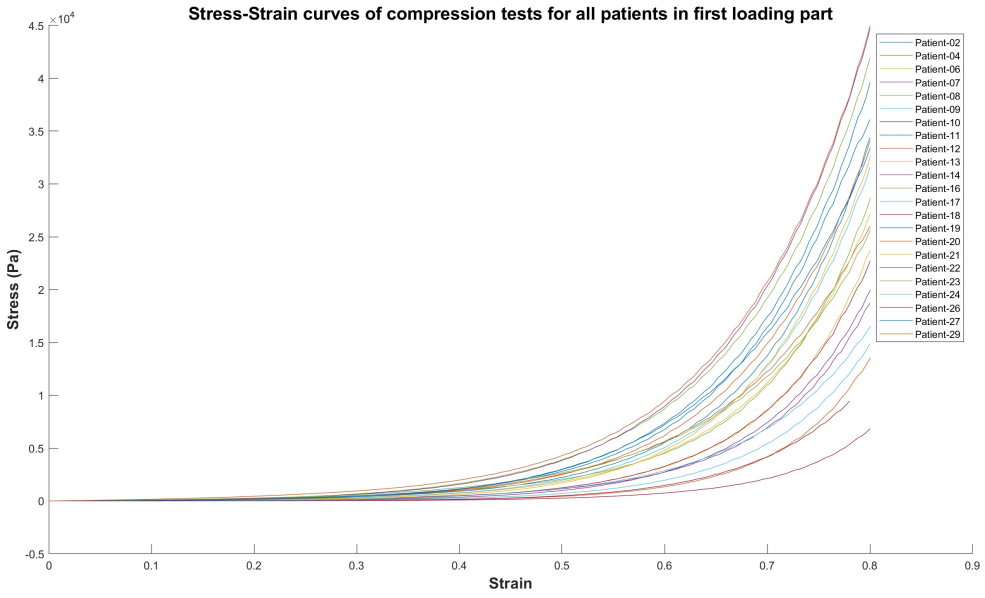

Figure F2: The first loading part of cyclic compression test for all patients.

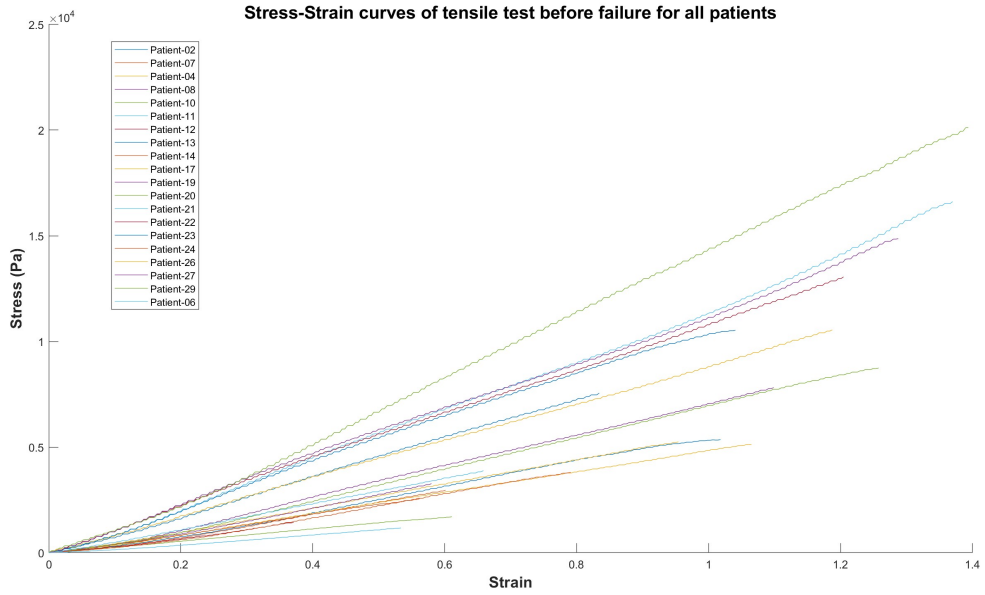

Figure F3: The stress-strain curves of tensile test before failure for all patients.

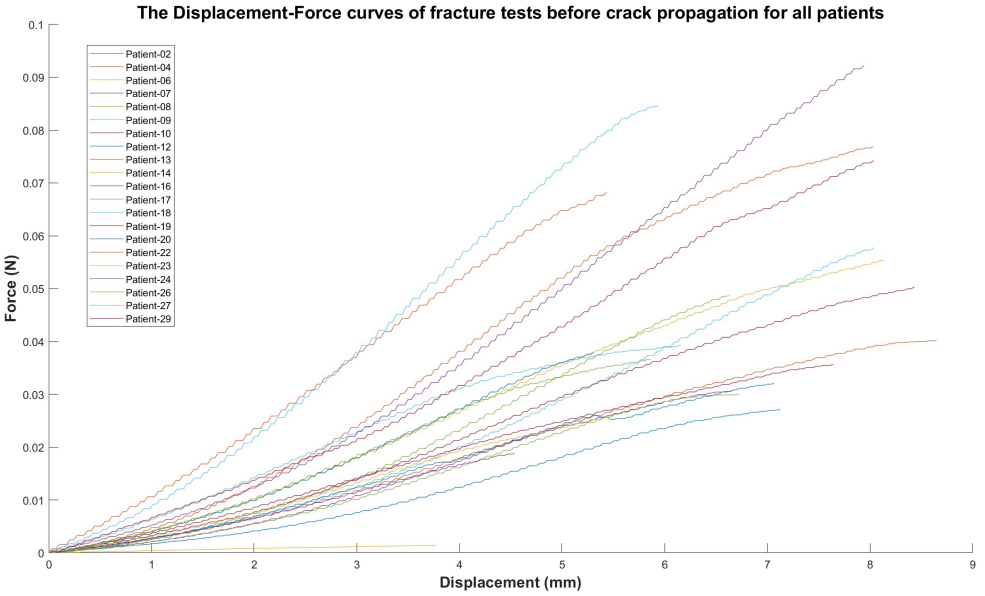

Figure F4: The Displacement-Force curves of fracture tests before crack propagation for all patients.

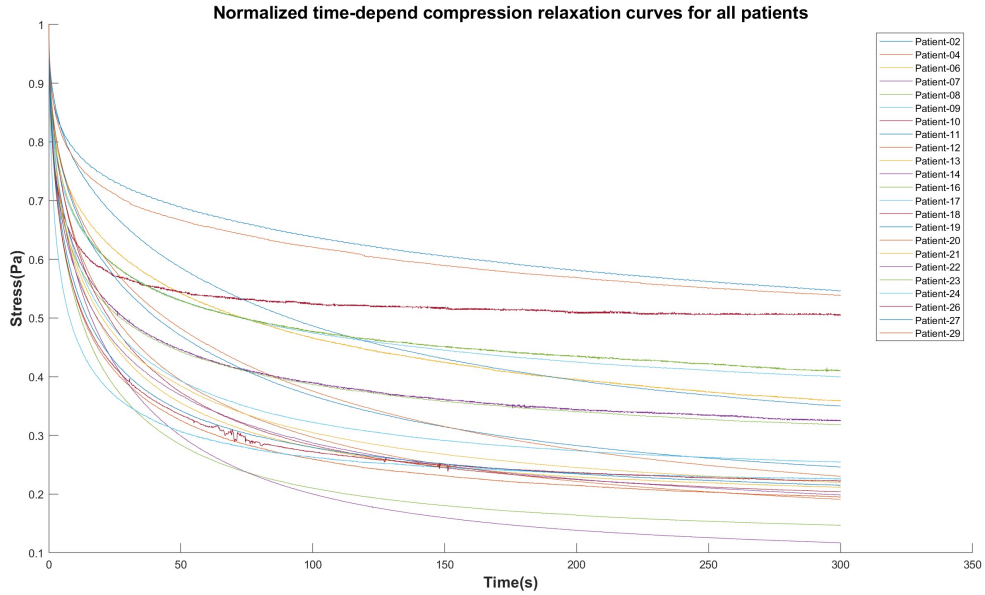

Figure F5: The compression stress relaxation tests for all patients.

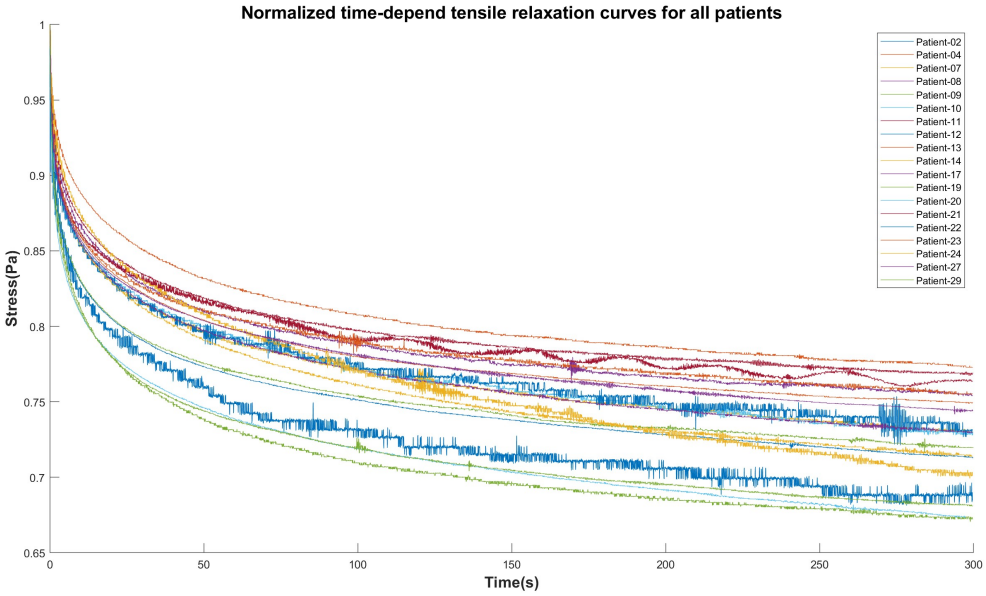

Figure F6: The tensile stress relaxation tests for all patients.

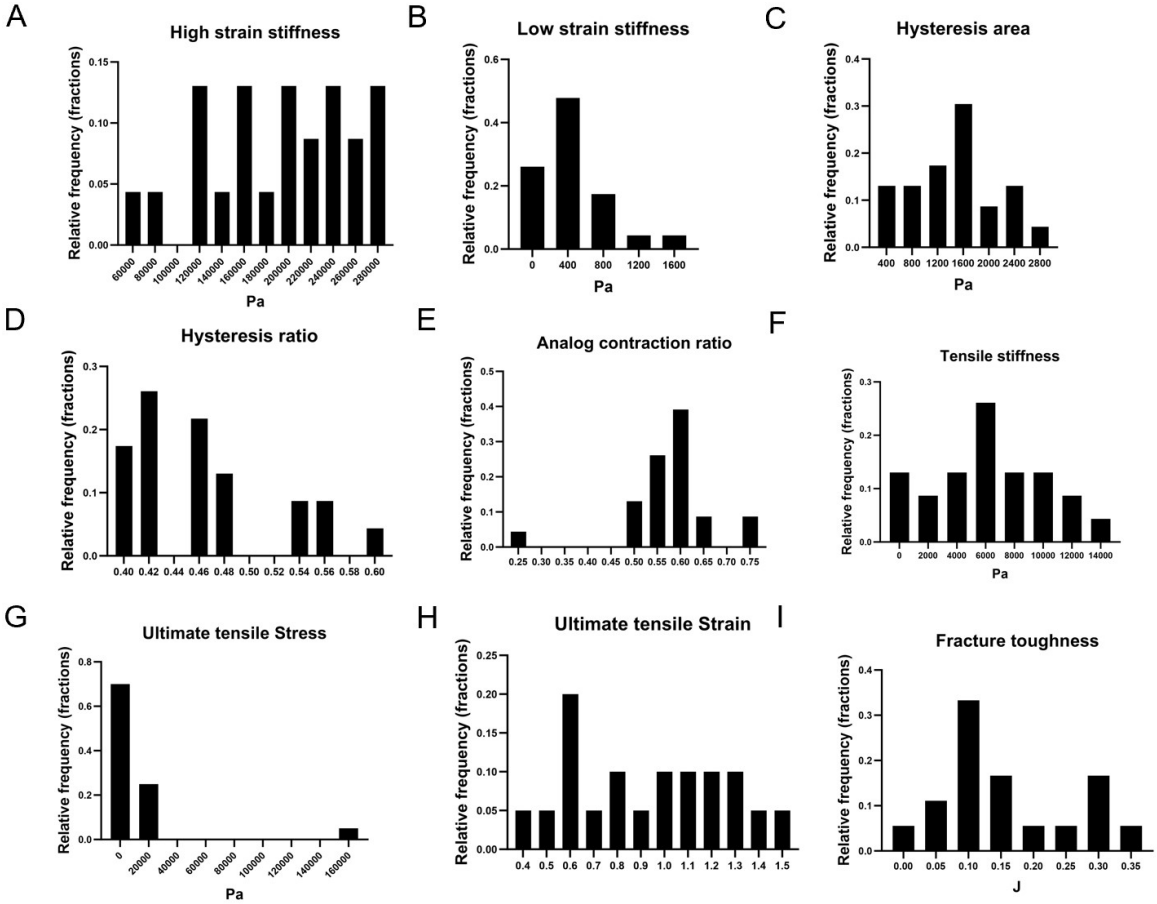

Figure F7: Histograms of the mechanical parameters. A. high-strain stiffness (Pa) histogram; B. low-strain stiffness (Pa) histogram; C. Hysteresis area (Pa) histogram; D. Hysteresis ratio histogram; E. Analog contraction ratio histogram; F. Tensile stiffness (Pa) histogram; F. Ultimate tensile stress (Pa) histogram; G. Ultimate tensile strain histogram; I. Fracture toughness (J) histogram.

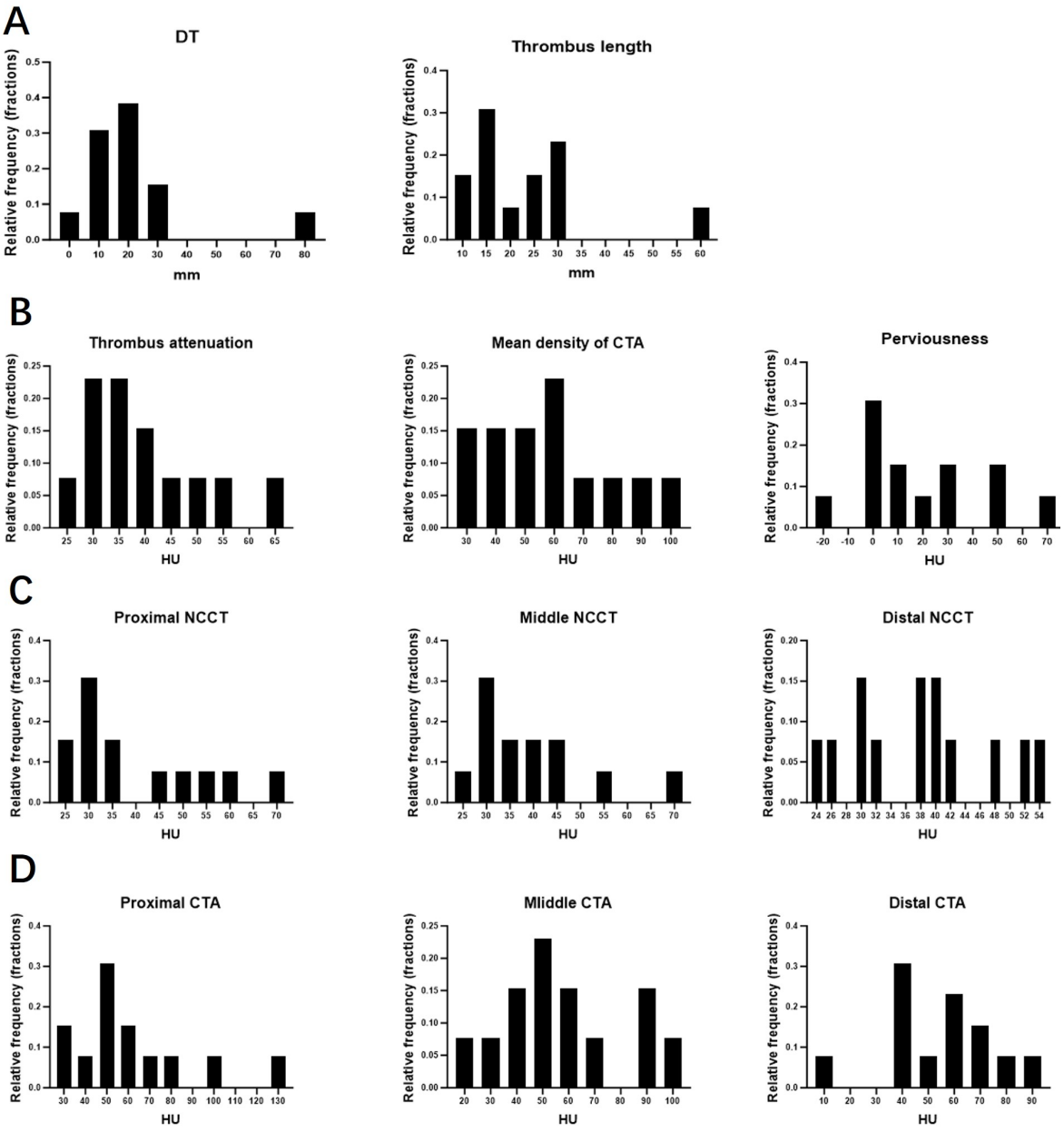

Figure F8: Histograms of the imaging characteristics. Line A: Distance from ICA-T (DT), thrombus length; Line B: Thrombus attenuation, the mean density of CTA, perviousness; Line C. Density values of three ROIs from NCCT; Line D: Density values of three ROIs from CTA.

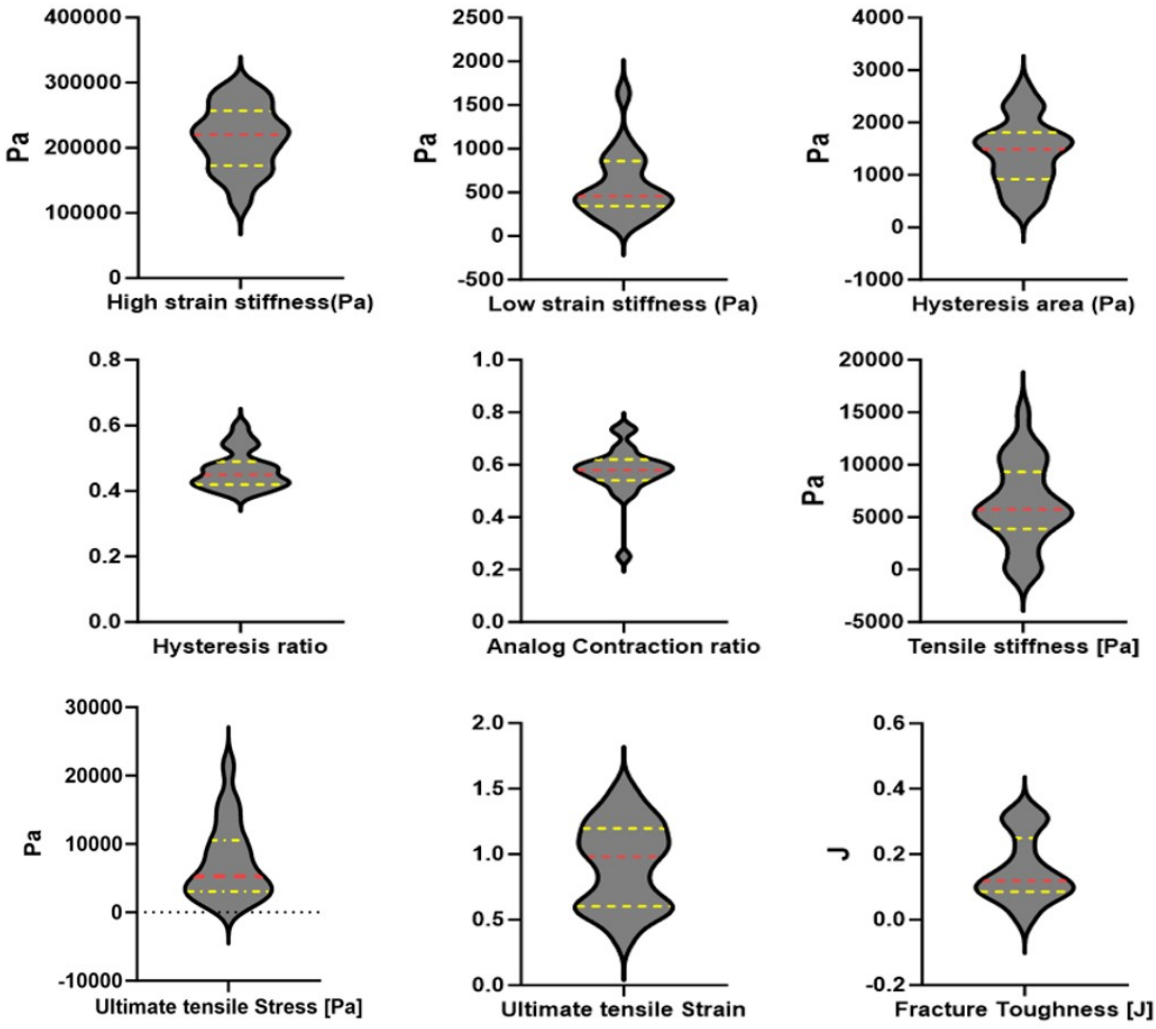

Figure F9: The violin plots for mechanical measurements with median (red dash line) and interquartile (yellow dash line).

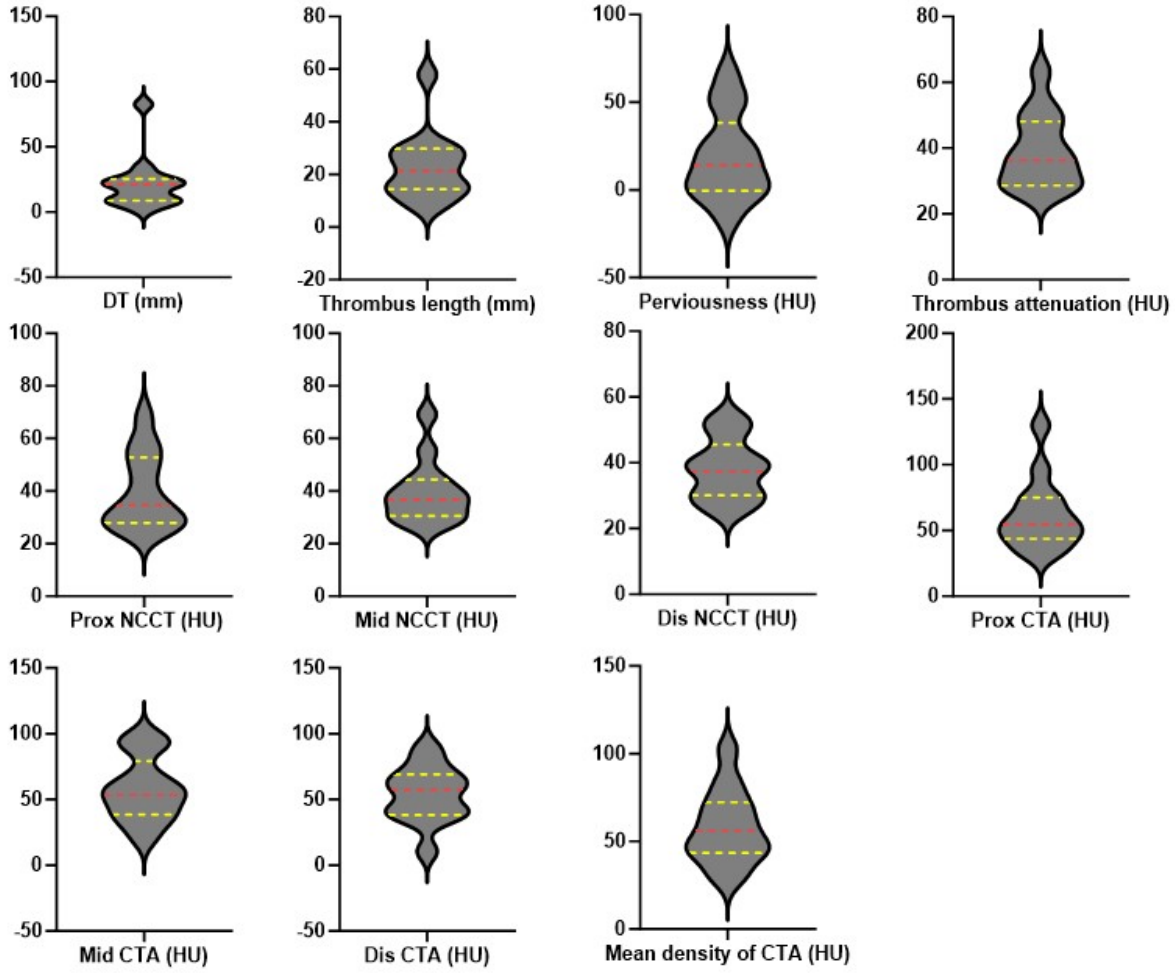

Figure F10: The violin plots for imaging measurements with median (red dash line) and interquartile (yellow dash line).

G

Computational model fitting

In this Appendix, the results of fitting experimental data using the Yeoh model are shown in Figure G1 and corresponding model parameters are shown in Table G1

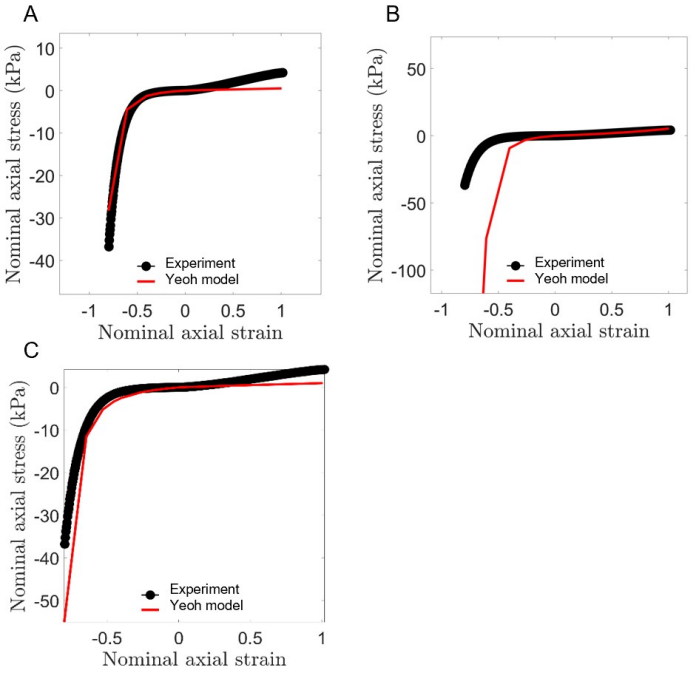

Figure G1: Stress-strain curve for fitting complete curve by three-term Yeoh model. A. The compression segment exhibited a satisfactory fit, while the tensile portion did not attain a suitable fit; B. The tensile segment exhibited a satisfactory fit, while the compression portion did not attain a suitable fit. C. Merging the parameters from the preceding two sets, neither segment of the curves demonstrates a satisfactory fit.

Table G1: The corresponding model parameters

	c_1 (MPa)	c_2 (MPa)	c_3 (MPa)	d_1	d_2	d_3
A	2.5E-04	2.8E-05	-4.5E-07	20	20	20
B	2.5E-02	2.8E-05	-4.5E-07	20	20	20
C	5E-04	2.8E-05	-4.5E-07	20	20	20

H

Source Code

MATLAB Code to calculate hysteresis are of first unconfined compression test loop.

```
%% 1. Load data and assign variables
%clear previous work
clc
clear all
close all;

saveFolder = 'D:\Mechanical_Tests\CC';
%make current working folder

T = readtable('Files/SPEC_cc_10.txt'); %load data from text file
timestamp = T{:,1};
force = T{:,2};

timeSec = seconds(timestamp - timestamp(1));
time = round(timeSec,3);

PlotFigures(time,force,'Time (s)','Force (N)',saveFolder)

%% 2. Crop the data
% Select beginning and starting points from figure(1) using zoom and data points
startTime = 1.075;
[~,endIdx] = min(abs(time-( startTime+16*20))); % 4 means there are 4 loops
endTime = time(endIdx);
startIdx = find(time==[[startTime]]); %search for index of start point
%endIdx = find(time==[[endTime]]); %search for index of end point
newtime=time(startIdx:endIdx)-time(startIdx); %zero the time
newforce= force(startIdx:endIdx)-force(startIdx); %zero the force
Stress=newforce./0.000035551; %CSA in m2
PlotFigures(newtime,Stress,'Time (s)','Stress (Pa)',saveFolder)

% 3. Write all stress-time data to excel file
WriteToExcel('time (s)', newtime ,'A','04_Hystersis_allcycles.xlsx');
WriteToExcel('stress (Pa)', Stress ,'B','04_Hystersis_allcycles.xlsx');
%% Find indices of loop starting points
% Calculate the number of data points per loop ( each loop lasts 16 seconds)
% Apply offset
offset = abs(min(Stress));
Stress=Stress+offset;

% Calculate area under each loop

N= 0:16:16*20;%320 means there are 20 loops, so 4 loops should be 64

indices = zeros(size(N));

rawdata(:,1) = newtime;
rawdata(:,2) = Stress;

for i = 1:length(N)
```

```
    diff= abs(N(i)-newtime);
    [~,loopIdx]= min(diff);
    indices(i) = loopIdx;
end

for j = 1:(length(indices)-1)
    tempdata = rawdata(indices(j):indices(j+1),:);
    areas(j) = trapz(tempdata(:,1), tempdata(:,2));

end

% Write areas to Excel file
%%
xlswrite('05_20loopsArea.xlsx', areas', '20_loops', 'H2');
disp('Areas written to output.xlsx');
```

MATLAB Code to calculate mechanical characteristics including high-strain stiffness, low-strain stiffness, tensile stiffness and fracture toughness.

```
clc
clear all
close all;

saveFolder = 'D:\Mechanical_Tests\CC';
%  20 loop Compression test data
T = readtable('Files\SPEC_cc_13.txt'); %load data from text file
timestamp = T{:,1};
force = T{:,2};

timeSec = seconds(timestamp - timestamp(1));
time = round(timeSec,3);

PlotFigures(time,force,'Time (s)','Force (N)',saveFolder)

%% First loop

[peakValues, indexes] = findpeaks(force, 'MinPeakHeight', 0.05);
tValues = time(indexes);
peak = tValues(1);

start = peak - 8;

%% crop curve
[~,beginIdex]=min(abs(time-start));
startTime=time(beginIdex);
endTime = peak;
startIdx = find(time==[[startTime]]); %search for index of start point
endIdx = find(time==[[endTime]]); %search for index of end point
newtime =time(startIdx:endIdx)-time(startIdx); %zero the time
newforce = force(startIdx:endIdx)-force(startIdx); %zero the force
displacement=newtime.*0.2; %these values remain the same for all SPECIMENS compression
    analysis (0.2)
% PlotFigures(-displacement, -newforce,'Displacement(mm)','Force(N)', saveFolder)
%
% WriteToExcel('Displacement(mm)', -displacement,'A','06_Force_Displacement.xlsx');
% WriteToExcel('Force(N)', -newforce ,'B','06_Force_Displacement.xlsx');
%
area=0.000028677;
Strain=displacement./2; %these values remain the same for all SPECIMENS compression analysis
Stress=newforce./area; %CSA in m2
PlotFigures(Strain, Stress,'Strain','Stress (Pa)', saveFolder)
total_area = trapz(Strain, Stress);
%% First loading part write to excel
WriteToExcel('Strain', Strain ,'A','00_First_loading_part.xlsx');
WriteToExcel('stress (Pa)', Stress ,'B','00_First_loading_part.xlsx');

writeDataToExcel( '01_CompleteCurve.xlsx','SPEC_10', -Strain, -Stress);
%% Hystersis area
close all

jieshutime = peak + 8;
```

```
[~,jieshuIdex]=min(abs(time-jieshutime));
jieshuTime=time(jieshuIdex);
endIdx=jieshuIdex;
newtime =time(startIdx:endIdx)-time(startIdx); %zero the time
newforce = force(startIdx:endIdx)-force(startIdx); %zero the force
Strain2=newtime.*(newtime<=(peak-startTime))*0.1+(0.1*(peak-startTime)-0.1*(newtime-(peak-
    startTime))).*(newtime>(peak-startTime));
Stress2=newforce./area; %CSA in m2

x=Strain2;
y=Stress2;
area= trapz(x,y);

PlotFigures(Strain2, Stress2,'Strain','Stress (Pa)', saveFolder)
fill(x,y, 'r');
hold off;

%% Hystersis first loop
WriteToExcel('Strain', Strain2 ,'A','02_Hystersis_first_loop.xlsx');
WriteToExcel('stress (Pa)', Stress2 ,'B','02_Hystersis_first_loop.xlsx');

%% 75%-80%
close all

[~,newstartIdx] = min(abs(Strain-0.75));
[~,newendIdx] = min(abs(Strain-0.80));
highstrain = Strain(newstartIdx+1:newendIdx);
highstress = Stress(newstartIdx+1:newendIdx);
PlotFigures(highstrain, highstress,'Strain','Stress (Pa)', saveFolder)
%% 0%-10%
close all

[~,lstartIdx] = min(abs(Strain-0));
[~,lendIdx] = min(abs(Strain-0.1));
lowstrain = Strain(lstartIdx+1:lendIdx);
lowstress = Stress(lstartIdx+1:lendIdx);

PlotFigures(lowstrain, lowstress,'Strain','Stress (Pa)', saveFolder)

%% Tensile To Failure data
close all
clc
saveFolder = 'D:\Mechanical_Tests\CC';
T1 = readtable('Files\SPEC_tf_07.txt'); %load data from text file
timestamp1 = T1{:,1};
force1 = T1{:,2};

timeSec1 = seconds(timestamp1 - timestamp1(1));
time1 = round(timeSec1,3);

PlotFigures(time1,force1,'Time (s)','Force (N)',saveFolder)
%% crop curve
startTime1 = 1.839;
endTime1 = 7.838;
startIdx1 = find(time1==[[startTime1]]); %search for index of start point
endIdx1 = find(time1==[[endTime1]]); %search for index of end point
newtime1 =time1(startIdx1:endIdx1)-time1(startIdx1); %zero the time
newforce1 = force1(startIdx1:endIdx1)-force1(startIdx1); %zero the force
displacement1=newtime1.*1.53; %this value will change for ever test, refer to information
    sheet (speed mm/s)
Strain1=displacement1./15.3; %this value will change for ever test, refer to information
    sheet (starting distance mm)
Stress1=newforce1./0.000010996; %CSA in m2
PlotFigures(displacement1, newforce1 ,'Displacement( mm','Force(N)',saveFolder) %Get the end
    strain
% WriteToExcel('Displacement( mm', displacement1 ,'A','07_Before_failure_F_D.xlsx');
% WriteToExcel('Force(N)',newforce1 ,'B','07_Before_failure_F_D.xlsx');

PlotFigures(Strain1, Stress1,'Strain','Stress(Pa)',saveFolder) %Get the end strain
%%
WriteToExcel('Strain', Strain1 ,'A','03_Before_failure.xlsx');
```

```
WriteToExcel('stress (Pa)', Stress1 ,'B','03_Before_failure.xlsx');

writeDataToExcel( '01_CompleteCurve.xlsx','SPEC_06', Strain1, Stress1);

%% Plot in one coordinate system

PlotFigures(-Strain, -Stress,'Strain','Stress (Pa)', saveFolder)
hold on
PlotFigures(Strain1, Stress1,'Strain','Stress (Pa)', saveFolder)

ax=gca;
ax.XAxisLocation = 'origin';
ax.YAxisLocation = 'origin';

%% Fracture
clc
clear all
close all;
saveFolder = 'D:\Mechanical_Tests\CC';

T = readtable('Files\SPEC_f_06.txt'); %load data from text file
timestamp = T{:,1};
force = T{:,2};
timeSec = seconds(timestamp - timestamp(1));
time = round(timeSec,3);
PlotFigures(time,force,'Time (s)','Force (N)',saveFolder)

startTime=2.519;
endTime =6.759;  % fracture time
endTimeEnd = 12.48;
startIdx = find(time==[[startTime]]); %search for index of start point
endIdx = find(time==[[endTime]]); %search for index of end point
endIdx1 = find(time==[[endTimeEnd]]);
newtime =time(startIdx:endIdx)-time(startIdx); %zero the time
newforce = force(startIdx:endIdx)-force(startIdx); %zero the force
%Fulltime= time(startIdx:endIdx1)-time(startIdx);

displacement=newtime .*0.89;
Fulldisplacement=Fulltime .*0.81;
Fullforce= force(startIdx:endIdx1)-force(startIdx);

%PlotFigures(displacement,newforce,'Displacement (mm)','Force (N)',saveFolder)
WriteToExcel('Displacement( mm', displacement ,'A','06_Force_Displacement.xlsx');
WriteToExcel('Force(N)',newforce ,'B','06_Force_Displacement.xlsx');

%% Fracture toughness
%x=displacement(startIdx:endIdx);
x=displacement;
y=newforce;
plot(x,y)
xi = linspace(min(x), max(x), 1000);
yi = interp1(x, y, xi, 'spline');

PlotFigures(Fulldisplacement,Fullforce,'Displacement (mm)','Force (N)',saveFolder)

hold on
plot(xi, yi, 'b-', 'LineWidth', 1.5);
hold on;

fill([xi, fliplr(xi)], [yi, zeros(1, length(yi))], 'b', 'FaceAlpha', 0.3);
hold off

area = trapz(x,y);
```

MATLAB code for calculating fitting parameters of one-term and two-term Prony series for compression relaxation and tensile stress relaxation.

```
clc
clear all
close all;

```

```
saveFolder = 'D:\Mechanical_Tests\CC';

T = readtable('Files/SPEC_tr_08.txt'); %load data from text file
timestamp = T{:,1};
force = T{:,2};

timeSec = seconds(timestamp - timestamp(1));
time = round(timeSec,3);

PlotFigures(time,force,'Time (s)','Force (N)',saveFolder)

startTime = 6.121;
startIdx = find(time==[[startTime]]);
End=305.999;
[~,endIdx]=min(abs(time-End));
endTime= time(endIdx);
%% 2. Crop data for testing cycle
%select start and end of the loading curve

newtime =time(startIdx:endIdx)-time(startIdx); %zero the time
%newforce = force(startIdx:endIdx)-force(startIdx); %zero the force
newforce = force(startIdx:endIdx);
%PlotFigures(newtime,newforce,'Time (s)','Stress (Pa)',saveFolder)

%% 3. Curve of Stress vs. time
Stress=newforce./0.00000755;
%PlotFigures(newtime,Stress,'Time (s)','Stress (Pa)',saveFolder)
% WriteToExcel('Time (s)', newtime ,'A','00_SPECIMENS_tensile_relaxation_data.xlsx');
% WriteToExcel('Stress (Pa)', Stress ,'B','00_SPECIMENS_tensile_relaxation_data.xlsx');

%% Fit to Prony Series
peakValue=max(Stress,[],"all");
t = newtime;
y = Stress./peakValue;
PlotFigures(t,y,'Time (s)','Stress (Pa)',saveFolder)

% WriteToExcel('Time (s)', t ,'A','01_Normalized_SPECIMENS_tensile_relaxation_data.xlsx');
% WriteToExcel('Stress (Pa)', y ,'B','01_Normalized_SPECIMENS_tensile_relaxation_data.xlsx');

%% one term Prony
 f=  @(p,t) p(1) + p(2)*exp(-t/p(3));

% Define initial guess for parameters
p0 = [ 1,1,1];
% Set lower and upper bounds for parameters
lb = [0, -Inf, 0  ];
ub = [Inf, Inf, Inf];

% Fit Prony series equation to data

maxNumberIterations=10000000; %Maximum number of optimization iterations

OPT_options = optimoptions(@lsqcurvefit,'Algorithm','levenberg-marquardt');
OPT_options = optimoptions(OPT_options,'MaxIter',maxNumberIterations);
%OPT_options = optimoptions('lsqcurvefit', 'TolFun', 1e-12); % Set the threshold value to 1e
    -6


[p] = lsqcurvefit(f, p0, t, y, lb, ub, OPT_options);


%  options=optimset;
%  options.MaxIterations = 1000;
%  [p,resnorm,residual,exitflag,output] = lsqcurvefit(f, p0, t, y, lb, ub,options);

% Calculate sum of squared residuals

SST = sum((y-mean(y)).^2); % Total sum of squares
SSE = sum((f(p,t)-y).^2); % sum of squared residuals
R2 = 1- (SSE/SST);

```

```
% Plot results
fit = f(p, t);
plot(t, y, 'b-', t, fit, '-')
xlabel('Time(s)')
ylabel('Stress(Pa)')

columnNames = {'g_inf', 'g_1', 't_1'};
filename = '02_PronySeries_oneterm.xlsx';

 T = table(p', 'VariableNames', columnNames');
 writetable(T, filename, 'Sheet', SPEC_02);

 WriteToExcel('g_inf', p(:,1) ,'B','02_PronySeries_tr.xlsx');
 WriteToExcel('g_1', p(:,2) ,'C','02_PronySeries_tr.xlsx');
 WriteToExcel('t_1', p(:,3) ,'D','02_PronySeries_tr.xlsx');
 WriteToExcel('R^2', R2 ,'E','02_PronySeries_tr.xlsx');
% Two-term Prony
f=  @(p,t) p(1) + p(2)*exp(-t/p(3)) +p(4)*exp(-t/p(5));

% Define initial guess for parameters
p0 = [ 1,1,1,1,1];
% Set lower and upper bounds for parameters
lb = [0, -Inf, 0 , -Inf, 0 ];
ub = [Inf, Inf, Inf, Inf, Inf];


% Fit Prony series equation to data

maxNumberIterations=1000000; %Maximum number of optimization iterations
OPT_options = optimoptions(@lsqcurvefit,'Algorithm','levenberg-marquardt');
OPT_options = optimoptions(OPT_options,'MaxIter',maxNumberIterations);

[p] = lsqcurvefit(f, p0, t, y, lb, ub, OPT_options);


%  options=optimset;
%  options.MaxIterations = 1000;
%  [p,resnorm,residual,exitflag,output] = lsqcurvefit(f, p0, t, y, lb, ub,options);


% Calculate sum of squared residuals

SST = sum((y-mean(y)).^2); % Total sum of squares
SSE = sum((f(p,t)-y).^2); % sum of squared residuals
R2 = 1- (SSE/SST);

% Plot results
fit = f(p, t);
plot(t, y, 'b-', t, fit, '-')
xlabel('Time(s)')
ylabel('Stress(Pa)')
 WriteToExcel('g_inf', p(:,1) ,'G','02_PronySeries_tr.xlsx');
 WriteToExcel('g_1', p(:,2) ,'H','02_PronySeries_tr.xlsx');
 WriteToExcel('t_1', p(:,3) ,'I','02_PronySeries_tr.xlsx');
 WriteToExcel('g_2', p(:,2) ,'J','02_PronySeries_tr.xlsx');
 WriteToExcel('t_2', p(:,3) ,'K','02_PronySeries_tr.xlsx');
 WriteToExcel('R^2', R2 ,'L','02_PronySeries_tr.xlsx');
```